Thèse n° 10 028

Self-Interaction and Polarons in Density Functional Theory

Présentée le 24 février 2023

Faculté des sciences de base
Chaire de simulation à l'échelle atomique
Programme doctoral en physique

pour l'obtention du grade de Docteur ès Sciences

par

Stefano FALLETTA

Acceptée sur proposition du jury

Prof. L. Villard, président du jury
Prof. A. Pasquarello, directeur de thèse
Prof. F. Giustino, rapporteur
Prof. F. Mauri, rapporteur
Prof. O. Yazyev, rapporteur

École
polytechnique
fédérale
de Lausanne

2023

*"It is like the point where the rainbow touches the forest.
We think that we can see it—but if we go to look for it,
it isn't there"* – Carlo Rovelli, *The order of time.*

Acknowledgements

Undertaking this PhD thesis has been a memorable and fascinating experience. I dedicate this section to those who have supported me throughout, without the collective help of many of you it would not have gone so smoothly.

First, I want to express my deepest gratitude to my thesis supervisor Professor Alfredo Pasquarello. He has believed in me since the very beginning of my PhD, providing me with insightful and patient guidance throughout this entire journey. I feel privileged to have been exposed to his way of doing science, from the design of a project to the writing of scientific articles. I am deeply grateful for all our daily discussions, for all the notions he taught me, for his constant encouragement, and for his numerous advice in career and in life. He has been an incredibly motivating and inspiring mentor, I could not ask for better guidance.

I would like to thank the jury members of my thesis – Professor Feliciano Giustino, Professor Francesco Mauri, Professor Oleg Yazyev, and Professor Laurent Villard – for having devoted their valuable time to reviewing my thesis and attending my thesis defense.

Among collaborators, I am grateful to Doctor Christoph Freysoldt, for hosting me at the Max Planck Institute for Eisenforschung in Dusseldorf, for all his advice in science, and for his support. I would like to thank also Professor Julia Wiktor, for our discussions, and for her support.

A warm thanks goes to past and current members of the group – Patrick Gono, Thomas Bischoff, Aleksei Tal, Haiyuan Wang, Jing Yang, Jinggang Lan, Arnaud Lorin, Giorgio Palermo, Mathilde Franckel, Mohamed Abdallah – for all the fruitful discussions and for the nice atmosphere in the group. A special thanks goes to Patrick Gono, for his help at the beginning of my PhD. Among other colleagues

at EPFL, I would like to thank Kristians Cernevics, Michele Pizzochero, Nikita Tepliakov, Fabrizio Minganti, Luca Gravina, David Schlegel, Kilian Seibold, Imelda Romero, Gabriel Pescia, Jannes Nys, Antoine Baillod, and Sam Nyckees for the nice atmosphere in the Physics department. I would like to thank Patrick Gono, Michele Pizzochero, Sophie Beck, Tara Tošić, and Guido Gandus for their support in the organisation of summer schools and workshops at EPFL and ETHZ throughout these years.

An immense thanks goes to all the friends that accompanied me throughout these years in Lausanne – Mazen Fouad, Federico Pucci, Ilaria Ricchi, Hannah Schede, Paola Mejia, Max Stieber, Mahmoud Said, Alex Holloway, Giorgio Rossi, Benjamin Gallusser, Melissa Des Crescenzio, Martin Josifoski, Asli Yörüsün, Luka Milosevic, Maxime Colignon, David Cotier, Giorgio Palermo, Begoña Espiñeira, Luca Gravina, Patrick Gono, Kristians Cernevics, Elija Grinhagena, and Debora Sesia – for all our adventures, laughters, travels, and for creating a family atmosphere in Switzerland. I am deeply grateful to my friend and flatmate Mazen Fouad for all the funny moments spent in the house, and for his motivational support.

I would like to dedicate another special thanks to all the friends from university studies – Andrea Pizzi, Lorenzo Pacchiardi, Gabriele Di Rosa, Daniele Poggi, Walter Agostinelli, Alessio Durante, and Saverio Tavernese – for their constant encouragement, and for the nice experiences and travels in these years. They have always been a source of great inspiration for me. Another great thanks goes to Mary Zaki for her continued support.

I would like to thank Estella Dong for her love, kindness, and for always making my days cheerful.

Finally, an incommensurable thanks goes to my family, especially to my mother Isabella, my father Vincenzo, my brother Angelo, and my sister-in-law Antoinette, for their unconditional love, guidance, advice, encouragement, and support in life. I dedicate this thesis to them.

Lausanne, December 15th, 2022 Stefano Falletta

Abstract

The electron self-interaction is a long-standing problem in density functional theory and is particularly critical in the description of polarons. Polarons are quasiparticles involving charge localization coupled with self-induced lattice distortions. Since their prediction by Landau almost a century ago, polarons have drawn a great deal of attention in physics, chemistry, and materials science. The polaron stability results from the competition between the energy gain associated with the charge localization and the energy cost of the involved lattice distortions. Therefore, the polaron localization and its formation energy are sensitively affected by the description of the electron self-interaction. Various competitive correction schemes based on either one-body or many-body descriptions of the self-interaction have been proposed to solve this longstanding problem. At present, it remains unclear which of these two descriptions of the self-interaction needs to be addressed in polaron physics.

In this thesis, we address the self-interaction problem in relation to polarons in density functional theory. First, we develop a scheme for correcting finite-size electrostatic effects involving the polaron charge density, which is crucial for achieving energetics of isolated polarons. Then, we study polarons with state-of-the-art hybrid functionals, highlighting the notion of formation energy for determining the polaron stability. Next, we develop a unified theoretical framework encompassing one-body and many-body forms of self-interaction, which confers superiority to the notion of many-body self-interaction over the notion of one-body self-interaction. Given the preeminence of the many-body self-interaction, we introduce an efficient semilocal scheme for localizing polarons based on the inclusion of a weak local potential in the semilocal Hamiltonian to suppress the many-body self-interaction. Taking advantage of these findings, we develop a selection criterion for the Hubbard interaction in Hubbard-corrected functionals. Finally, we apply our methodologies to the case of an anisotropic system, and use semilocal functionals free from many-body self-interaction to calculate polaron hopping rates. In this context, we demonstrate that polaron properties free from many-body self-interaction, including formation energies, hopping energy barriers, and hopping rates are robust upon variation of the functional. This supports the use of our semilocal scheme and of the Hubbard-corrected functional over computationally more expensive hybrid functionals.

This thesis advances the conceptual understanding of the self-interaction problem in density functional theory, and paves the way to efficient calculations of polarons in large systems, in systematic studies involving large sets of materials, in molecular dynamics evolving over long time periods, and in charge transfer mechanisms.

Keywords: Self-interaction, Polarons, Defects, Phonons, Electronic Structure

Résumé

L'auto-interaction des électrons est un problème de longue date dans la théorie de la fonctionnelle de la densité et est particulièrement critique dans la description de polarons. Les polarons sont des quasi-particules impliquant une localisation de la charge couplée à des distorsions auto-induites du réseau. Depuis leur prédiction par Landau il y a presque un siècle, les polarons ont attiré une grande attention en physique, en chimie et en science des matériaux. La stabilité de polarons résulte de la compétition entre le gain d'énergie associé à la localisation de la charge et le coût énergétique des distorsions induite du réseau. Par conséquent, la localisation du polaron et son énergie de formation sont affectées de manière sensible par la description de l'auto-interaction des électrons. Divers schémas de correction basés sur des descriptions à un ou plusieurs corps de l'auto-interaction ont été proposés pour résoudre cet ancien problème. A l'heure actuelle, il n'est pas clair laquelle de ces deux descriptions de l'auto-interaction doit être prise en compte dans la physique de polarons.

Dans cette thèse, nous abordons le problème de l'auto-interaction en relation avec les polarons dans la théorie de la fonctionnelle de la densité. Tout d'abord, nous développons un schéma pour corriger les effets électrostatiques de taille finie impliquant la densité de charge du polaron, ce qui est crucial pour obtenir l'énergétique de polarons isolés. Ensuite, nous étudions les polarons à l'aide de fonctionnelles hybrides de pointes, en mettant en évidence la notion d'énergie de formation pour déterminer la stabilité de polarons. Par la suite, nous développons un cadre théorique unifié englobant les formes d'auto-interaction à un corps et à plusieurs corps, ce qui confère à la notion d'auto-interaction à plusieurs corps une supériorité sur la notion d'auto-interaction à un corps. Étant donné la prééminence de l'auto-interaction entre plusieurs corps, nous introduisons un schéma semilocal efficace pour localiser les polarons, basé sur l'inclusion d'un potentiel local faible dans l'Hamiltonien semilocal pour supprimer l'auto-interaction à plusieurs corps. En exploitant ces résultats, nous développons un critère de sélection pour l'interaction de Hubbard dans les fonctionnelles corrigées par Hubbard. Enfin, nous appliquons nos méthodologies au cas d'un système anisotrope, et nous utilisons des fonctionnelles semilocales exemptes d'auto-interaction à plusieurs corps pour calculer les taux de sauts des polarons. Dans ce contexte, nous démontrons que les propriétés des polarons affranchis de l'auto-interaction à plusieurs corps, dont les énergies de formation, les barrières énergétiques de saut, et les taux de saut sont robustes lors de variations de la fonctionnelle. Ceci soutient l'utilisation de notre schéma semi-local et de la fonctionnelle corrigée par Hubbard par rapport aux fonctions hybrides plus coûteuses en termes de calcul.

Cette thèse fait progresser la compréhension conceptuelle du problème de l'auto-interaction dans la théorie de la fonctionnelle de la densité, et ouvre la voie à des calculs efficaces de polarons dans de grands systèmes, dans des études systématiques impliquant de grands ensembles de matériaux, dans des dynamiques moléculaires évoluant sur de longues périodes de temps, et dans des mécanismes de transfert de charges.

Mots-clés: Auto-interaction, Polarons, Défauts, Phonons, Structure électronique

Contents

Acknowledgements i

Abstract (English/French) iii

1 Introduction 1
  1.1 Self-interaction in electronic structure theory 1
  1.2 Self-interaction and polarons 4
  1.3 One-body self-interaction 7
  1.4 Many-body self-interaction 9
  1.5 Thesis outline 11

2 Methodology 15
  2.1 Semilocal functional PBE 16
  2.2 Hybrid functional PBE0(α) 17
  2.3 Hubbard-corrected functional DFT+U 18
  2.4 Atomic forces and Hellmann-Feynman theorem 19
  2.5 Janak's theorem 20
  2.6 Electrostatic corrections due to finite-size supercells 21
  2.7 Nudged-elastic-band method 24
  2.8 Polaron hopping rate 26

3 Finite-size corrections of defect energy levels involving ionic polarization 29
  3.1 Introduction 30
  3.2 Methodology 30
  3.3 Results 34
  3.4 Ionic polarization charge 38
  3.5 Sum rule from thermodynamic integration 39
  3.6 Comparison with previous literature 42

3.7 Discussion 44

4 Polarons modelled through hybrid functionals 45

4.1 Introduction 46

4.2 Polaron formation energy 47

4.3 Computational details 48

4.4 Results 50

4.5 Band gaps 53

4.6 Discussion 54

5 Unified formulation for the self-interaction 55

5.1 Introduction 56

5.2 Assumptions 56

5.3 Many-body self-interaction 59

5.4 One-body self-interaction 63

5.5 Relationship between many-body and one-body self-interaction . . . 64

5.6 Screening model 68

5.7 Connection with other previous literature 71

5.8 Discussion 72

6 Semilocal γDFT scheme for polaron localization 73

6.1 Introduction 74

6.2 Methodology 74

6.3 Computational advantages 77

6.4 Self-consistent scissor operator 79

6.5 Results 80

6.6 Discussion 85

7 Hubbard U through polaronic defect states 87

7.1 Introduction 88

7.2 Selection criterion for U 88

7.3 Results 89

7.4 Band gaps and density of states 91

7.5 Polaronic defects 93

7.6 Comparison with linear-response method 95

7.7 Discussion 97

8 Polaron hopping through piecewise-linear functionals 99

8.1 Introduction . . . 100
8.2 Stable polaronic states . . . 101
8.3 Polaron hopping . . . 108
8.4 Discussion . . . 111

9 Conclusion 115

A Appendix: Scissor operator for opening the band gap 119
A.1 Introduction . . . 120
A.2 Methodology . . . 120
A.3 Results . . . 121
A.4 Discussion . . . 123

B Appendix: Code implementation in Quantum Espresso 125
B.1 Implementation of the γDFT scheme . . . 126
B.2 Implementation of the scissor operator . . . 129

Bibliography 131

Curriculum Vitae 147

1 Introduction

> *"The underlying physical laws necessary for the mathematical theory of a large part of physics and the whole of chemistry are thus completely known, and the difficulty is only that the exact application of these laws leads to equations much too complicated to be soluble. It therefore becomes desirable that approximate practical methods of applying quantum mechanics should be developed, which can lead to an explanation of the main features of complex atomic systems without too much computation."* –
> Paul Dirac, 1929 [1]

1.1 Self-interaction in electronic structure theory

Quantum mechanics is a fundamental theory that describes the physical phenomena at the atomic and subatomic scale. In this theory, particles like electrons can be treated as waves and they are governed by a complex wave equation, namely the Schrödinger equation. Even though quantum mechanics is not yet fully understood, our current knowledge of quantum mechanics can be used for making predictions of physical properties to be compared with experiment. In particular, one of the most important applications of quantum mechanics consists in *modelling condensed matter from first principles*, in order to understand its properties at a quantitative level. *Condensed matter* refers to any system with many constituents interacting with each other, such as solids and liquids; *modelling* refers to the description of a system using mathematical laws; *from first principles* denotes the approach of starting from basic concepts that cannot be deduced from any other proposition. In the language of quantum mechanics, these concepts refer to solving the Schrödinger equation for a given atomic system. Despite knowing this exact law of quantum mechanics, its solution is extremely challenging. Indeed, condensed matter systems are characterized by a multitude of interactions between electrons and ions. While the treatment of ions can be generally simplified assuming that their movements are much slower than those of electrons, the number of electron-electron interactions grows tremendously with the number of electrons. For this reason, the exact treatment of such interactions becomes inaccessible from a computational point of view. As highlighted by the Nobel laureate Kohn [2],

> *"In general the many-electron wave function* $\Psi(\mathbf{r}_1, \dots, \mathbf{r}_N)$ *for a system of* N *electrons is not a legitimate scientific concept, when* $N > N_0$*, where* $N_0 \approx 10^3$*."*

This calls for the development of approximate strategies for modelling the complex Coulomb interactions between electrons, thus paving the way to the field of electronic structure theory.

Electronic structure methods have made an unprecedented impact on the use of quantum mechanics for studying challenging problems in physics, chemistry and materials science. In such methods, the interactions between electrons are calculated in an approximate way, thereby allowing for the computational modelling of condensed matter from first principles. Depending on the level of theory, more physical ingredients can be taken into account, and the comparison between theory and experiments can be improved. However, the computational cost of such calculations increases with the level of theory, and can become inaccessible for studying technologically relevant applications. Hence, for this reason, the ability of obtaining accurate results within computationally efficient methods is a core objective of electronic structure methods.

One of the most notorious shortcomings in electronic structure theory is the long-standing problem of the electron self-interaction. This consists in the interaction of the electron with itself, which arises from the approximate treatment of the electron-electron interactions. Clearly, such a spurious effect is absent in the exact theory, since electrons interact only in pairs. The self-interaction is responsible for many failures of widely-used electronic structure methods, including the incorrect prediction of binding energies, ionization potentials, electron affinities, charge transfer rates, and band gaps. These properties are critical for the determination of the structural, electronic, and transport properties of materials. For instance, the optical and transport properties of semiconductors are largely affected by the presence of defects in the crystal lattice. In this context, the account of the electron self-interaction enables a direct comparison between theory and experiment, and is thus crucial for the design of electronic and optoelectronic devices.

In the following, we give a brief overview of some landmark schemes developed in electronic structure theory, and of related approaches for addressing the electron self-interaction. In 1927, Thomas and Fermi proposed a semiclassical approach [3, 4] in which the potential energy is a function of the total electron density n, namely

$$U[n] = \frac{1}{2}\int d\mathbf{r}d\mathbf{r}' \, \frac{n(\mathbf{r})n(\mathbf{r}')}{|\mathbf{r}-\mathbf{r}'|}. \tag{1.1}$$

However, as highlighted in 1934 by Fermi and Amaldi [5], the potential energy U does not vanish for a one electron system due to the spurious interaction of the electron with itself. To address such issue, these authors proposed a simple expression of the self-interaction energy correction, namely

$$\Delta E[n]|_{\mathrm{TF}} = -NU\left[\frac{n}{N}\right], \tag{1.2}$$

which constitutes the first attempt for addressing the electron self-interaction. In this way, the potential energy $U + \Delta E|_{\mathrm{TF}}$ vanishes in the limit of a system with one electron. However, the Thomas-Fermi theory carries several shortcomings, including the classical treatment of the kinetic energy, and the lack of exchange-correlation effects between electrons. Improvements to the Thomas-Fermi theory were made by Hartree in 1928 [6], by including the quantum-mechanical treatment of the kinetic term. However, Hartree theory suffers from the lack of exchange-correlation effects, and therefore its applicability remains limited.

In 1930, Fock included exchange effects to the Hartree energy, thereby leading to the Hartree-Fock theory [7]. In this case, the potential energy is defined as

$$U = \frac{1}{2}\int d\mathbf{r}d\mathbf{r}' \, \frac{n(\mathbf{r})n(\mathbf{r}')}{|\mathbf{r}-\mathbf{r}'|} - \frac{1}{2}\sum_{ij}\int d\mathbf{r}d\mathbf{r}' \, \frac{\psi_i^*(\mathbf{r})\psi_j^*(\mathbf{r}')\psi_j(\mathbf{r})\psi_i(\mathbf{r}')}{|\mathbf{r}-\mathbf{r}'|}, \tag{1.3}$$

which is a functional of the wave functions due to the presence of the Fock exchange energy. The Fock exchange energy cancels the Hartree self-interaction of each orbital. In this sense, the Hartree-Fock method is considered to be free from self-interaction. However, correlation effects are still missing. Moreover, the dependence of U on the wave functions leads to a more substantial computational cost compared to methods based on the electron density, like Hartree theory.

In 1965, density functional theory was introduced [8, 9]. Similarly to Thomas-Fermi theory, density functional theory is based on using the electron density to describe the complex many-body effects within a single-particle formalism. However, in contrast to Thomas-Fermi theory, density functional theory includes an approximate exchange-correlation energy [10], which is a functional of the electron density. Due to its lower computational cost compared to methods based on wave functions, like Hartree-Fock theory, density functional theory has become a widely-used method for modelling condensed matter systems.

In density functional theory, the concept of self-interaction has been associated to one-body and many-body formulations [11–21]. The one-body self-interaction generally refers to the way the interaction of a charge with itself is cancelled in Hartree-Fock theory. At variance, the many-body self-interaction corresponds to the deviation from the piecewise linearity of the total energy upon electron occupation [11–14, 16]. At the present, it remains unclear which of these two descriptions of the self-interaction needs to be addressed for an accurate determination of quasiparticle stabilities. Additionally, it remains to be determined how the suppression of the self-interaction can be achieved through a computationally-efficient scheme.

1.2 Self-interaction and polarons

The electron self-interaction is particularly critical in the description of a class of quasiparticles with relevant applications in optical and transport properties: the polarons [23]. In a crystal, a polaron is a quasiparticles consisting of a localized charge dressed by its self-induced lattice distortions (cf. Fig. 1.1). Historically, the concept of polarons has been first discussed in 1933 by Landau [24], who introduced the idea of a trapped electron coupled with lattice distortions. In 1946, Pekar illustrated the first theoretical description of a free electron interacting with a polarizable dielectric continuum [25]. Subsequently, Landau and Pekar showed that such interactions can lead to the localization of the wave function, and to an increased effective mass [26]. This result inspired several studies based on effective Hamiltonians treating electron-phonon interactions. Depending on the strength of the electron-phonon interactions, two types of polarons are distinguished. In the limit of weak coupling, the polaron has a large spatial extension and is called large polaron (or Fröhlich polaron) [27]. At variance, in the limit of strong coupling, the polaron localizes over a short length scale comparable to the lattice parameter and is named small polaron (or Holstein polaron) [28]. A great deal of attention has been devoted to finding accurate solutions of the Fröhlich polaron Hamiltonian for various strengths of the electron-phonon interactions, including the preliminary work of Lee, Low, and Pines [29], Fröhlich [30], Feynman [31], and others [32–35]. Large polarons have generally been studied via Monte Carlo [36], path-integral Monte Carlo [37], and the renormalization group [38]. At variance, small polarons have mostly been investigated through first-principles approaches based on density functional theory [39–48]. Recently, Sio *et al.* have developed a unified formulation for small and large polarons inspired by the Landau-Pekar model, which allows one to obtain the polaron wave functions and the associated lattice displacements [49, 50]. An alternative approach based on a canonical transformation has been proposed for capturing lattice vibrations and thermal effects [51, 52]. A comparison between the two methods has been discussed by Luo *et al.* [52], including the advantages and shortcomings of both approaches. These recent developments combining many-body theories with density functional theory open up interesting possibilities in the field of polaron physics.

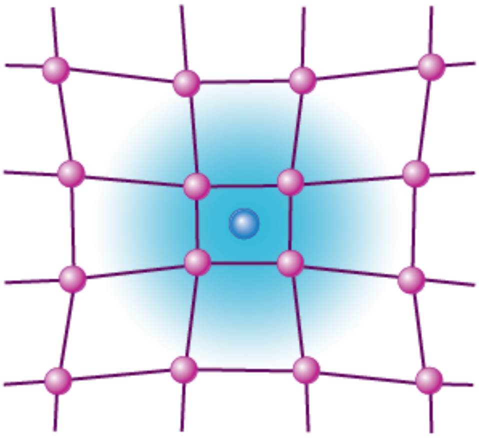

Figure 1.1 – Sketch of a polaron in a crystal. Image taken from Ref. [22].

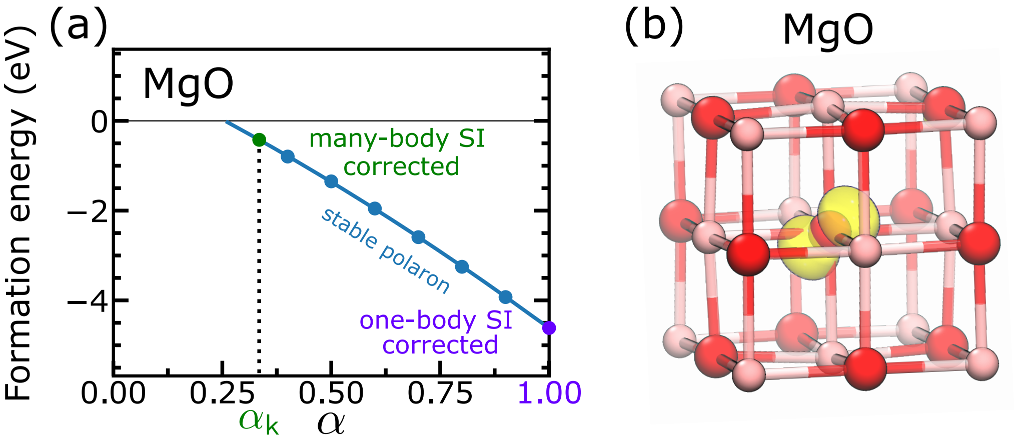

Figure 1.2 – (a) Stability of the hole polaron in MgO as obtained with the hybrid functional PBE0(α) [53]. The parameter α denotes the amount of mix between semilocal density functional theory ($\alpha = 0$) and Hartree-Fock theory ($\alpha = 1$). The stability is measured through the concept of formation energy (cf. Chapter 4). The many-body and the one-body self-interaction are suppressed at $\alpha = \alpha_\text{k}$ and at $\alpha = 1$, respectively. (b) Isodensity surface of the hole polaron at 5% of its maximum (Mg in pink, O in red). The hole polaron is centered on an O atom, leading to longer bonds with neighboring Mg atoms.

The localized nature of polarons is opposed to the delocalized nature of electrons in periodic crystals, which are described by Bloch waves. The charge localization is enabled by the structural symmetry breaking, when the energy gain due to charge localization overcomes the energy cost due to lattice distortions. Therefore, the polaron stability is sensitively affected by the description of the electron self-interaction. As an example, in Fig. 1.2(a) we consider the stability of the hole polaron in magnesium oxide when using hybrid functionals [53], which admix a fraction of Fock exchange to the semilocal exchange. The polaron stability can deviate by several electronvolts when addressing either the many-body or the one-body self-interaction. However, it should be remarked that the cancellation of the many-body self-interaction further guarantees an accurate description of the band gap [40], which in turn gives defect energy levels in good agreement with experiment and state-of-the-art *GW* many-body calculations [54]. At variance, the cancellation of the one-body self-interaction generally leads to very large polaron formation energies, on par with the overestimation of band gaps in Hartree-Fock theory. This strongly suggests that one should correct for the many-body rather than for the one-body self-interaction. In the following, we focus on the concepts of one-body and many-body self-interaction in density functional theory, and briefly outline various approaches developed to address them.

1.3 One-body self-interaction

The one-body self-interaction generally refers to the way the interaction of a charge with itself is cancelled in Hartree-Fock theory. This arises from the interaction of the electron with the effective potential generated by the total electron density, which includes the electron density itself. As a consequence, the electron interacts with the potential generated by itself (cf. Fig. 1.3).

Many schemes have been developed to solve the problem of the one-body self-interaction. In 1981, Perdew and Zunger proposed an approach that removes the single-particle self-interaction pertaining to each electron state [55]. In this approach, the self-interaction energy is written as

$$\Delta E|_{\mathrm{PZ}} = -\sum_{i\sigma}(E_{\mathrm{H}}[n_{i\sigma}] + E_{\mathrm{xc}}[n_{i\sigma}, 0]), \tag{1.4}$$

where $n_{i\sigma}$ is the density of the i-th orbital in the spin channel σ, E_{H} the Hartree energy, and E_{xc} the exchange-correlation energy. The total energy functional including $\Delta E|_{\mathrm{PZ}}$ vanishes for a one-electron system, thereby recovering an exact property. However, the self-consistent minimization of the resulting energy functional is challenging, since the Hamiltonian becomes orbital dependent. Hence, the diagonalization of such orbital-dependent Hamiltonian requires the use of more sophisticated diagonalization algorithms [56].

Subsequently, schemes that specifically address the one-body self-interaction of an

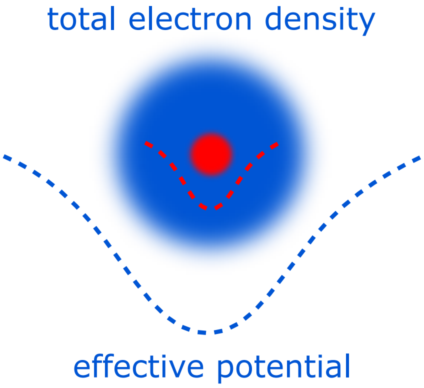

Figure 1.3 – In semilocal density functional theory, each electron interacts with the effective potential generated by the total electron density. Each electron contributes to the effective potential, thus generating a spurious electron self-interaction.

excess charge were proposed [57, 58]. Without loss of generality, we here consider the case of an extra electron in the spin channel ↑. Then, the Perdew-Zunger method can be simplified by considering only the energy contribution pertaining to the extra charge [57], namely

$$\Delta E|_{\mathrm{sPZ}} = -(E_{\mathrm{H}}[m] + E_{\mathrm{xc}}[m, 0]), \tag{1.5}$$

where $m = n_\uparrow - n_\downarrow$ is the magnetization density. A variation of the Perdew-Zunger functional is achieved by introducing two parameters a and b in Eq. (1.5), resulting in the following expression [58]

$$\Delta E|_{\mathrm{SS}} = -(aE_{\mathrm{H}}[m] + bE_{\mathrm{xc}}[m, 0]), \tag{1.6}$$

where a and b are tuned to obtain accurate energetics [58]. A further step proposed by d'Avezac *et al.* consists in identifying the self-interaction energy as [57]

$$\Delta E|_{\mathrm{US}} = -(E_{\mathrm{H}}[m] + E_{\mathrm{xc}}[n_\uparrow, n_\downarrow] - E_{\mathrm{xc}}[n_\uparrow - m, n_\downarrow]), \tag{1.7}$$

which replaces the exchange-correlation functional of the charged system with the one of the neutral system. The self-consistent minimization of the energy functionals including either $\Delta E|_{\mathrm{sPZ}}$, $\Delta E|_{\mathrm{SS}}$, or $\Delta E|_{\mathrm{US}}$ requires the use of the restricted open shell condition on the wave orbitals [57], which enforces the valence wave functions of the two spin channels to be equal. Moreover, in the approach of d'Avezac *et al.*, the exchange-correlation interaction of the valence electrons with the polaron is cancelled [50].

More recently, Sio *et al.* modelled electron-phonon interactions within an *ab-initio* formulation and derived therefrom a one-body self-interaction approach for polarons [49, 50]. In this approach, the self-interaction energy correction is identified as the second-order expansion term of the total energy with respect to the polaron density, namely

$$\Delta E|_{\mathrm{Sio}} = -\left(E_{\mathrm{H}}[n_{\mathrm{p}}] + \frac{1}{2}\int d\mathbf{r}d\mathbf{r}' \, \frac{\delta^2 E_{\mathrm{xc}}[n_\uparrow, n_\downarrow]}{\delta n_{\sigma_{\mathrm{p}}}(\mathbf{r})\delta n_{\sigma_{\mathrm{p}}}(\mathbf{r}')} n_{\mathrm{p}}(\mathbf{r}) n_{\mathrm{p}}(\mathbf{r}') \right), \tag{1.8}$$

where n_{p} is the polaron density, and σ_{p} the corresponding spin channel. For an electron polaron in the spin channel $\sigma_{\mathrm{p}} = \uparrow$, Eq. (1.8) can be expressed with finite differences as

$$\Delta E|_{\mathrm{Sio}} = -\bigg(E_{\mathrm{H}}[n_{\mathrm{p}}] + \frac{1}{2}E_{\mathrm{xc}}[n_{\uparrow\mathrm{val}} + n_{\mathrm{p}}, n_{\downarrow\mathrm{val}}] \\ + \frac{1}{2}E_{\mathrm{xc}}[n_{\uparrow\mathrm{val}} - n_{\mathrm{p}}, n_{\downarrow\mathrm{val}}] - E_{\mathrm{xc}}[n_{\uparrow\mathrm{val}}, n_{\downarrow\mathrm{val}}] \bigg), \tag{1.9}$$

where $n_{\sigma\mathrm{val}}$ denotes the density of the valence electrons in the spin channel σ.

1.4 Many-body self-interaction

The many-body self-interaction corresponds to the deviation from the piecewise linearity of the total energy upon electron occupation [11, 14, 18, 59], which is a property of the exact density functional [11–14, 16]. The piecewise linearity is related to the notion of grand canonical ensemble, since it is defined for a system with fractional charge. Nevertheless, the enforcement of the piecewise linearity is crucial for achieving an accurate description of ground-state and excited-state properties of systems with integer number of electrons [19]. For instance, defect energy levels are crucially affected by the description of the many-body self-interaction and have a large impact on the optical properties of materials.

The concept of piecewise linearity was introduced by Perdew *et al.* in 1982 [11]. These authors showed that the ground state energy of a system with a fractional number of electrons $N + \Delta N$ can be written as a linear interpolation of the ground state energies of the corresponding integer states, namely

$$E(N + \Delta N) = (1 - \Delta N) \cdot E(N) + \Delta N \cdot E(N + 1), \tag{1.10}$$

where ΔN is in between 0 and 1. Then, a system with a fractional number of electrons can be interpreted as a statistical mixture of ground-state systems with integer number of electrons. This exact property must hold for any ensemble, and in particular it must be true also in density functional theory. Another interpretation involving replicas of pure states was given by Yang *et al.* [14]. In this picture, for a system of $N + \Delta N$ electrons, one considers many replicas of N-electrons systems with an extra electron. The extra electron can be in any of the replicas, resulting in various degenerate systems. Any linear combination of such degenerate systems, resulting into a fractional number of electrons, is still degenerate and thus satisfies

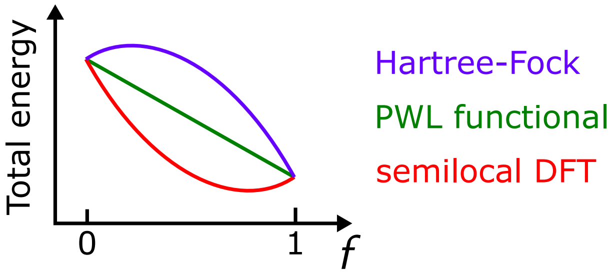

Figure 1.4 – Total energy as a function of the electron occupation f, as obtained with standard semilocal density functional theory, Hartree-Fock theory, and piecewise-linear functionals.

Eq. (1.10). These two interpretations are connected through the Boltzmann's ergodic hypothesis [19].

Most density functionals do not comply with the piecewise linearity. As illustrated in Fig. 4.1(a), semilocal density functional theory [10] yields a total energy with positive concavity with respect to the fractional electron charge. Similarly, the total energy obtained with the Hartree-Fock functional is concave. When the functional is piecewise linear, the many-body self-interaction vanishes. Hybrid functionals mixing semilocal density functional and Hartree Fock energies offer a straightforward way to address the many-body self-interaction. In order to cancel the many-body self-interaction, the hybrid functional parameters are adjusted to enforce the piecewise linearity of the total energy upon electron occupation [19, 40, 60]. Hybrid functionals satisfying such a constraint yield localized polarons [40, 61–63] and band gaps in agreement with state-of-the-art GW calculations [40, 60, 64–67]. However, hybrid functionals increase dramatically the computational cost of density functional theory calculations and therefore become unaccessible for large systems.

Alternatively, the inclusion of a Hubbard correction U can also be used to overcome the many-body self-interaction and to enforce the piecewise linearity condition [17, 68]. In particular, Cococcioni and de Gironcoli proposed a linear response approach to fix the parameter U in order to retrieve the piecewise linearity in perturbation theory [68]. A similar approach was introduced by Lany and Zunger [17], which consists in including a Hubbard-like operator in the Hamiltonian with a strength adjusted to comply with the piecewise linearity. However, the performance of Hubbard-corrected functionals in comparison to hybrid functionals remain to be assessed. Moreover, it is of interest to investigate whether polaronic states can be used to determine of U in DFT+U functionals.

An alternative approach for addressing the many-body self-interaction in relation to polarons has been proposed by Sadigh *et al.* [61]. In their method, the self-interaction corrected energy is linear, with a slope corresponding to the polaron energy level calculated in the limit of zero charge. However, this leads to an overestimation of the polaron formation energy due to the enforcement of the polaron energy level at zero charge. Other methods enforce the piecewise linearity condition on the entire electronic manifold by modifying the Hamiltonian pertaining to each orbital [69–71], like in the Perdew-Zunger method. However, the resulting equations are orbital dependent and therefore require more complex diagonalization algorithms [56].

1.5 Thesis outline

The goal of this thesis is to address the self-interaction problem in relation to polarons. This thesis is organised as follows.

In Chapter 2, we summarize background methodology in density functional theory, including semilocal, hybrid, and Hubbard-corrected functionals, and notorious theorems. Additionally, we emphasize the importance of correcting for finite-size electrostatic effects when modelling excess charges in supercells, and discuss state-of-the-art methods for calculating electron-transfer rates.

In Chapter 3, we develop a scheme for correcting the finite-size effects of defects involving frozen lattice distortions, which is necessary for achieving an accurate energetics of isolated polarons. Our scheme accounts on an equal footing for the screening of the electrons and of the polarization charge due to the lattice distortions, and finds applications in correcting vertical transition energies.

In Chapter 4, we study polarons free from many-body self-interaction with hybrid functionals. In particular, we highlight the concept of formation energy for determining the polaron stability. Moreover, we show that hybrid functionals free from many-body self-interaction lead to an overall improvement of the electronic structure, including the band gap.

In Chapter 5, we develop a unified formulation for one-body and many-body forms of self-interaction. Within this formulation, we quantitatively connect the two forms of self-interaction through the dielectric constant. We show that addressing the many-body self-interaction accounts for additional screening effects, which are overseen when addressing the one-body self-interaction. This allows us to demonstrate the superiority of the concept of many-body self-interaction over the concept of one-body self-interaction.

In Chapter 6, we introduce a semilocal scheme for polaron localization. This is achieved by including a weak local potential in the semilocal Hamiltonian that suppresses the many-body self-interaction of the polaron state. Possible resonances involving the polaron state and delocalized states are overcome by including a scissor operator to the Hamiltonian. Our approach yields polaron formation energies in agreement with those obtained with hybrid functionals, but at a significantly lower computational cost. This highlights that polaron properties free from many-body self-interaction are robust upon variation of the functional adopted.

In Chapter 7, we introduce a criterion for selecting the Hubbard parameter U in DFT+U calculations such that the many-body self-interaction of polarons is suppressed. We show that the resulting polaron properties are in good agreement with results from hybrid functional calculations, thereby corroborating the robustness of polaron properties free from many-body self-interaction. This further supports the use of semilocal functionals for modelling polarons.

In Chapter 8, we use functionals free from many-body self-interaction to study the polaron energy landscape and hopping rates in the case of an anisotropic material hosting multiple polaronic states. We find that single-site and multi-site polaronic states can be found in close energetic competition. Moreover, we show that the robustness of polaron properties obtained with piecewise-linear functionals also extends to polaron transport properties, including energy barriers and hopping rates. This validates the use of semilocal piecewise-linear functionals for studying polaron transport.

In Chapter 9, we summarize our results, and give an outlook on future developments and applications.

In Appendix A, we address the band-gap problem in semilocal density functional theory by introducing a scissor operator to the Hamiltonian. We show that this methodology leads to accurate properties of bulk system when compared to those obtained with hybrid functionals, but at a lower computational cost. In Appendix B, we discuss the implementation details of our semilocal scheme for polaron localization and of the scissor operator.

2 Methodology

We present the state-of-the art methodology for density functional theory calculations that constitute the basis for this thesis. First, we discuss semilocal functionals, hybrid functionals, and Hubbard corrected DFT+U functionals. Then, we present the Hellmann-Feynman theorem and the Janak's theorem, which will be frequently used throughout this thesis. Next, we highlight the importance of correcting the energetics obtained in the presence of external charges in supercells to avoid spurious electrostatic interactions. Finally, we outline the nudged-elastic-band method for calculating adiabatic energy landscapes, and a widely-used method for determining electron-transfer rates.

2.1 Semilocal functional PBE

Without loss of generality, we here adopt a plane-wave-pseudopotential formulation. We take the Perdew-Burke-Ernzerhof (PBE) functional [10] as reference for our semilocal calculations. This consists in solving the following set of Kohn-Sham equations for each spin channel σ:

$$\mathcal{H}^0_\sigma[n^0_\uparrow, n^0_\downarrow]\psi^0_{i\sigma} = \epsilon^0_{i\sigma}\psi^0_{i\sigma}, \tag{2.1}$$

where $\mathcal{H}^0_\sigma$ is the PBE Hamiltonian, $\psi^0_{i\sigma}$ and $\epsilon^0_{i\sigma}$ are the resulting wave functions and energy levels, and $n^0_\sigma = \sum_i |\psi^0_{i\sigma}|^2$ is the electron density in the spin channel σ. The Hamiltonian $\mathcal{H}^0_\sigma$ is defined as

$$\mathcal{H}^0_\sigma[n^0_\uparrow, n^0_\downarrow] = -\tfrac{1}{2}\nabla^2 + V_{\rm ps} + V_{\rm H}[n^0] + V_{{\rm xc}\sigma}[n^0_\uparrow, n^0_\downarrow], \tag{2.2}$$

where $n^0 = \sum_\sigma n^0_\sigma$ is the total electron density, $-\frac{1}{2}\nabla^2$ the kinetic term, $V_{\rm ps}$ the sum of the local and nonlocal pseudopotentials, $V_{\rm H}(\mathbf{r}) = \int d\mathbf{r}'\, n^0(\mathbf{r}')/|\mathbf{r}-\mathbf{r}'|$ the Hartree potential, and $V_{{\rm xc}\sigma} = V_{{\rm x}\sigma} + V_{{\rm c}\sigma}$ the semilocal PBE exchange-correlation potential [10]. We remark that the semilocal exchange potential $V_{{\rm x}\sigma}$ depends only on the density in the spin channel σ. This can be seen by using the exact relation [72]

$$V_{{\rm x}\sigma}[n^0_\uparrow, n^0_\downarrow] = V_{\rm x}[2n^0_\sigma], \tag{2.3}$$

where $V_{\rm x}[2n^0_\sigma]$ denotes the spin-unpolarized exchange potential evaluated for the density $2n^0_\sigma$. Then, the PBE energy is given by

$$\begin{aligned} E^0[\{\psi^0_{i\uparrow}\}, \{\psi^0_{i\downarrow}\}] = T[n^0] + E_{\rm H}[n^0] + E_{\rm xc}[n^0_\uparrow, n^0_\downarrow] \\ + E_{\rm ps}[\{\psi^0_{i\uparrow}\}, \{\psi^0_{i\downarrow}\}] + E_{\rm Ewald}, \end{aligned} \tag{2.4}$$

where T is the kinetic energy, $E_{\rm H}$ the Hartree energy, $E_{\rm xc} = E_{\rm x} + E_{\rm c}$ the semilocal exchange-correlation energy, $E_{\rm ps}$ the pseudopotential energy, and $E_{\rm Ewald}$ the Ewald energy. The Hartree energy is given by

$$E_{\rm H}[n^0] = \frac{1}{2}\int d\mathbf{r}d\mathbf{r}'\, \frac{n^0(\mathbf{r})n^0(\mathbf{r}')}{|\mathbf{r}-\mathbf{r}'|}. \tag{2.5}$$

2.2 Hybrid functional PBE0(α)

We consider the class of hybrid functionals PBE0(α) [53], in which a fraction α of Fock exchange is admixed to a fraction $(1-\alpha)$ of local PBE exchange. This corresponds to solving the following generalized Kohn-Sham equations

$$\mathcal{H}^{\alpha}_{\sigma}[\{\psi^{\alpha}_{j\uparrow}\},\{\psi^{\alpha}_{j\downarrow}\}]\psi^{\alpha}_{i\sigma} = \epsilon^{\alpha}_{i\sigma}\psi^{\alpha}_{i\sigma}, \tag{2.6}$$

where $\psi^{\alpha}_{i\sigma}$ and $\epsilon^{\alpha}_{i\sigma}$ are the resulting wave functions and energy levels, respectively, and the Hamiltonian $\mathcal{H}^{\alpha}_{\sigma}$ is given by

$$\mathcal{H}^{\alpha}_{\sigma}[\{\psi^{\alpha}_{i\uparrow}\},\{\psi^{\alpha}_{i\downarrow}\}] = -\tfrac{1}{2}\nabla^2 + V_{\mathrm{ps}} + V_{\mathrm{H}}[n^{\alpha}] + V^{\alpha}_{\mathrm{xc}\sigma}[n^{\alpha}_{\uparrow}, n^{\alpha}_{\downarrow}] + V^{\alpha}_{\mathrm{X}}[\{\psi^{\alpha}_{i\sigma}\}], \tag{2.7}$$

where

$$V^{\alpha}_{\mathrm{xc}\sigma} = (1-\alpha)V_{\mathrm{x}\sigma} + V_{\mathrm{c}\sigma} \tag{2.8}$$

is the semilocal exchange-correlation potential,

$$V^{\alpha}_{\mathrm{X}}[\{\psi^{\alpha}_{i\sigma}\}](\mathbf{r},\mathbf{r}') = -\alpha\sum_{i} f_{i\sigma}\frac{|\psi^{\alpha}_{i\sigma}\rangle\langle\psi^{\alpha}_{i\sigma}|}{|\mathbf{r}-\mathbf{r}'|} \tag{2.9}$$

the Fock potential multiplied by α with $f_{i\sigma}$ being the electron occupation of the i-th state in the spin channel σ, $n^{\alpha}_{\sigma} = \sum_i f_{i\sigma}|\psi^{\alpha}_{i\sigma}|^2$ the electron density in the spin channel σ, and $n^{\alpha} = \sum_{\sigma} n^{\alpha}_{\sigma}$ the total electron density. We remark that the Fock potential contributing to $\mathcal{H}^{\alpha}_{\sigma}$ is constructed using only the wave functions in the spin channel σ. Then, the PBE0(α) energy is given by

$$\begin{aligned} E^{\alpha}[\{\psi^{\alpha}_{i\uparrow}\},\{\psi^{\alpha}_{i\downarrow}\}] \;&=\; T[n^{\alpha}] + E_{\mathrm{H}}[n^{\alpha}] + E^{\alpha}_{\mathrm{xc}}[n^{\alpha}_{\uparrow}, n^{\alpha}_{\downarrow}] + E^{\alpha}_{\mathrm{X}}[\{\psi^{\alpha}_{i\uparrow}\},\{\psi^{\alpha}_{i\downarrow}\}] \\ &\quad + E_{\mathrm{ps}}[\{\psi^{\alpha}_{i\uparrow}\},\{\psi^{\alpha}_{i\downarrow}\}] + E_{\mathrm{Ewald}}, \end{aligned} \tag{2.10}$$

where $E^{\alpha}_{\mathrm{xc}} = (1-\alpha)E_{\mathrm{x}} + E_{\mathrm{c}}$ is the semilocal exchange-correlation energy, and E^{α}_{X} the Fock energy, which is defined as

$$E^{\alpha}_{\mathrm{X}}[\{\psi^{\alpha}_{i\uparrow}\},\{\psi^{\alpha}_{i\downarrow}\} = -\frac{\alpha}{2}\sum_{ij\sigma} f_{i\sigma}f_{j\sigma}\int d\mathbf{r}d\mathbf{r}'\,\frac{\psi^{*}_{i\sigma}(\mathbf{r})\psi^{*}_{j\sigma}(\mathbf{r}')\psi_{j\sigma}(\mathbf{r})\psi_{i\sigma}(\mathbf{r}')}{|\mathbf{r}-\mathbf{r}'|}. \tag{2.11}$$

For $\alpha = 0$, PBE0(α) reduces to PBE.

2.3 Hubbard-corrected functional DFT+U

We consider the Hubbard corrected DFT+U functional. In its simplified rotationally-invariant form, the DFT+U total energy is written as [68, 73]:

$$E^U[n^U_\uparrow, n^U_\downarrow] = E^0[n^U_\uparrow, n^U_\downarrow] + \frac{U}{2}\sum_{I\sigma} \mathrm{Tr}[\mathbf{n}^{I\sigma}(1 - \mathbf{n}^{I\sigma})], \tag{2.12}$$

where E^0 is the PBE energy, n^U_σ the total density in the spin channel σ, U the Hubbard parameter, $\mathbf{n}^{I\sigma}$ the occupation matrix of localized orbitals ϕ^I_m, I the atomic site, m the state index, and σ the spin. The matrix elements $n^{I\sigma}_{mm'}$ are defined as

$$n^{I\sigma}_{mm'} = \sum_i f_{i\sigma} \langle \psi^U_{i\sigma} | \phi^I_m \rangle \langle \phi^I_{m'} | \psi^U_{i\sigma} \rangle \,. \tag{2.13}$$

where $\psi^U_{i\sigma}$ are the wave functions, and $f_{i\sigma}$ the respective occupations. Variational minimization of the energy functional E^U leads to the following Kohn-Sham equations

$$(\mathcal{H}^0_\sigma + V^U_\sigma)\psi^U_{i\sigma} = \epsilon^U_{i\sigma}\psi^U_{i\sigma}, \tag{2.14}$$

where $\mathcal{H}^0_\sigma$ is the PBE Hamiltonian, $\epsilon^U_{i\sigma}$ are the Kohn-Sham eigenvalues, and V^U_σ is the Hubbard potential, which is given by

$$V^U_\sigma = U \sum_{Imm'} \left[\frac{\delta_{mm'}}{2} - n^{I\sigma}_{mm'} \right] |\phi^I_{m'}\rangle\langle\phi^I_m| \,. \tag{2.15}$$

From Eq. (2.15), one can see that the Hubbard potential is repulsive for unoccupied orbitals and attractive for occupied orbitals, thereby favoring the Mott localization of electrons on specific atomic sites.

The parameter U can be calculated in linear-response theory to enforce the piecewise linearity of the total energy upon electron occupation. In the perturbative approach of Cococcioni and de Gironcoli [68], one solves the following set of Kohn-Sham equations:

$$\left(\mathcal{H}_\sigma^0 + \alpha^I \sum_m |\phi_m^I\rangle\langle\phi_m^I|\right)\psi_{i\sigma}^{\alpha^I} = \epsilon_{i\sigma}^{\alpha^I}\psi_{i\sigma}^{\alpha^I}, \tag{2.16}$$

where α^I is the amplitude of the perturbation, and $\epsilon_{i\sigma}^{\alpha^I}$ and $\psi_{i\sigma}^{\alpha^I}$ are the corresponding eigenvalues and wave functions. This corresponds to minimizing the following energy functional

$$E^{\alpha^I}[\{\psi_{i\uparrow}^{\alpha^I}\},\{\psi_{i\downarrow}^{\alpha^I}\}] = E^0[n_\uparrow^{\alpha^I}, n_\downarrow^{\alpha^I}] + \alpha^I n^I, \tag{2.17}$$

where n^I is the total occupation of the localized states for atom I, which is defined as

$$n^I = \sum_{\sigma m} n_{mm}^{I\sigma} = \sum_m f_{i\sigma}|\langle\psi_{i\sigma}^{\alpha^I}|\phi_m^I\rangle|^2. \tag{2.18}$$

Then, U is chosen as

$$U_{\text{LR}} = (\chi_0^{-1} - \chi^{-1})_{II}, \tag{2.19}$$

where χ and χ_0 are the screened and unscreened response matrices, respectively, which are defined as variations of the occupations n^I.

2.4 Atomic forces and Hellmann-Feynman theorem

Without loss of generality, we consider the case of the PBE0(α) hybrid functional. Then, the atomic forces are defined as

$$F_{I\mu}^\alpha = -\frac{dE^\alpha}{d\boldsymbol{\tau}_{I\mu}}, \tag{2.20}$$

where $\boldsymbol{\tau}_{I\mu}$ denotes the Cartesian coordinate μ of the atom I. A naive approach for determining the forces consists in performing multiple evaluations of the total energy for different atomic diplacements, and then use a finite-difference expression of Eq. (2.20). However, this approach would require $3N_I + 1$ evaluations of the total energy, where N_I is the number of ions.

A more efficient method consists in using the Hellmann-Feynman theorem, which allows one to determine the forces on all atoms with a single evaluation of the total energy. For simplicity, we here illustrate the Hellmann-Feynmann theorem for a one-dimensional example. We consider an Hamiltonian $\mathcal{H}$ with eigenstate ψ and energy E. Then, the derivative of the energy E with respect to a parameter λ is given by

$$\frac{dE}{d\lambda} = \frac{d}{d\lambda}\int d\mathbf{r}\,\psi^*\mathcal{H}\psi = \int d\mathbf{r}\left[\frac{d\psi^*}{d\lambda}\mathcal{H}\psi + \psi^*\frac{d\mathcal{H}}{d\lambda}\psi + \psi^*\mathcal{H}\frac{d\psi}{d\lambda}\right]. \tag{2.21}$$

Considering that by construction $\mathcal{H}\psi = E\psi$, then

$$\frac{dE}{d\lambda} = \int d\mathbf{r}\,\psi^*\frac{d\mathcal{H}}{d\lambda}\psi + E\frac{d}{d\lambda}\int d\mathbf{r}\,|\psi|^2 = \int d\mathbf{r}\,\psi^*\frac{d\mathcal{H}}{d\lambda}\psi, \tag{2.22}$$

where we used the normalization of the wave function ψ. This gives

$$\frac{dE}{d\lambda} = \langle\psi|\frac{d\mathcal{H}}{d\lambda}|\psi\rangle\,. \tag{2.23}$$

Hence, using Eq. (2.23), the atomic forces in Eq. (2.20) can be rewritten as

$$F^{\alpha}_{I\mu} = -\left(\sum_{i\sigma}\langle\psi^{\alpha}_{i\sigma}|\frac{dV_{\text{ps}}}{d\boldsymbol{\tau}_{I\mu}}|\psi^{\alpha}_{i\sigma}\rangle + \frac{dE_{\text{Ewald}}}{d\boldsymbol{\tau}_{I\mu}}\right), \tag{2.24}$$

where $\tau_{I\mu}$ is the Cartesian coordinate μ of the atom I. When the wave functions $\psi^{\alpha}_{i\sigma}$ are expanded on a plane-wave basis set, no Pulay forces appear [74]. In Eq. (2.24), there are no explicit contributions resulting from electron-electron interactions (Hartree, exchange-correlation, Fock). Their influence on the atomic forces occurs via the self-consistent optimization of the wave functions $\psi^{\alpha}_{i\sigma}$.

2.5 Janak's theorem

Here, we consider the case of an electron system with only one partially-filled orbital with occupation f. Without loss of generality, we consider the case of the PBE0(α) hybrid functional. Then, the Janak's theorem establishes a connection between the variation of the total energy E^{α} with respect to the occupation f, namely

$$\frac{dE^\alpha(f)}{df} = \epsilon_{\mathrm{p}}^\alpha(f), \tag{2.25}$$

where $\epsilon_{\mathrm{p}}^\alpha$ is the Kohn-Sham energy level of the partially-filled orbital. To prove Eq. (2.25), we introduce the orbitals $\phi_{i\sigma}^\alpha = f_{i\sigma}\psi_{i\sigma}^\alpha$, where $f_{i\sigma}$ is the occupation of the i-th state of the spin channel σ. For the partially-filled orbital, one has $f_{i_{\mathrm{p}}\sigma_{\mathrm{p}}} = f$, where i_{p} and σ_{p} denote the index and the spin-channel of the partially-filled orbital, respectively. Then, by applying the chain rule for the derivative of $E^\alpha(f)$ with respect to f and by using the variational relation

$$\frac{\delta E^\alpha}{\delta \phi_{i\sigma}^\alpha} = \mathcal{H}_\sigma^\alpha \psi_{i\sigma}^\alpha = \epsilon_{i\sigma}^\alpha \psi_{i\sigma}^\alpha, \tag{2.26}$$

the left-hand side of Eq. (2.25) can be written as

$$\frac{dE^\alpha(f)}{df} = \sum_{i\sigma}\int d\mathbf{r}\,\frac{\delta E^\alpha}{\delta \phi_{i\sigma}^{\alpha *}(\mathbf{r})}\frac{d\phi_{i\sigma}^{\alpha *}(\mathbf{r})}{df} + \mathrm{h.c.} = \sum_{i\sigma}\epsilon_{i\sigma}^\alpha \int d\mathbf{r}\,\psi_{i\sigma}^\alpha(\mathbf{r})\frac{d\phi_{i\sigma}^{\alpha *}(\mathbf{r})}{df} + \mathrm{h.c.}, \tag{2.27}$$

where h.c. stands for hermitian conjugate. Considering that the wave functions $\psi_{i\sigma}^\alpha$ are normalized, then

$$\int d\mathbf{r}\,\psi_{i\sigma}^\alpha(\mathbf{r})\frac{d\phi_{i\sigma}^{\alpha *}(\mathbf{r})}{df} + \mathrm{h.c.} = \begin{cases} 1 & \text{if } \sigma = \sigma_{\mathrm{p}},\ i = i_{\mathrm{p}} \\ 0 & \text{else} \end{cases}. \tag{2.28}$$

Inserting Eq. (2.28) in Eq. (2.27), one obtains Eq. (2.25). Janak's theorem finds applications for calculating charge transition levels within density functional theory [75] and will be frequently used in this thesis.

2.6 Electrostatic corrections due to finite-size supercells

Density functional theory calculations subject to periodic boundary conditions represent the method of choice for studying defect properties [76]. However, in a supercell, the long-range nature of the electric field associated with a localized charge leads to spurious finite-size effects on defect formation energies [77, 78]. This limitation can be overcome by addressing various supercells of increasing size and extrapolating to the limit of an infinitely large supercell [78–82]. Since this method becomes prohibitive for large systems, it is preferable to apply *a posteriori* correction schemes [77, 78, 81, 83–85]. Such corrections depend quadratically on the extra electronic charge and scale inversely with the dielectric constant of the material.

Here, we illustrate the scheme introduced by Freysoldt, Neugebauer, and Van de Walle for addressing such spurious effects [77, 86]. Upon insertion of a defect density ρ_m of charge q in the system, a compensating background charge $-q/\Omega$ is generated, where Ω is the volume of the supercell. We denote V_m the potential generated by ρ_m, and $\tilde{V}_\mathrm{m}$ the potential generated by the periodic arrangement or ρ_m. Then, the spurious energy related to finite-size effects is given by two contributions. The first contribution arises from the interaction between the potential $\tilde{V}_\mathrm{m} - V_\mathrm{m}$ with the charge density ρ_m and the related compensating background charge. The other contribution arises from the interaction between ρ_m and the background charge. This results in the following corection energy to be added to the total energy from density functional theory calculations [77]

$$E_\mathrm{m} = -\left\{ \frac{1}{2} \int_\Omega d\mathbf{r} \left[\rho_\mathrm{m}(\mathbf{r}) - \frac{q}{\Omega} \right] [\tilde{V}_\mathrm{m}(\mathbf{r}) - V_\mathrm{m}(\mathbf{r})] - \frac{q}{\Omega} \int_\Omega d\mathbf{r}\, V_\mathrm{m}(\mathbf{r}) \right\}, \tag{2.29}$$

where the prefactor 1/2 accounts for double-counting effects. The potential V_m is then split into long-range and short-range contributions, namely

$$V_\mathrm{m} = V_\mathrm{m}^\mathrm{lr} + V_\mathrm{m}^\mathrm{sr}, \tag{2.30}$$

where the long-range potential V_m^lr is defined as

$$V_\mathrm{m}^\mathrm{lr}(\mathbf{r}) = \frac{1}{\varepsilon} \int d\mathbf{r}\, \frac{\rho_\mathrm{m}(\mathbf{r})}{|\mathbf{r} - \mathbf{r}'|}, \tag{2.31}$$

and the short range potential V_m^sr is calculated as $V_\mathrm{m} - V_\mathrm{m}^\mathrm{lr}$. Then, Eq. (2.29) can be rewritten as [77, 86]

$$E_\mathrm{m} = E_\mathrm{lat} - q\Delta V, \tag{2.32}$$

where E_lat and $q\Delta V$ are the lattice and alignment energies, respectively. The lattice energy E_{lat} is related to $V_{\mathrm{m}}^{\mathrm{lr}}$ and is given by

$$E_{\mathrm{lat}} = \frac{1}{2}\frac{1}{(2\pi)^3}\int_0^{|\mathbf{k}|\le G_{\mathrm{cut}}} \mathrm{d}\mathbf{k}\, \rho_{\mathrm{m}}(\mathbf{k})V_{\mathrm{m}}^{\mathrm{lr}}(\mathbf{k}) - \frac{1}{2}\frac{1}{\Omega}\sum_{\mathbf{G}\neq 0}^{|\mathbf{G}|<G_{\mathrm{cut}}} \rho_{\mathrm{m}}(\mathbf{G})V_{\mathrm{m}}^{\mathrm{lr}}(\mathbf{G}), \tag{2.33}$$

where $\mathbf{G}$ runs over the reciprocal lattice vectors with modulus lower than the cutoff G_{cut}. The divergent $\mathbf{G} = 0$ component is cancelled by the compensating background charge. The alignment term $q\Delta V$ is related to $V_{\mathrm{m}}^{\mathrm{sr}}$ and is given by

$$q\Delta V = q|V_{\mathrm{DFT}} - V_{\mathrm{m}}^{\mathrm{lr}}|_{\mathrm{far}}, \tag{2.34}$$

where V_{DFT} is the potential obtained through density functional theory calculations, and the difference is evaluated in a region far from the defect.

For a radial distribution ρ_{m}, and using the fact that

$$V_{\mathrm{m}}^{\mathrm{lr}}(\mathbf{k}) = \frac{4\pi}{\varepsilon}\frac{\rho_{\mathrm{m}}(\mathbf{k})}{|\mathbf{k}|^2}, \tag{2.35}$$

the lattice energy E_{lat} in Eq. (2.33) reduces to [86]

$$E_{\mathrm{lat}} = \frac{1}{\pi\varepsilon}\int_0^{G_{\mathrm{cut}}} dk\, \rho_{\mathrm{m}}^2(k) - \frac{2\pi}{\varepsilon\Omega}\sum_{\mathbf{G}\neq 0}^{|\mathbf{G}|\le G_{\mathrm{cut}}} \frac{\rho_{\mathrm{m}}^2(|\mathbf{G}|)}{|\mathbf{G}|^2}. \tag{2.36}$$

The charge distribution ρ_{m} is generally taken as a Gaussian distribution of width σ.

The finite-size corrections depend on the high-frequency and static dielectric constants of the system under consideration. Through the application of finite electric fields [87], the dielectric tensor $\boldsymbol{\varepsilon}$ can be calculated as

$$\varepsilon_{ij} = 1 + \frac{4\pi}{\Omega}\frac{dp_i}{de_j}, \tag{2.37}$$

where Ω is the volume of the supercell, e_j the electric field along the direction j, and p_i the polarization in the direction i. For the evaluation of the high frequency dielectric tensor $\boldsymbol{\varepsilon}_\infty$, the structure is kept fixed, such that the polarization arises only from electronic relaxation. At variance, for the calculation of the static dielectric tensor $\boldsymbol{\varepsilon}_0$, the structure is relaxed in the presence of the electric field, to account for both the electronic and the ionic screening. In the case of anisotropic screening, the dielectric constant ε is obtained from the trace of $\boldsymbol{\varepsilon}$ as $\varepsilon = \mathrm{Tr}(\boldsymbol{\varepsilon})/3$.

2.7 Nudged-elastic-band method

One relevant application of density functional theory consists in calculating transition rates for diffusion events or chemical reactions. The characteristic time scale of such transitions depends exponentially on the energy barrier between inital and final states. Hence, thermally-activated transitions can take very long molecular dynamics to be observed and therefore constitute a rare-event problem. To overcome such issue, one can focus on determining the path with highest statistical weight, which corresponds to the minimum energy path. This can be found by minimizing the forces orthogonal to the path in the configurational space, so that the energy is stationary along the direction perpendicular to the path. In the simplest case, the energy profile along the minimum energy path is represented by two minima connected by a maximum. Such maximum constitutes a saddle point and can be considered as the transition state. This allows one to determine energy barriers, thus overcoming the rare-event problem of determining transition rates through molecular dynamics.

A common approach for determining the minimal energy path consists in discretizing the path between two states into a series of images connected by springs. For simplicity, we here consider that all springs have the same stiffness. Then, one considers the following object function

$$\mathcal{S} = \sum_{m=1}^{M} E(\{\mathbf{R}_J^m\}) + \sum_{m=1}^{M}\sum_{I} \frac{Mk}{2}\left(\mathbf{R}_I^m - \mathbf{R}_I^{m-1}\right)^2, \tag{2.38}$$

where m is the image index, M the total number of images, I the atom index, $\mathbf{R}_I^m$ the Cartesian coordinate of the atom I in the m-th image, and k the spring constant. The minimization of such object function leads to the following forces

$$\mathbf{F}_I^m = -\nabla_I E(\{\mathbf{R}_J^m\}) + k\Big[(\mathbf{R}_I^{m+1} - \mathbf{R}_I^m) - (\mathbf{R}_I^m - \mathbf{R}_I^{m-1})\Big], \tag{2.39}$$

where the first and second terms on the right-hand side represent the Hellmann-Feynman force and the spring force acting on the atom I, respectively. This method does not however guarantee convergence towards the transition state. Indeed, the orthogonal component of the spring forces to the path can cause a path edge

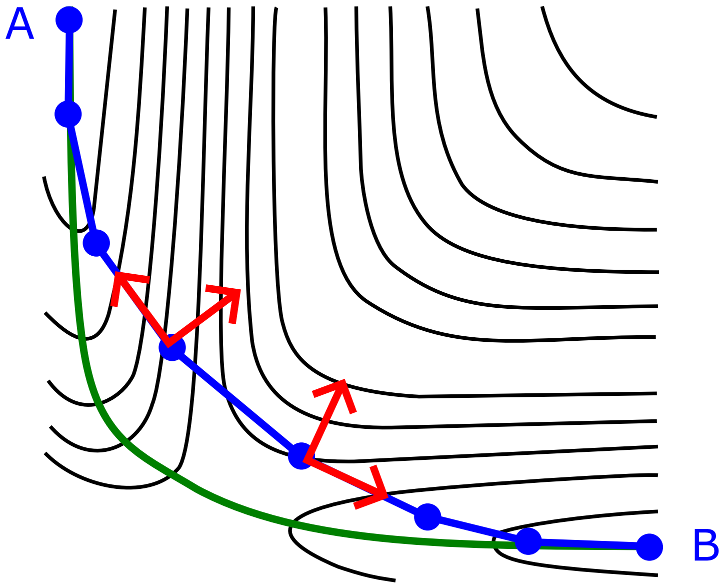

Figure 2.1 – Sketch of potential energy surface for a transition between two states A and B. In green the minimal energy path, in blue the path minimized with the forces in Eq. (2.39), in red the spring force perpendicular to the path and the Hellmann-Feynman force parallel to the path for two intermediate images.

cutting close to the transition state. Moreover, the Hellmann-Feynman forces have a components along the path, which can lead to a non-equidistance distribution of the images along the energy pathway and consequent sliding down of the images away from the barrier region. These two shortcomings are schematically illustrated in Fig. 2.1.

The nudged elastic band method allows one to determine the minimum energy path connecting two states [88, 89] overcoming the issues of corner cutting and sliding down images. This is achieved by projecting out the component of the spring force perpendicular to the path and the component of the Hellmann-Feynman force parallel to the path. This results in the following force acting on the atom I of the m-th image:

$$\begin{aligned}\mathbf{F}_I^m = &-\Big[\nabla_I E(\mathbf{R}^m) - \nabla_I E(\mathbf{R}^m)\cdot\mathbf{t}^m\mathbf{t}^m\Big]\\ &+ k\Big[(\mathbf{R}_I^{m+1} - \mathbf{R}_I^m) - (\mathbf{R}_I^m - \mathbf{R}_I^{m-1})\Big]\cdot\mathbf{t}^m\mathbf{t}^m,\end{aligned} \tag{2.40}$$

where $\mathbf{t}^m$ is the normalized tangent to the reaction path. We remark that the first and second contributions on the right-hand side of Eq. (2.40) represent the component of the Hellmann-Feynman force orthogonal to the path, and the component of the spring force parallel to the path. In this way, the optimization of the path is decoupled from the discrete representation of the path, which allows for a convergence towards the minimal energy path. Considering that the springs act only along the path, the choice of the spring constant is arbitrary. This represents a great advantage of the nudged-elastic-band method.

2.8 Polaron hopping rate

The rate of polaron charge transfer from the initial to the final state can be calculated using the Marcus-Emin-Holstein-Austin-Mott theory [90–94]. Depending on the coupling between the initial and final states, two regimes are distinguished: for large coupling the regime is adiabatic, for small coupling the regime is diabatic [95]. Depending on the regime, different analytic expressions for the polaron hopping rate have been derived [95]. Such expressions can be incorporated within the Landau-Zener formula [96, 97], and have largely been applied to polaron hopping processes [46, 98–113]. A schematical illustration of the energy profiles in these two regimes is given in Fig. 2.2, where the energy profile of the transition between two states is given as a function of a one-dimensional configurational coordinate Q. A common choice for Q is

$$(Q^n)^2 = \sum_I m_I |\mathbf{R}_I^n - \mathbf{R}_I^1|^2, \tag{2.41}$$

where n is the image index, and m_I the mass of atom I. The adiabatic energy profile can be obtained by performing nudged-elastic-band calculations.

Then, the charge transfer rate k_t for the hopping from an initial state to a final state can be calculated using the Landau-Zener formula [95–98], namely

$$k_\mathrm{t} = \kappa \nu \Gamma \exp\left(-\frac{E_\mathrm{a}}{k_\mathrm{B} T}\right), \tag{2.42}$$

where κ is the thermally-averaged electronic transmission coefficient, ν an effective nuclear frequency along the reaction coordinate, Γ the nuclear tunnelling factor, E_a the activation energy, and T the temperature. The tunnelling factor Γ takes into account the nuclear quantum effects and can generally be approximated as $\Gamma \approx 1$, except when considering low temperatures or light elements [108]. The effective

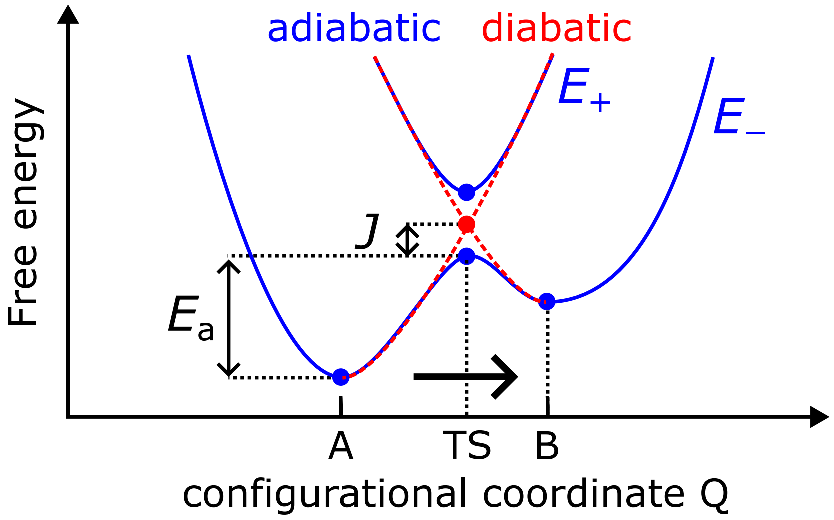

Figure 2.2 – Energy profile for electron transfer from the initial state A to the final state B along a configurational coordinate Q. The activation energy E_a, the coupling J between the two states, the lower and upper adiabatic energy surfaces E_- and E_+, and the transition state (TS) are indicated.

nuclear frequency ν can be calculated as [111]

$$\nu^2 = \frac{\partial^2 E(Q)}{\partial Q^2}, \tag{2.43}$$

and can be estimated from the nudged-elastic-band energy profile around the initial state within an effective one-dimensional phonon frequency approximation [114, 115]. We remark that presence of the atomic masses in Eq. (2.41) allows one to directly associate the right-hand side of Eq. (2.43) to the nuclear frequency ν. The transmission coefficient κ describes the transition probability from the initial state to the final state through multiple passages via the intersection point between the diabatic surfaces [95–98]. By denoting $(1 - P)$ the probability of the diabatic transition at the transition state from the low-energy adiabatic surface to the high-energy adiabatic surface and viceversa (cf. Fig. 2.2), κ can be expressed as [95–98]

$$\kappa = P + (1 - P)^2 \sum_{k=0}^{\infty} P^{2k+1} = \frac{2P}{1+P}, \tag{2.44}$$

where it is assumed that no transition occurs when the system falls back to the initial state [95]. The probability P is calculated as [95–98]

$$P = 1 - \exp\left[-\frac{\pi^2 J^2}{h\nu\sqrt{4\pi(E_\mathrm{a} + J)k_\mathrm{B}T}}\right], \tag{2.45}$$

where h is the Planck constant, k_B the Boltzmann constant, and J the coupling between initial and final states (cf. Fig. 2.2). We note that $E_\mathrm{a} + J$ corresponds to the diabatic activation energy, as schematically illustrated in Fig. 2.2. The coupling J can be calculated as the difference of the bonding and antibonding energy levels at the transition state [116]. For $P \to 1$ the regime is adiabatic, whereas the regime is diabatic for $P \to 0$.

3 Finite-size corrections of defect energy levels involving ionic polarization

We develop a scheme for finite-size corrections of vertical transition energies and single-particle energy levels involving defect states with built-in ionic polarization in supercell calculations, which is necessary for addressing the self-interaction problem for polarons. The method accounts on an equal footing for the screening of the electrons and of the ionic polarization charge arising from the lattice distortions. We demonstrate the accuracy of our corrections for various defects in MgO and in water by comparing with the dilute limit achieved through the scaling of the system size. The general validity of our formulation is also confirmed through a sum rule that connects vertical transition energies with the formation energies of structurally relaxed defects.

This chapter is adapted from:
Ref. [117]: S. Falletta, J. Wiktor, A. Pasquarello, *Finite-size corrections of defect energy levels involving ionic polarization*, Physical Review B 102, 041115(R) (2020).

3.1 Introduction

The suppression of the self-interaction of polarons requires one to consider the defect state without polaronic charge and with polaronic distortions. Similar states are of interest when dealing with vertical transitions involving defect states, which have gained attention in recent years for their potential in optoelectronic and photovoltaic applications [60, 118–120]. In this case, available model corrections [77, 83–85] cannot trivially be applied to vertical transitions, which involve defect charge states in the presence of a frozen lattice distortion.

For illustration, we consider in Fig. 3.1(b) the stability corresponding to the neutral state obtained upon vertical electron injection in the hole polaron state of MgO. While current schemes do not give any correction for neutral defects [77, 83–85], we observe noticeable scaling. Similarly, in Fig. 3.1(c), we show that the vertical extraction energy of the hydrated electron scales significantly with the system size, an effect that should be assigned to the neutral state as the negatively charged state is heavily screened ($\varepsilon_0 = 78.3$ at ambient conditions [121]). In the absence of a hydrated electron, the water dipoles remain oriented in a frozen geometry leading to a divergence of the ionic polarization [cf. Fig. 3.1(d)], which needs to be properly accounted for in correction schemes.

Since vertical transitions only involve electronic relaxations, the spurious interactions in the supercell are expected to be dominated by the high-frequency dielectric constant ε_∞. This generally leads to significantly larger corrections than for relaxed defects. For instance, in a recent study of transition energies in Ga_2O_3, the choice of the dielectric constant leads to differences up to 1 eV and the issue could not be solved by system size scaling because of the prohibitive computational cost [60].

3.2 Methodology

We generalize the notion of formation energy [76, 78] to account for a defect in the charge state q within a frozen geometry $\mathbf{R}_{q'}$ as induced by a charge q',

$$E_\mathrm{f}(q, \mathbf{R}_{q'}) = E(q, \mathbf{R}_{q'}) - E(0, \mathbf{R}_0) + q(\epsilon_\mathrm{F} + \epsilon_\mathrm{v}) - \sum_i n_i \mu_i + E_\mathrm{cor}(q, \mathbf{R}_{q'}), \quad (3.1)$$

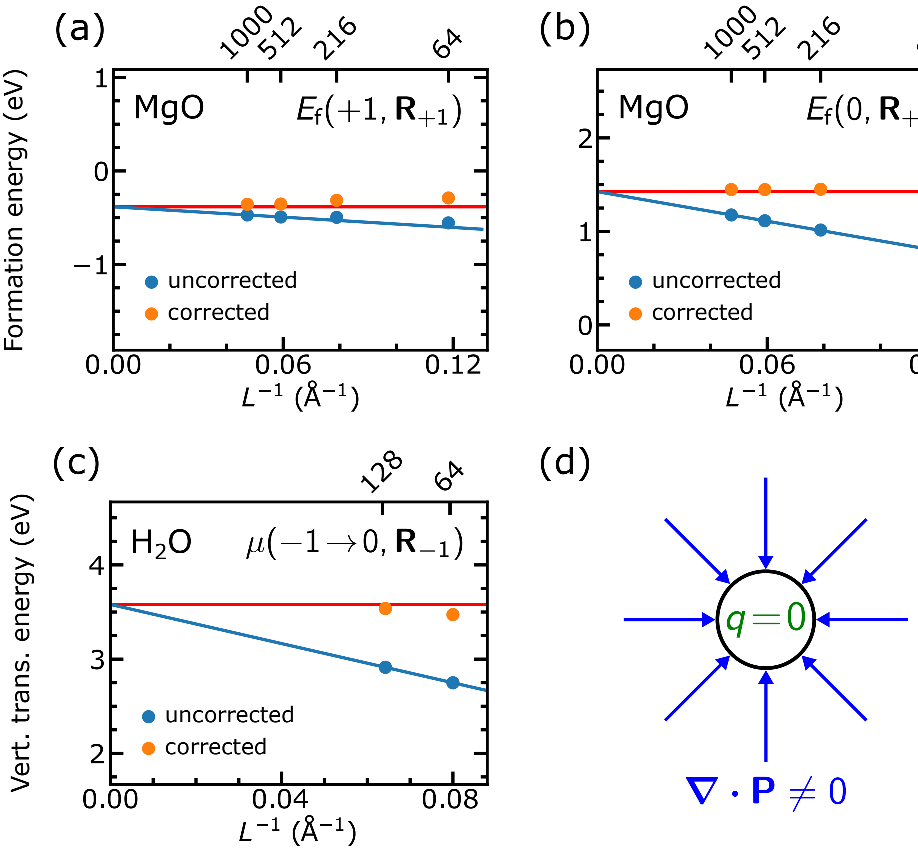

Figure 3.1 – Scalings with inverse supercell size L^{-1} for (a) the formation energy of the hole polaron in MgO (for $\epsilon_F = 0$), (b) the formation energy of the neutral defect in the geometry of the hole polaron in MgO, and (c) the vertical transition energy for the hydrated electron in water (non corrected values from Ref. [120]). The number of atoms or water molecules in the supercell is given at the top. The formation energies in the dilute limit are found by linear extrapolation of the two largest supercells and are indicated by horizontal red lines. (d) Schematics pointing to the presence of a divergence in the ionic polarization, $\nabla \cdot \mathbf{P} \neq 0$, due to lattice distortions, which cause finite-size effects even in the absence of an external charge ($q = 0$).

where $E(q, \mathbf{R}_{q'})$ and $E(0, \mathbf{R}_0)$ are total energies, ϵ_v is the valence band maximum, ϵ_F the Fermi level, n_i the number of atoms of species i involved in the defect, and μ_i the respective chemical potential. $E_{cor}(q, \mathbf{R}_{q'})$ corrects the finite-size effects and constitutes a crucial auxiliary quantity in our formulation.

The correction $E_{cor}(q, \mathbf{R}_q)$ for a defect in charge state q within a geometry relaxed in the presence of the same charge q can be expressed as

$$E_{cor}(q, \mathbf{R}_q) = E_m(q, \varepsilon_0), \tag{3.2}$$

where $E_\mathrm{m}(q, \varepsilon_0)$ corresponds to a regular model correction [77, 83–85] for an external charge q screened by the dielectric constant ε_0. Similarly, we define $E_\mathrm{m}(q, \varepsilon_\infty)$ as the model correction due to the sole electronic screening of the charge q through the high-frequency dielectric constant ε_∞. For instance, the latter correction applies to the case of a charge q in a neutral pristine lattice in which only electronic relaxation is allowed.

Here, we describe the effect of lattice distortions in the configuration $\mathbf{R}_{q'}$ by considering the ionic polarization charge q'_pol. This charge can be defined by setting the long-range screened potential $q'/(\varepsilon_0 r)$ equal to $(q' + q'_\mathrm{pol})/(\varepsilon_\infty r)$. This leads to

$$q'_\mathrm{pol} = -q'\left(1 - \frac{\varepsilon_\infty}{\varepsilon_0}\right). \tag{3.3}$$

When an external free charge amounting to $-q'_\mathrm{pol}$ is inserted at the defect site in the configuration $\mathbf{R}_{q'}$, the electronic polarization vanishes. Hence, the system $(-q'_\mathrm{pol}, \mathbf{R}_{q'})$ defined in this way can be used as a starting point for model finite-size corrections involving electronic screening, i.e. governed by ε_∞.

To find an expression for $E_\mathrm{cor}(q, \mathbf{R}_{q'})$, we construct the final state through a three-step procedure, as illustrated in Fig. 3.2. The first step $(0, \mathbf{R}_0) \rightarrow (q', \mathbf{R}_{q'})$ corresponds to the formation of a regularly relaxed defect of charge state q' and is hence described by a correction $E_\mathrm{m}(q', \varepsilon_0)$ [cf. Eq. (3.2)]. The second step $(q', \mathbf{R}_{q'}) \rightarrow (-q'_\mathrm{pol}, \mathbf{R}_{q'})$ needs a correction corresponding to $-E_\mathrm{m}(q' + q'_\mathrm{pol}, \varepsilon_\infty)$, where the minus sign results from the application of the model correction to the inverted step from $(-q'_\mathrm{pol}, \mathbf{R}_{q'})$ to $(q', \mathbf{R}_{q'})$ and $q' + q'_\mathrm{pol}$ represents the net localized charge to which the electrons respond. The use of ε_∞ is warranted by the purely electronic nature of the screening as the lattice structure $\mathbf{R}_{q'}$ is kept fixed. The last step $(-q'_\mathrm{pol}, \mathbf{R}_{q'}) \rightarrow (q, \mathbf{R}_{q'})$ leads to the final configuration $(q, \mathbf{R}_{q'})$ and needs a correction $E_\mathrm{m}(q + q'_\mathrm{pol}, \varepsilon_\infty)$, which can be justified analogously to the previous step.

Summing up the corrections pertaining to the three steps, we obtain the correction for a defect of charge q in the frozen equilibrium geometry pertaining to the charge state q',

$$E_\mathrm{cor}(q, \mathbf{R}_{q'}) = E_\mathrm{m}(q', \varepsilon_0) - E_\mathrm{m}(q' + q'_\mathrm{pol}, \varepsilon_\infty) + E_\mathrm{m}(q + q'_\mathrm{pol}, \varepsilon_\infty). \tag{3.4}$$

Equation (3.4) has a well defined physical meaning. Indeed, the difference between

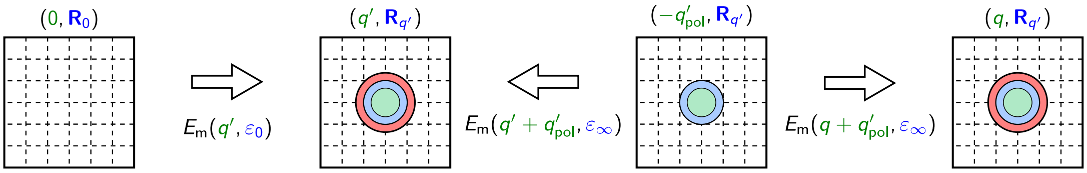
$(0, \mathbf{R}_0)$
$E_\mathrm{m}(q', \varepsilon_0)$
$(q', \mathbf{R}_{q'})$
$E_\mathrm{m}(q' + q'_\mathrm{pol}, \varepsilon_\infty)$
$(-q'_\mathrm{pol}, \mathbf{R}_{q'})$
$E_\mathrm{m}(q + q'_\mathrm{pol}, \varepsilon_\infty)$
$(q, \mathbf{R}_{q'})$

Figure 3.2 – Schematics for deriving the formula in Eq. (3.4). The external charge is shown in green, the ionic polarization charge in blue, and the electronic polarization charge in red. The system $(0, \mathbf{R}_0)$ does not show any localized polarization charge and can be used as the starting point for the application of model corrections involving ε_0. Similarly, $(-q'_\mathrm{pol}, \mathbf{R}_{q'})$ does not have any electronic polarization charge and can be used as the starting point for model corrections involving ε_∞.

the first two terms accounts for the finite-size effects due to the establishment of the ionic polarization charge q'_pol, while the last term results from the electronic response to the localized charge $q + q'_\mathrm{pol}$. Furthermore, our formula in Eq. (3.4) properly recovers the model corrections for regularly screened defects. When a charge q is in its relaxed structure $\mathbf{R}_q$, i.e., $q' = q$, the last two terms on the right-hand side of Eq. (3.4) cancel and the correction reduces to $E_\mathrm{m}(q, \varepsilon_0)$, as in Eq. (3.2). Similarly, when the charge q is added to a pristine lattice $\mathbf{R}_0$ without allowing for ionic relaxation, i.e., taking $q' = 0$ and hence $q'_\mathrm{pol} = 0$, the first two terms on the right-hand side of Eq. (3.4) vanish and $E_\mathrm{m}(q, \varepsilon_\infty)$ is correctly retrieved.

We now consider the vertical transition energy between the charge states q' and q in the geometry $\mathbf{R}_{q'}$,

$$\mu(q' \to q, \mathbf{R}_{q'}) = E_\mathrm{f}(q, \mathbf{R}_{q'}) - E_\mathrm{f}(q', \mathbf{R}_{q'}). \tag{3.5}$$

Using Eq. (3.4), we obtain the finite-size correction for this vertical transition,

$$\mu_\mathrm{cor}(q' \to q, \mathbf{R}_{q'}) = E_\mathrm{m}(q + q'_\mathrm{pol}, \varepsilon_\infty) - E_\mathrm{m}(q' + q'_\mathrm{pol}, \varepsilon_\infty), \tag{3.6}$$

where the terms due to the establishment of the ionic polarization charge q'_pol cancel and only the terms related with the electronic response to the net localized charge remain. When the charge q' in the initial configuration is neutral, our correction for the vertical transition in Eq. (3.6) becomes $E_\mathrm{m}(q, \varepsilon_\infty)$, which results from purely electronic screening. However, for the general case $q' \neq 0$, the expression in Eq. (3.6) shows that a complex interplay of ionic and electronic screening occurs.

The present formulation also opens the way to the corrections for single-particle defect levels. Such corrections find immediate application when calculating quasiparticle shifts in many-body GW formulations [122, 123] and when enforcing the generalized Koopmans' condition to defect states [40, 48, 60, 61, 65, 124]. The Kohn-Sham level ϵ of a defect of charge q in the geometry $\mathbf{R}_{q'}$ can be related to its total energy $E(q, \mathbf{R}_{q'})$ through Janak's theorem [75],

$$\epsilon(q, \mathbf{R}_{q'}) = -\lim_{Q\to q} \frac{\partial E(Q, \mathbf{R}_{q'})}{\partial Q}. \tag{3.7}$$

Using Eq. (3.4) and the quadratic dependence of $E_\mathrm{m}(q, \varepsilon)$ on q, we find that the corresponding finite-size correction ϵ_cor is expressed as

$$\epsilon_\mathrm{cor}(q, \mathbf{R}_{q'}) = -\frac{\partial E_\mathrm{cor}(q, \mathbf{R}_{q'})}{\partial q} = -\frac{\partial E_\mathrm{m}(q + q'_\mathrm{pol}, \varepsilon_\infty)}{\partial q}. \tag{3.8}$$

Considering the quadratic dependence of the model correction energy $E_\mathrm{m}(q, \varepsilon)$ on q [78, 86], one gets

$$\epsilon_\mathrm{cor}(q, \mathbf{R}_{q'}) = -2\frac{E_\mathrm{m}(q + q'_\mathrm{pol}, \epsilon_\infty)}{q + q'_\mathrm{pol}}. \tag{3.9}$$

For structurally relaxed defects, i.e. when $q' = q$, the formula in Eq. (3.9) falls back to the expression found by Chen and Pasquarello [125] in view of the relation in Eq. (3.3).

3.3 Results

The calculations are performed at the hybrid-functional level [53], as implemented in the CP2K code [126–130]. Goedecker-Teter-Hutter pseudopotentials [127, 128] are used to describe the electron core-valence interactions. Calculations are performed with double-ζ MOLOPT Gaussian basis sets [129]. The Brillouin zone is sampled at the sole Γ-point. The energy cutoff for the plane waves is set to 800 Ry. We use a dielectric dependent hybrid functional defined by the one-parameter PBE0 functional [53], in which we fix the fraction of exact exchange at $\alpha = 1/\varepsilon_\infty$. For MgO, we use the experimental value of $\varepsilon_\infty = 3.0$ [131], resulting in $\alpha = 0.33$. This choice gives a fundamental band gap of 7.8 eV, in excellent agreement with the experimental value of 7.83 eV [132]. The hybrid functional calculations are accelerated through the use of the auxiliary density matrix method, in which cFIT3 auxiliary basis set is used for the Gaussian functions [130]. By applying a finite electric field [87] to the largest supercell under consideration (1000 atoms), we determine $\varepsilon_0 = 8.6$ and $\varepsilon_\infty = 2.5$, in agreement with the experimental values $\varepsilon_0^{\text{expt}} = 9.8$ [133] and $\varepsilon_\infty^{\text{expt}} = 3.0$ [131]. As the model correction E_{m} for regularly screened defects, we adopt the method introduced by Freysoldt, Neugebauer, and Van de Walle (FNV) [77].

In Fig. 3.1(b), we illustrate the quality of our correction scheme for the formation energy $E_{\text{f}}(0, \mathbf{R}_{+1})$ of the neutral charge state in the geometry of the hole polaron. In the case of the oxygen vacancy, we consider $E_{\text{f}}(q, \mathbf{R}_{q'})$ for $q, q' = 0, +1, +2$, resulting in eight cases excluding $E_{\text{f}}(0, \mathbf{R}_0)$, which we take as the reference. Figure 3.3 shows the scaling towards the dilute limit in the cases in which standard correction schemes cannot be applied. Excluding the case of the relatively small 64-atom supercells, the errors of the corrected formation energies with respect to the extrapolated value in the dilute limit are smaller than 0.16 eV in all cases.

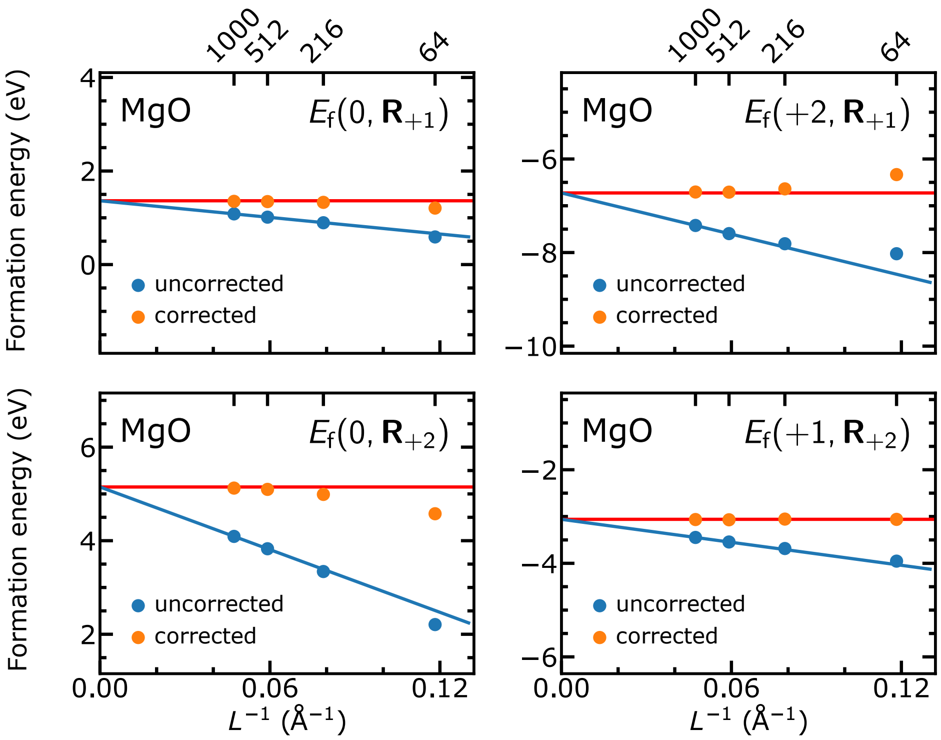

Figure 3.3 – Formation energies of various states $(q, \mathbf{R}_{q'})$ of the oxygen vacancy in MgO as a function of the inverse supercell size L^{-1}. The number of atoms in the supercell is given at the top. The formation energies in the dilute limit are found by linear extrapolation of the two largest supercells and are indicated by horizontal red lines. In charged systems, we take $\epsilon_{\text{F}} = 0$.

Similar errors are found for the FNV scheme applied to the formation energies of regularly screened oxygen vacancies (cf. Fig. 3.4), in agreement with the literature [78]. This is illustrated in Fig. 3.4, where we show the scaling towards the dilute limit of the formation energies of regularly screened defects. The error with respect to the dilute limit becomes negligible for sufficiently large supercells.

In Fig. 3.5, we illustrate the vertical transition energies obtained for the 64-atom supercell of MgO. This highlights the importance of accounting for finite-size corrections when considering configurational diagrams. Additionally, Fig. 3.6(a) shows the performance of the scheme by Chen and Pasquarello [125] applied to the regularly relaxed hole polaron in MgO ($q = q' = +1$). Figure 3.6(b) illustrates

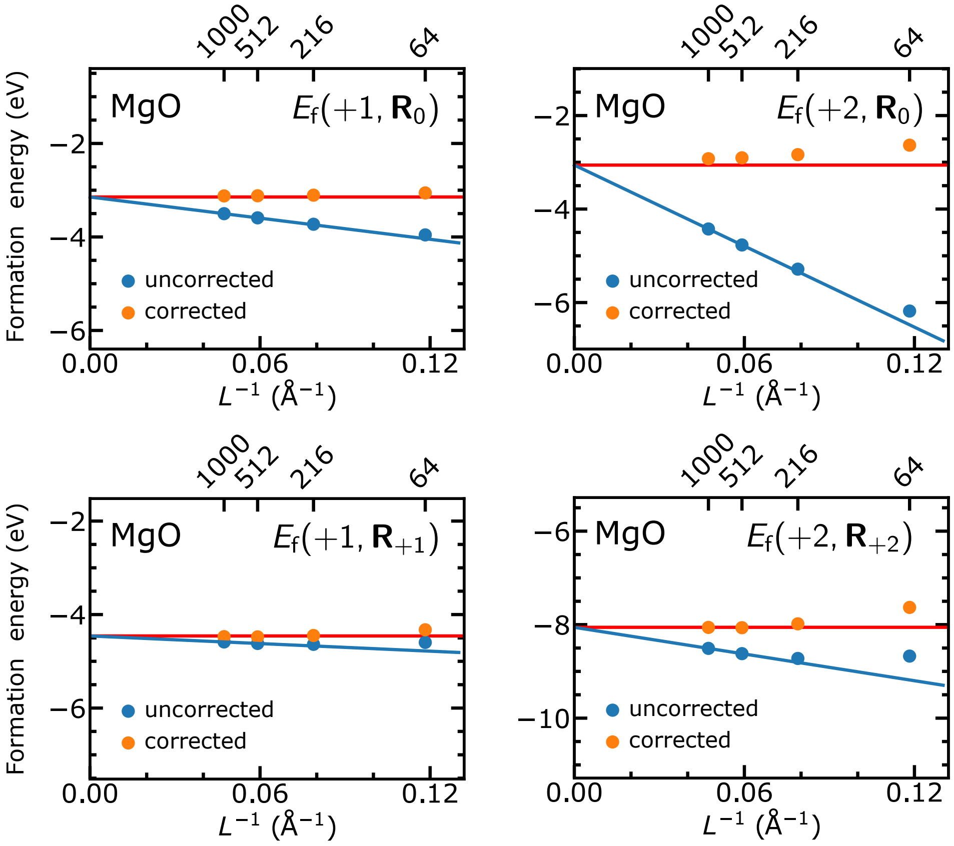

Figure 3.4 – Formation energies of regularly screened defect states of the oxygen vacancy in MgO as function of the inverse supercell size L^{-1}. The corrections are performed with the FNV model correction scheme [77]. The number of atoms in the supercell is given at the top. The formation energies in the dilute limit are found by linear extrapolation of the two largest supercells and are indicated by horizontal red lines. In all these cases, we take the Fermi level $\epsilon_\mathrm{F} = 0$.

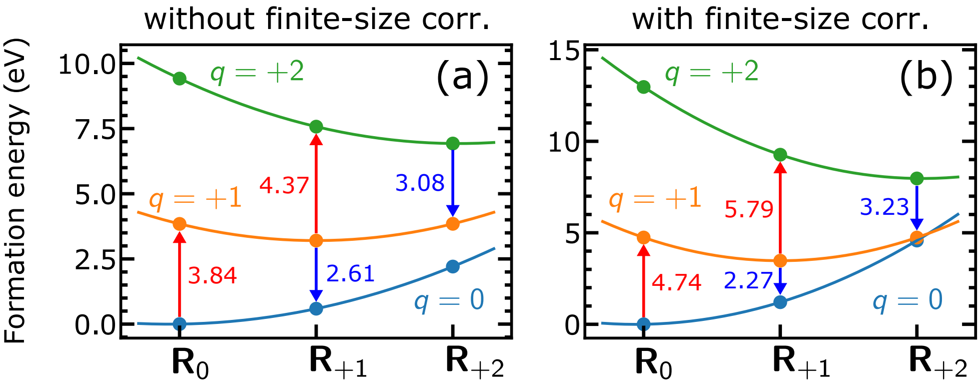

Figure 3.5 – Vertical transition energies for the O vacancy in MgO (64 atoms) (a) without and (b) with finite-size corrections.

the accuracy of the present finite-size correction scheme applied to the charged and neutral states of the hole polaron in MgO, in which a built-in polarization is present. The errors with respect to the dilute limit in the two cases are similar, thereby supporting the validity of our formulation.

The scaling behavior here studied is affected not only by the finite-size of the simulation cell but also by the varying accuracy of the **k**-point sampling. However, the consideration of large band-gap materials, such as MgO and liquid water,

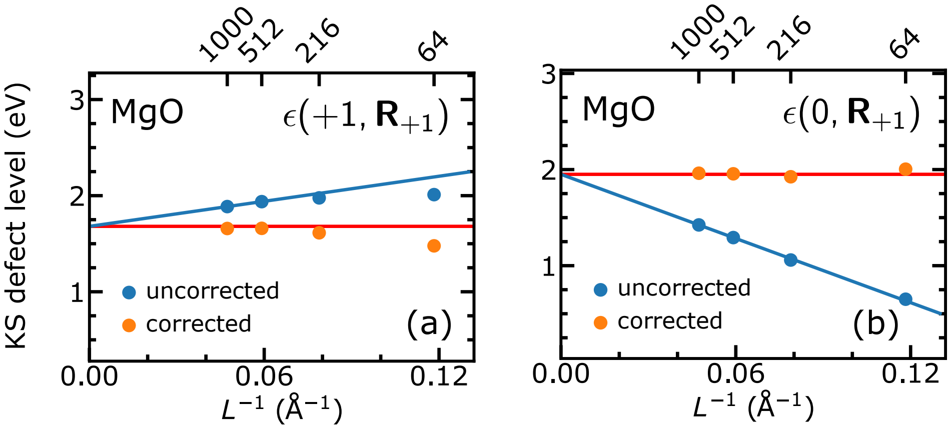

Figure 3.6 – Kohn-Sham defect levels ϵ of the charged (a) and neutral (b) hole polaron in MgO as a function of the inverse supercell size L^{-1}. The defect levels are referred to the valence bands of the pristine system. In both cases, we use the correction formula given in Eq. (11) of the main text, which corresponds to that of Chen and Pasquarello [125] in the case of the positively charged state. The number of atoms in the supercell is given at the top. The defect levels in the dilute limit are found by linear extrapolation of the two largest supercells and are indicated by horizontal red lines.

ensures that the effect from the latter is negligible. For the hole polaron in the 64-atom supercell, we verified that a **k**-point sampling involving the sole Γ point gives results within only 0.07 eV from the fully converged sampling. This effect becomes fully negligible for the larger supercells.

3.4 Ionic polarization charge

To highlight the role of the ionic polarization charge q'_{pol}, we focus on the $(0, \mathbf{R}_{+1})$ state of the oxygen vacancy in MgO, in which the localized charge is solely provided by the ionic polarization. In Fig. 3.7(a), we display the potential V_{DFT} obtained from the hybrid functional calculation. We compare the latter with the long-range model potential associated with a charge q'_{pol} screened by ε_∞,

$$V_{\mathrm{m}}^{\mathrm{lr}}(\mathbf{r}; q'_{\mathrm{pol}}, \varepsilon_\infty) = \frac{1}{\varepsilon_\infty} \int \mathrm{d}\mathbf{r}' \frac{\rho_{\mathrm{m}}(\mathbf{r}'; q'_{\mathrm{pol}})}{|\mathbf{r} - \mathbf{r}'|}, \tag{3.10}$$

where $\rho_{\mathrm{m}}(\mathbf{r}'; q'_{\mathrm{pol}})$ represents a Gaussian distribution of charge q'_{pol}. Figure 3.7(a) shows that V_{DFT} is well described by V_{m} in the long range, supporting the description of the ionic polarization in terms of the charge q'_{pol}. The role of q'_{pol} can be further emphasized by displaying the finite-size errors with respect to the dilute limit for $E_{\mathrm{f}}(q, \mathbf{R}_{+1})$, where the charge states $q = 0, +1, +2$ are considered in the presence of the same frozen configuration $\mathbf{R}_{+1}$. In Fig. 3.7(b), we display these errors for every considered supercell size and interpolate them with parabola. When the supercells are sufficiently large, the minima of these parabola occur at charge $-q'_{\mathrm{pol}}$ pertaining to $\mathbf{R}_{+1}$. This is consistent with our finite-size expression in Eq. (3.4), since the third term $E_{\mathrm{m}}(q + q'_{\mathrm{pol}}, \varepsilon_\infty)$ is quadratic in the localized charge [77, 83–85] and is thus minimized for $q = -q'_{\mathrm{pol}}$. At the minimum the electronic polarization is absent, but the correction does not vanish because of the first two terms in Eq. (3.4), which correspond to the establishment of the ionic polarization in the geometry $\mathbf{R}_{+1}$. Figures 3.7(c-d) corresponds to the same analysis for the O vacancy in MgO as illustrated in Fig. 3.7(b) but for the lattice configurations relaxed in the presence of a charge $q' = 0, +2$.

As a second case study, we focus on the vertical extraction energy of the hydrated electron. In the final state, the system is neutral but the structure of liquid water presents a strong dipolar polarization giving rise to significant finite-size effects (cf. Fig. 3.1) [120]. We take uncorrected data for the vertical transition $\mu(-1 \to 0, \mathbf{R}_{-1})$

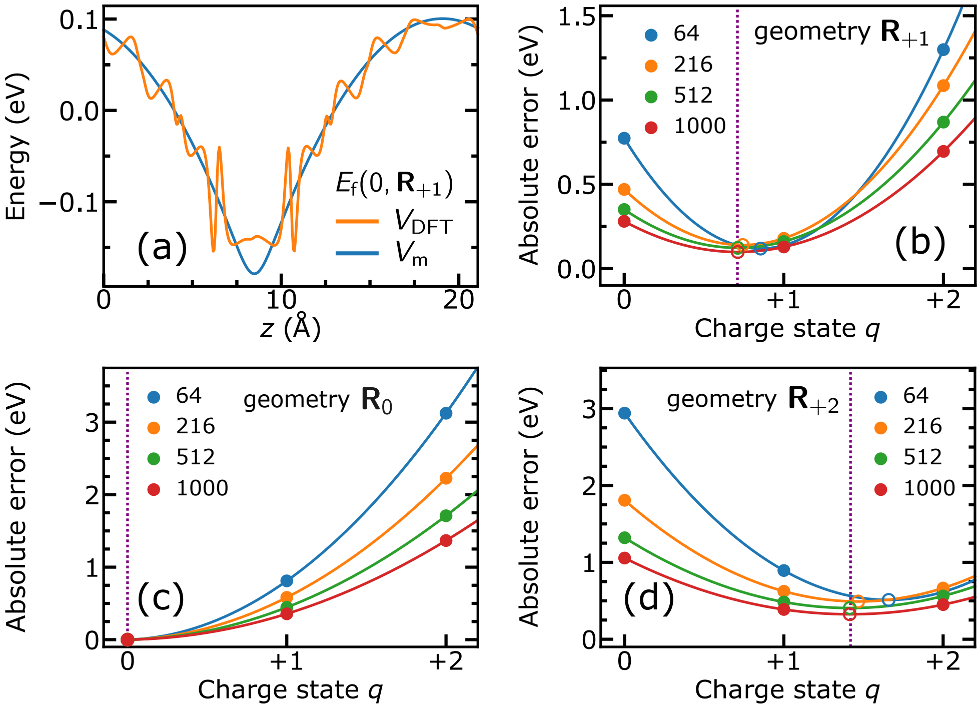

Figure 3.7 – (a) Comparison between the potential V_{DFT} obtained from the hybrid functional calculation for the $(0, \mathbf{R}_{+1})$ state of the O vacancy in MgO and the model potential $V_{\mathrm{m}}(\mathbf{r}; q'_{\mathrm{pol}}, \varepsilon_\infty)$ resulting from a Gaussian distribution of charge $q'_{\mathrm{pol}} = -(1 - \varepsilon_\infty/\varepsilon_0)$ with a width of 1 bohr. (b-d) Absolute finite-size error with respect to the dilute limit for $E_{\mathrm{f}}(q, \mathbf{R}_{q'})$ with $q = 0, +1, +2$ and $q' = 0, +1, +2$ (solid circles). Supercells based on various numbers of atoms are considered. The data are interpolated with parabola and the obtained minima are indicated with open circles. The vertical line indicates the charge $-q'_{\mathrm{pol}}$ and corresponds to the theoretical minimum of the finite-size correction for $\mathbf{R}_{q'}$.

calculated in Ref. [120] and apply our scheme based on FNV model corrections for E_{m} [77, 86, 125]. We use static and high-frequency dielectric constants inferred from experimental data ($\varepsilon_0 = 78.3$ [121] and $\varepsilon_\infty = 1.78$ [134]). Compared to the extrapolated limit, our corrected transition energies show errors of 0.11 and 0.04 eV for supercells containing 64 and 128 water molecules, respectively, thereby further supporting the accuracy of our scheme [cf. Fig. 3.1(c)].

3.5 Sum rule from thermodynamic integration

To corroborate the general validity of our formulation, we show that the finite-size corrections for vertical transition energies in Eq. (3.6) satisfy a sum rule that connects them to standard corrections of structurally relaxed defects [cf. Eq.

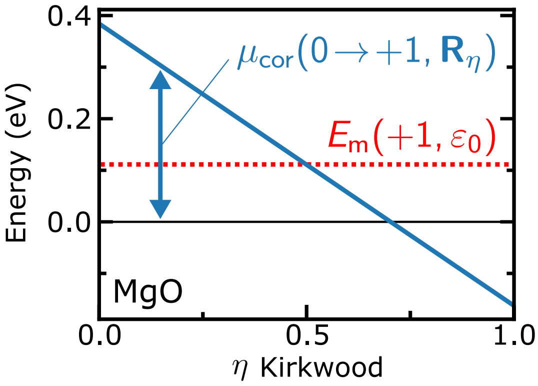

Figure 3.8 – Illustration of the sum rule defined in Eq. (3.13) for a transition between the defect charge states of $q'=0$ and $q=+1$ in a 1000-atom supercell of MgO. For each value of the Kirkwood parameter η, the correction $\mu_{\rm cor}(0\to+1,\mathbf{R}_\eta)$ is evaluated through Eq. (3.6). The mean value of $\mu_{\rm cor}(0\to+1,\mathbf{R}_\eta)$ (red line) equals $E_{\rm m}(+1,\varepsilon_0)$.

(3.2)]. To derive the sum rule, we adopt a procedure commonly utilized in the framework of the thermodynamic integration method [135–137]. To describe the transition from the charge state q' to that of q, we introduce a fictitious Hamiltonian $\mathcal{H}_\eta=\eta\mathcal{H}_q+(1-\eta)\mathcal{H}_{q'}$, where η is the Kirkwood parameter [138], and $\mathcal{H}_{q'}$ and $\mathcal{H}_q$ are the Hamiltonians associated to the initial and final states, respectively. This leads to

$$E(q,\mathbf{R}_q)-E(q',\mathbf{R}_{q'})=\int_0^1 d\eta\;\mu(q'\to q,\mathbf{R}_\eta), \tag{3.11}$$

where the terms on the left-hand side correspond to equilibrium energies of relaxed defects, whereas the integrand on the right-hand side is the vertical transition energy defined in Eq. (3.5). This leads to the following relationship between the corresponding finite-size corrections,

$$E_{\rm m}(q,\varepsilon_0)-E_{\rm m}(q',\varepsilon_0)=\int_0^1 d\eta\;\mu_{\rm cor}(q'\to q,\mathbf{R}_\eta). \tag{3.12}$$

It can be proven that this relationship is generally satisfied by our finite-size corrections for vertical charge transition energies. The proof uses the quadratic dependence of the model correction $E_{\rm m}(q,\varepsilon)$ on q and the linearity of the model potential $V_{\rm m}(\mathbf{r};q,\varepsilon)$ in q. In Fig. 3.8, we illustrate the relationship between the finite-size corrections in Eq. (3.13) for a transition from $q'=0$ to $q=+1$ in MgO.

Without loss of generality, we here explicitly demonstrate the validity of the sum rule in case of FNV model corrections [77]. We start by inserting the expression of μ_{cor} given in Eq. (3.6) into Eq. (3.13), namely

$$E_{\mathrm{m}}(q,\varepsilon_0) - E_{\mathrm{m}}(q',\varepsilon_0) = \int_0^1 d\eta \left[E_{\mathrm{m}}(q+q_{\mathrm{pol}}^{\eta},\varepsilon_\infty) - E_{\mathrm{m}}(q'+q_{\mathrm{pol}}^{\eta},\varepsilon_\infty)\right], \tag{3.13}$$

where $q_{\mathrm{pol}}^{\eta} = \eta q_{\mathrm{pol}} + (1-\eta)q'_{\mathrm{pol}}$. The ionic polarization charges q_{pol} and q'_{pol} correspond to the defect states $(q,\mathbf{R}_q)$ and $(q',\mathbf{R}_{q'})$, respectively. From the definition of the ionic polarization charge in Eq. (3.3), it follows that $\rho_{\mathrm{m}}(q_{\mathrm{pol}}) = -\rho_{\mathrm{m}}(q)(1-\varepsilon_\infty/\varepsilon_0)$.

Next, considering that $E_{\mathrm{m}} = E_{\mathrm{lat}} - q\Delta V$ [cf. Eq. (2.33)], we can decompose Eq. (3.13) in two separate equations, for the lattice energy E_{lat} and for the alignment term $q\Delta V$, respectively. For the lattice energy terms, we get

$$\begin{aligned}\rho_{\mathrm{m}}(q)V_{\mathrm{m}}^{\mathrm{lr}}(q,\varepsilon_0) - \rho_{\mathrm{m}}(q')V_{\mathrm{m}}^{\mathrm{lr}}(q',\varepsilon_0) = \int_0^1 d\eta \Big\{&[\rho_{\mathrm{m}}(q)+\rho_{\mathrm{m}}(q_{\mathrm{pol}}^{\eta})]V_{\mathrm{m}}^{\mathrm{lr}}(q+q_{\mathrm{pol}}^{\eta},\varepsilon_\infty)\\ &-[\rho_{\mathrm{m}}(q')+\rho_{\mathrm{m}}(q_{\mathrm{pol}}^{\eta})]V_{\mathrm{m}}^{\mathrm{lr}}(q'+q_{\mathrm{pol}}^{\eta},\varepsilon_\infty)\Big\}.\end{aligned} \tag{3.14}$$

Using the explicit expression of the model potential $V_{\mathrm{m}}^{\mathrm{lr}}$ in Eq. (2.31), Eq. (3.14) becomes

$$\begin{aligned}\frac{\rho_{\mathrm{m}}(q)^2}{\varepsilon_0} - \frac{\rho_{\mathrm{m}}(q')^2}{\varepsilon_0} &= \frac{1}{\varepsilon_\infty}\int_0^1 d\eta \left\{\left[\rho_{\mathrm{m}}(q)+\rho_{\mathrm{m}}(q_{\mathrm{pol}}^{\eta})\right]^2 - \left[\rho_{\mathrm{m}}(q')+\rho_{\mathrm{m}}(q_{\mathrm{pol}}^{\eta})\right]^2\right\}\\ &= \frac{1}{\varepsilon_\infty}\left\{\rho_{\mathrm{m}}(q)^2 - \rho_{\mathrm{m}}(q')^2 + 2\left[\rho_{\mathrm{m}}(q)-\rho_{\mathrm{m}}(q')\right]\int_0^1 d\eta\ \rho_{\mathrm{m}}(q_{\mathrm{pol}}^{\eta})\right\}.\end{aligned} \tag{3.15}$$

Using the relation $\rho_{\mathrm{m}}(q_{\mathrm{pol}}^{\eta}) = \eta\rho_{\mathrm{m}}(q_{\mathrm{pol}}) + (1-\eta)\rho_{\mathrm{m}}(q'_{\mathrm{pol}})$ and performing the integration in η, we obtain

$$\begin{aligned}\frac{\rho_{\mathrm{m}}(q)^2}{\varepsilon_0} - \frac{\rho_{\mathrm{m}}(q')^2}{\varepsilon_0} &= \frac{1}{\varepsilon_\infty}\Big\{\rho_{\mathrm{m}}(q)^2 - \rho_{\mathrm{m}}(q')^2 + [\rho_{\mathrm{m}}(q)-\rho_{\mathrm{m}}(q')][\rho_{\mathrm{m}}(q_{\mathrm{pol}})+\rho_{\mathrm{m}}(q'_{\mathrm{pol}})]\Big\}\\ &= \frac{1}{\varepsilon_\infty}\Big\{\rho_{\mathrm{m}}(q)^2 - \rho_{\mathrm{m}}(q')^2 - \left(1-\frac{\varepsilon_\infty}{\varepsilon_0}\right)\Big[\rho_{\mathrm{m}}(q)^2 - \rho_{\mathrm{m}}(q')^2\Big]\Big\}\\ &= \frac{\rho_{\mathrm{m}}(q)^2}{\varepsilon_0} - \frac{\rho_{\mathrm{m}}(q')^2}{\varepsilon_0}.\end{aligned} \tag{3.16}$$

Therefore, Eq. (3.13) is satisfied for the lattice energy terms.

For the alignment terms, Eq. (3.13) is satisfied when

$$q\Delta V(q,\varepsilon_0) - q'\Delta V(q',\varepsilon_0) = \int_0^1 d\eta \left\{(q+q_{\text{pol}}^{\eta})\Delta V(q+q_{\text{pol}}^{\eta},\varepsilon_\infty) - (q'+q_{\text{pol}}^{\eta})\Delta V(q'+q_{\text{pol}}^{\eta},\varepsilon_\infty)\right\}. \tag{3.17}$$

Using the linearity of the alignment term with respect to the charge distribution [78], the latter becomes

$$\begin{aligned} q\Delta V(q,\varepsilon_0) - q'\Delta V(q',\varepsilon_0) = {}& q\Delta V(q,\varepsilon_\infty) - q'\Delta V(q',\varepsilon_\infty) \\ &+ (q-q')\int_0^1 d\eta\ \Delta V(q_{\text{pol}}^{\eta},\varepsilon_\infty) \\ &+ [\Delta V(q,\varepsilon_\infty) - \Delta V(q',\varepsilon_\infty)]\int_0^1 d\eta\ q_{\text{pol}}^{\eta}. \end{aligned} \tag{3.18}$$

Using the fact that $q_{\text{pol}}^{\eta} = \eta q_{\text{pol}} + (1-\eta)q'_{\text{pol}}$ and the linearity of the alignment term with respect to the charge density, Eq. (3.18) can be rewritten as

$$\begin{aligned} q\Delta V(q,\varepsilon_0) - q'\Delta V(q',\varepsilon_0) = {}& q\Delta V(q,\varepsilon_\infty) - q'\Delta V(q',\varepsilon_\infty) \\ &+ \frac{1}{2}(q-q')[\Delta V(q_{\text{pol}},\varepsilon_\infty) + \Delta V(q'_{\text{pol}},\varepsilon_\infty)] \\ &+ \frac{1}{2}[\Delta V(q,\varepsilon_\infty) - \Delta V(q',\varepsilon_\infty)](q_{\text{pol}} + q'_{\text{pol}}). \end{aligned} \tag{3.19}$$

Finally, re-elaborating Eq. (3.19), we get

$$q\Delta V(q,\varepsilon_0) - q'\Delta V(q',\varepsilon_0) = q\Delta V(q+q_{\text{pol}},\varepsilon_\infty) - q'\Delta V(q'+q'_{\text{pol}},\varepsilon_\infty), \tag{3.20}$$

which is satisfied by definition of q_{pol}. This concludes our proof of Eq. (3.13).

3.6 Comparison with previous literature

In Tables 3.1 and 3.2, we report the finite-size errors with respect to the dilute limit for all the defect states in MgO and H_2O considered in this work. It is seen that the mean percentage errors defined as the ratio of the corrected and uncorrected errors generally decrease with increasing supercell size.

Table 3.1 – Errors with respect to the dilute limit (DL) of formation energies for the hole polaron and the oxygen vacancy in MgO, with (δ_{cor}) and without (δ_{uncor}) the finite-size energy corrections. We use the correction formula derived in this work with FNV model corrections [77]. The footnotes specify when they are equivalent to model correction schemes for regularly screened defects. The mean percentage errors (MPE) defined as the average $\delta_{\mathsf{cor}}/\delta_{\mathsf{uncor}}$ for a given supercell size are reported. All energies are in eV.

			64 atoms		216 atoms		512 atoms		1000 atoms	
		DL	δ_{uncor}	δ_{cor}	δ_{uncor}	δ_{cor}	δ_{uncor}	δ_{cor}	δ_{uncor}	δ_{cor}
hole polaron	$E_{\mathrm{f}}(+1,\mathbf{R}_{+1})^{\mathrm{I}}$	−0.384	−0.172	0.094	−0.113	0.069	−0.109	0.030	−0.087	0.027
	$E_{\mathrm{f}}(0,\mathbf{R}_{+1})$	1.425	−0.663	0.006	−0.411	0.025	−0.311	0.022	−0.249	0.022
	MPE		27.8%		33.7%		17.2%		19.9%	
O vacancy	$E_{\mathrm{f}}(+1,\mathbf{R}_{0})^{\mathrm{II}}$	−3.145	−0.811	0.087	−0.583	0.039	−0.446	0.026	−0.357	0.023
	$E_{\mathrm{f}}(+2,\mathbf{R}_{0})^{\mathrm{II}}$	−3.060	−3.122	0.427	−2.226	0.223	−1.709	0.155	−1.367	0.136
	$E_{\mathrm{f}}(0,\mathbf{R}_{+1})$	1.364	−0.773	−0.156	−0.470	−0.034	−0.350	−0.017	−0.280	−0.012
	$E_{\mathrm{f}}(+1,\mathbf{R}_{+1})^{\mathrm{I}}$	−4.458	−0.138	0.125	−0.179	0.010	−0.160	−0.020	−0.128	−0.015
	$E_{\mathrm{f}}(+2,\mathbf{R}_{+1})$	−6.726	−1.299	0.379	−1.085	0.087	−0.869	0.017	−0.695	0.020
	$E_{\mathrm{f}}(0,\mathbf{R}_{+2})$	5.148	−2.941	−0.571	−1.807	−0.159	−1.320	−0.051	−1.056	−0.024
	$E_{\mathrm{f}}(+1,\mathbf{R}_{+2})$	−3.059	−0.894	−0.008	−0.624	0.005	−0.484	−0.010	−0.388	−0.005
	$E_{\mathrm{f}}(+2,\mathbf{R}_{+2})^{\mathrm{I}}$	−8.057	−0.616	0.412	−0.666	0.074	−0.563	−0.008	−0.450	−0.002
	MPE		31.5%		7.2%		5.2%		4.9%	

Table 3.2 – Errors with respect to the dilute limit (DL) of the vertical excitation energy μ of the hydrated electron in water, with (δ_{cor}) and without (δ_{uncor}) finite-size energy corrections. We use the correction formula derived in this work with FNV model corrections [77]. The Gaussian distribution of the model charge has a width corresponding to the gyration radius of the hydrated electron (2.49 Å, Ref. [120]) to ensure a vanishing alignment term [86, 125]. The mean percentage errors (MPE) defined as the average $\delta_{\mathsf{cor}}/\delta_{\mathsf{uncor}}$ for a given supercell size are reported. All energies are in eV.

			64 molecules		128 molecules	
		DL	δ_{uncor}	δ_{cor}	δ_{uncor}	δ_{cor}
hydrated e^-	$\mu(-1 \to 0,\mathbf{R}_{-1})$	3.581	−0.832	−0.108	−0.668	−0.044
	MPE		13.0%		6.6%	

In Table 3.3, we compare uncorrected and corrected vertical transitions with previous results in the literature for the hole polaron [39] and the oxygen vacancy [139] in MgO. We used a simulation cell of 216 atoms for the hole polaron and of 64 atoms for the oxygen vacancy to enable comparisons with the results in Refs. [39, 139]. Generally, the difference between corrected and uncorrected results is sizable demonstrating the usefulness of our correction scheme. The differences between our values and the values in the literature [39, 139] result from different correction schemes but also from different computational setups, which make a detailed comparison difficult.

Table 3.3 – Vertical transition energies for the hole polaron and the oxygen vacancy in MgO, uncorrected and corrected using our scheme. It is specified whether ϵ_F is taken at the conduction band minimum (CBM) or at the valence band maximum (VBM). A comparison with previously calculated values is reported. The simulation cell contains 216 atoms for the hole polaron and 64 atoms for the oxygen vacancy. All energies are in eV.

		ϵ_F	Uncorrected	Corrected	Previous
hole polaron	$\mu(+1 \rightarrow 0, \mathbf{R}_{+1})$	VBM	1.32	1.72	1.15[I]
		CBM	6.48	6.08	6.8[I]
O vacancy	$\mu(0 \rightarrow +1, \mathbf{R}_0)$	VBM	−3.96	−3.06	−2.7[II]
		CBM	3.84	4.74	5.4[II]
	$\mu(+1 \rightarrow 0, \mathbf{R}_{+1})$	VBM	5.19	5.53	4.3[II]
		CBM	−2.61	−2.27	−3.8[II]
	$\mu(+1 \rightarrow +2, \mathbf{R}_{+1})$	VBM	−3.43	−2.01	−2.6[II]
		CBM	4.37	5.79	5.5[II]
	$\mu(+2 \rightarrow +1, \mathbf{R}_{+2})$	VBM	4.72	4.57	4.0[II]
		CBM	−3.08	−3.23	−4.1[II]

I Ref. [39], II Ref. [139].

3.7 Discussion

In conclusion, we derived finite-size corrections for vertical transition energies and single-particle energy levels involving defect states with built-in ionic polarization. The present formulation is fully general and applies to defect states in condensed systems ranging from the solid to the liquid state. Its physical motivation is transparent and the limiting cases are trivially recovered. Our method allows for the combination with existing schemes for regularly relaxed defects, making its implementation and use widely accessible [140]. Our corrections are validated through numerical case studies in MgO and water and through the analytical condition set by a sum rule. This scheme allows one to achieve accurate optical transition energies for identifying defect signatures in measured optical spectra without requiring computationally prohibitive system-size scalings.

4 Polarons modelled through hybrid functionals

We study polarons free from many-body self-interaction using hybrid functionals. First, we present the notion of polaron formation energy in relation to Janak's theorem, and discuss practical ways through which the piecewise linearity of the total energy can be enfoced. We demonstrate that hybrid functionals stabilize polarons, as opposed to semilocal density functionals. Then, we show that piecewise linear hybrid functionals lead to an overall improvement of the electronic structure, yielding accurate band gaps when compared to experiment. As test cases, we consider the electron polaron in $BiVO_4$, the hole polaron in MgO, and the Al-trapped hole in α-SiO_2.

This chapter is adapted from:
Ref. [141]: S. Falletta, A. Pasquarello, *Many-body self-interaction and polarons*, Physical Review Letters 129, 126401 (2022).
Ref. [142]: S. Falletta, A. Pasquarello, *Polarons free from many-body self-interaction in density functional theory*, Physical Review B 106, 125119 (2022).

4.1 Introduction

Hybrid functionals mixing semilocal density functional and Hartree Fock energies allow one to suppress the many-body self-interaction [19, 40, 60]. Here, we consider the PBE0(α) hybrid functional, in which a fraction α of Fock exchange is admixed to the semilocal exchange. As illustrated in Fig. 4.1, the total energy $E^{\alpha}(q)$ generally shows either a positive or negative concavity with respect to the fractional charge q. For $\alpha = 0$, PBE0(α) reduces to PBE, which is known to have a convex total energy as a function of q. On the other hand, for $\alpha = 1$, the nonlocal exchange operator in PBE0(α) is the same as in Hartree-Fock theory, which is characterized by a concave total energy as a function of q. For a specific value $\alpha = \alpha_{\mathrm{k}}$, PBE0($\alpha_{\mathrm{k}}$) is essentially piecewise linear upon electron occupation. In this case, the many-body self-interaction vanishes. Through Janak's theorem, the energy level of the excess charge obtained with PBE0(α_{k}) is independent of q.

Localized states represent a prototypical case for enforcing the piecewise linearity. For instance, this can be achieved by using either electron probes [64–67], defect states [40, 43, 48, 61, 111, 117, 141–147], or Wannier functions [148]. In this context, piecewise-linear hybrid functionals yield localized polarons [40, 61–63] and band gaps in agreement with state-of-the-art *GW* calculations [40, 60, 64–67]. However, the use of hybrid functionals demands computationally expensive structural and electronic relaxations as compared to semilocal functionals. This is particularly the case in plane-wave codes, but could represent a limiting factor also when using localized-orbital codes, for instance in molecular dynamics simulations.

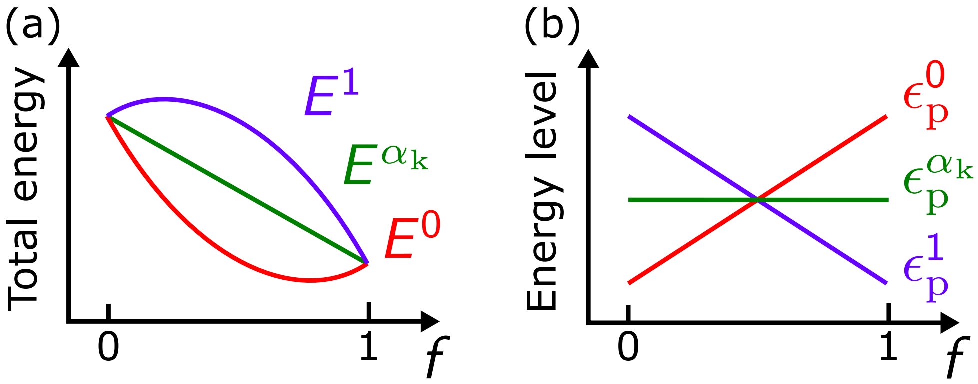

Figure 4.1 – (a) Total energy and (b) energy level of the excess charge as a function of the electron occupation for different PBE0(α) functionals.

4.2 Polaron formation energy

We consider a polaron of charge Q coupled with its self-induced lattice distortions $\mathbf{R}_Q^\alpha$, which are obtained by performing structural relaxation with PBE0(α). For electron polarons $Q = -1$, while for hole polarons $Q = +1$. Then, the PBE0(α) polaron formation energy is defined as [76, 78]

$$E_{\mathrm{f}}^\alpha(Q) = E^\alpha(Q) - E_{\mathrm{ref}}^\alpha(0) + Q\epsilon_{\mathrm{b}}^\alpha, \tag{4.1}$$

where $E^\alpha(Q)$ is the total energy of the polaron system, $E_{\mathrm{ref}}^\alpha(0)$ the total energy of the pristine bulk system, and $\epsilon_{\mathrm{b}}^\alpha$ the band edge corresponding to the delocalized state as calculated for the pristine bulk system. The total energy $E^\alpha(Q)$ is related to the polaron level $\epsilon_{\mathrm{p}}^\alpha(Q)$ through Janak's theorem [75], namely

$$\epsilon_{\mathrm{p}}^\alpha(Q) = -\left.\frac{dE^\alpha(q)}{dq}\right|_{q=Q}, \tag{4.2}$$

where we have introduced the fractional polaron charge q to perform the derivative of the total energy with respect to charge at fixed geometry $\mathbf{R}_Q^\alpha$. The integral version of Eq. (4.2) reads

$$E^\alpha(Q) - E^\alpha(0) = -\int_0^Q dq\, \epsilon_{\mathrm{p}}^\alpha(q). \tag{4.3}$$

The many-body self-interaction vanishes in correspondence of a fraction α_{k} of Fock exchange such that

$$\left.\frac{d}{dq}\epsilon_{\mathrm{p}}^\alpha(q)\right|_{\alpha=\alpha_{\mathrm{k}}} = 0, \tag{4.4}$$

where α_{k} is found self-consistently with the geometry $\mathbf{R}_Q^\alpha$. Then, using Eq. (4.3), one can write

$$E^{\alpha_{\mathrm{k}}}(Q) = E^{\alpha_{\mathrm{k}}}(0) - Q\epsilon_{\mathrm{p}}^{\alpha_{\mathrm{k}}}. \tag{4.5}$$

By inserting Eq. (4.5) in Eq. (4.1) for $\alpha = \alpha_{\mathrm{k}}$, one obtains the following expression for the polaron formation energy

$$E_{\mathrm{f}}^{\alpha_{\mathrm{k}}}(Q) = Q(\epsilon_{\mathrm{b}}^{\alpha_{\mathrm{k}}} - \epsilon_{\mathrm{p}}^{\alpha_{\mathrm{k}}}) + [E^{\alpha_{\mathrm{k}}}(0) - E_{\mathrm{ref}}^{\alpha_{\mathrm{k}}}(0)], \tag{4.6}$$

where the first and the second term on the right hand side correspond to the energetic gain due to the electronic localization and to the energetic cost due to the lattice distortions, respectively. To simplify the notation, the energetics is considered to be corrected by finite-size effects in all formulas. At $\alpha = \alpha_{\mathrm{k}}$, Eqs. (4.1) and (4.2) coincide, and the difference between them can be used to estimate the accuracy by which α_{k} enforces the piecewise linearity condition.

The notion of formation energy is equivalent to the notion of binding energy, with the convention that, for stable polarons, the formation energies are given with a negative sign while the binding energies are given with a positive sign. Experimentally, the polaron binding energy can be measured using photoemission spectroscopy (PES). Photoemission spectroscopy is a well-established method for studying the electronic structure of polarons. Indeed, the energy measured by photoemission can be directly associated with the energy difference between the polaron level and the delocalized band edge. This is due to the fact that the photoemission is faster than the atomic relaxation, and hence the lattice does not relax during the emission. For an electron polaron, this results in the following expression [23]

$$E_{\mathrm{b}} + E_{\mathrm{st}} = h\nu_{\mathrm{p}} - T_e - \Phi, \tag{4.7}$$

where E_{b} is the polaron binding energy, E_{st} is the cost of lattice distortions, $h\nu_{\mathrm{p}}$ is the incident photon energy, T_e is the kinetic energy of the emitted electron, and Φ is the work function of the spectrometer. In our notation, $E_{\mathrm{b}} = -E_{\mathrm{f}}^{\alpha_{\mathrm{k}}}$, and $E_{\mathrm{st}} = [E^{\alpha_{\mathrm{k}}}(0) - E_{\mathrm{ref}}^{\alpha_{\mathrm{k}}}(0)]$. Hence, using Eq. (4.6) in the case of an electron polaron, Eq. (4.7) can be rewritten as

$$\epsilon_{\mathrm{b}}^{\alpha_{\mathrm{k}}} - \epsilon_{\mathrm{p}}^{\alpha_{\mathrm{k}}} = h\nu_{\mathrm{p}} - T_e - \Phi, \tag{4.8}$$

which provides a direct connection between the notion of formation energy and experimental signatures from photoemission spectroscopy.

4.3 Computational details

As case studies, we consider the electron polaron in $\mathrm{BiVO_4}$ [41], the hole polaron in MgO [39], and Al-trapped hole in α-$\mathrm{SiO_2}$ [39, 57, 149–152]. The calculations are performed using a plane-wave density functional approach as implemented in the Quantum Espresso suite [153]. We use the semilocal functional PBE [10] and the hybrid functional PBE0(α) [53]. The core-valence interactions are described by normconserving pseudopotentials [154]. We model $BiVO_4$ with a 96-atom orthorhombic supercell ($a = 10.34$ Å, $b = 10.34$ Å, $c = 11.79$ Å), MgO with a 64-atom cubic supercell ($a = 8.45$ Å), and α-SiO_2 with a 72-atom hexagonal supercell ($a = 9.97$ Å, $c = 10.96$ Å). The lattice parameters and the atomic positions are optimized at the semilocal level of theory for the pristine systems. We sample the Brillouin zone at Γ point. The energy cutoff is set to 100 Ry. The self-trapped polarons ($BiVO_4$, MgO) are obtained by either adding or removing one electron from the system. The Al-trapped polaron in α-SiO_2 is obtained in the neutral system. The polaron structures are obtained through atomic relaxation at fixed supercell parameters.

The high-frequency and static dielectric tensors, $\boldsymbol{\varepsilon}_\infty$ and $\boldsymbol{\varepsilon}_0$, respectively, are determined by applying finite electric fields [87] at the semilocal level of theory. We use the values $e_j = 0, 1 \times 10^{-4}, 2.5 \times 10^{-4}, 5 \times 10^{-4}$ a.u. ($j = x, y, z$) and perform a linear regression to find the components of the dielectric tensors. In the case of isotropic screening (MgO), the electric field is applied only along one Cartesian direction. At variance, in the case of anisotropic screening ($BiVO_4$, α-SiO_2), the electric field is applied along the three Cartesian directions. As an example, we show in Fig. 4.2 the calculation of the zz-component of the high-frequency and static dielectric tensors in $BiVO_4$, MgO, and α-SiO_2. Additionally, as illustrated in Fig. 4.3, the dielectric constants depend quadratically on α, but their variations are minor and can thus be neglected. The obtained values of the dielectric constants are given in Table 4.1.

Table 4.1 – High-frequency and static dielectric constants, ε_∞ and ε_0, respectively, for the systems considered in this thesis, as calculated with the functional PBE.

System	ε_∞	ε_0
$BiVO_4$	5.83	64.95
MgO	2.77	10.73
α-SiO_2	2.25	4.52

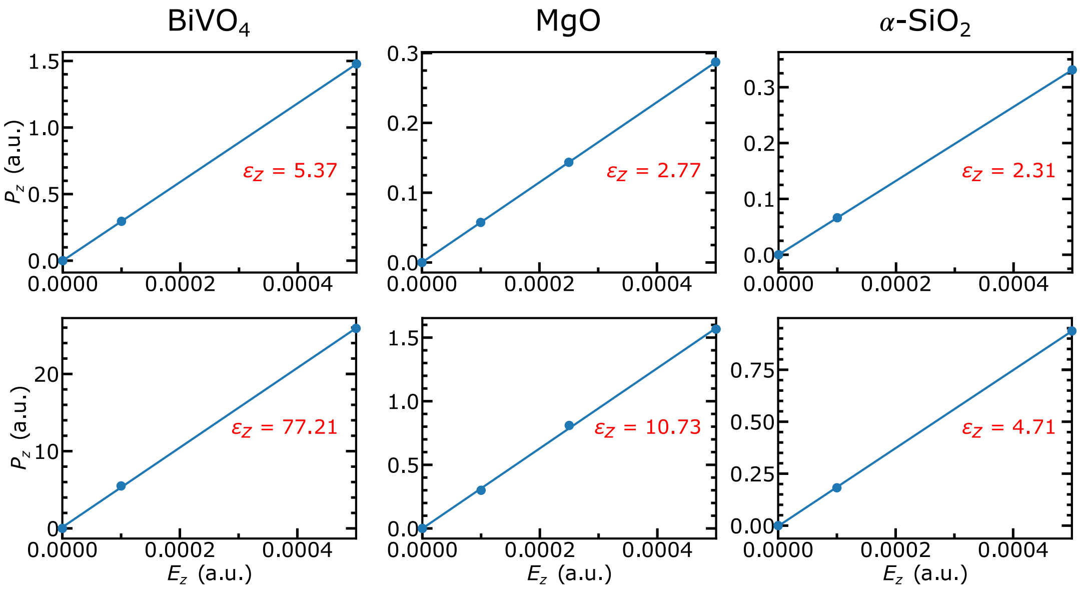

Figure 4.2 – Determination of the component ε_{zz} of the high-frequency and static dielectric constant in BiVO$_4$, MgO, and α-SiO$_2$.

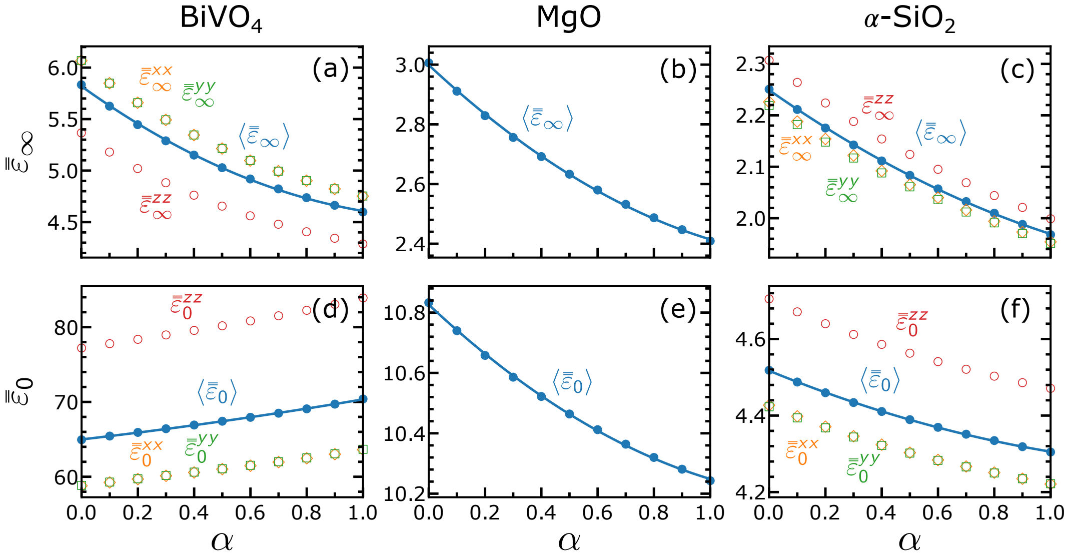

Figure 4.3 – Components ε_{xx}, ε_{yy}, and ε_{zz} of the high-frequency and static dielectric constant as a function of the fraction α of Fock exchange in BiVO$_4$, MgO, and α-SiO$_2$.

4.4 Results

In Fig. 4.4, we show the polaron density obtained with PBE0(α_k) for all cases studied. In BiVO$_4$, the electron polaron localizes on a vanadium atom, thereby causing an elongation of the neighboring V-O bonds from 1.73 to 1.80 Å. In MgO,

Table 4.2 – Finite-size corrections of total energies and polaron levels for the systems with and without polaron charge in the polaron geometry. All values are in eV.

	With polaron		Without polaron	
System	$E_{\rm cor}$	$\epsilon_{\rm cor}$	$E_{\rm cor}$	$\epsilon_{\rm cor}$
$BiVO_4$	0.03	0.06	0.29	-0.58
MgO	0.13	-0.25	0.59	1.34
α-SiO_2	0.00	0.00	1.24	2.47

the hole polaron is centered on an oxygen atom, thereby elongating the neighboring Mg-O bonds from 2.11 to 2.20 Å. In α-SiO_2, the hole is trapped at the Al impurity, with three short Al-O bonds of 1.69 Å and one long Al-O bond of 1.91 Å.

For each system, the fraction $\alpha_{\rm k}$ of Fock exchange used in the polaron calculation is determined according to Eq. (4.4) as follows. We first fix an approximate value of $\alpha_{\rm k}$ and relax the polaron to find the geometry $\mathbf{R}_Q^{\alpha_{\rm k}}$. Second, for this geometry, we obtain the levels $\epsilon_{\rm p}^{\alpha}(0)$ and $\epsilon_{\rm p}^{\alpha}(Q)$ pertaining to the charge states 0 and Q as a function of α. Their intersection gives an improved value for $\alpha_{\rm k}$, with which the procedure is repeated until self-consistency is reached. As illustrated in Figs. 4.5(a-c), we find $\alpha_{\rm k} = 0.14$, 0.34, and 0.45 for $BiVO_4$, MgO, and α-SiO_2, respectively. This study allows us to determine the polaron level $\epsilon_{\rm p}^{\alpha_{\rm k}}$. The finite-size corrections for total energies and polaron levels are given in Table 4.2. In the case of Al-trapped hole in α-SiO_2, the hole trapping occurs in a neutral calculation and is not affected by finite-size effects.

From $\epsilon_{\rm p}^{\alpha_{\rm k}}$, we obtain the formation energies via Eq. (4.6) for all the systems under consideration. For $BiVO_4$, MgO, and α-SiO_2, we find -0.63 eV, -0.53 eV, and -3.11 eV, respectively. In the case of α-SiO_2, the larger formation energy stems from the fact that the hole is not self-trapped but bound to the Al impurity. Furthermore, we illustrate in Figs. 4.5(d-f) the polaron stability as a function of the fraction of Fock exchange α using the formation energy of Eq. (4.1) at fixed geometry $\mathbf{R}_Q^{\alpha_{\rm k}}$. The PBE0($\alpha$) formation energies are found to be very sensitive to α, which is an effect mainly resulting from the strong dependence of the band edge $\epsilon_{\rm b}^{\alpha}$ on α [cf. Figs. 4.5(a-c)]. Moreover, the polaron at $\alpha = 0$ (i.e. PBE) is not stable in all cases. This emphasizes that the functional PBE fails in localizing the polaronic states. In the case of α-SiO_2, we also calculate the formation energy corresponding to the geometry found in PBE, in which the hole is delocalized over

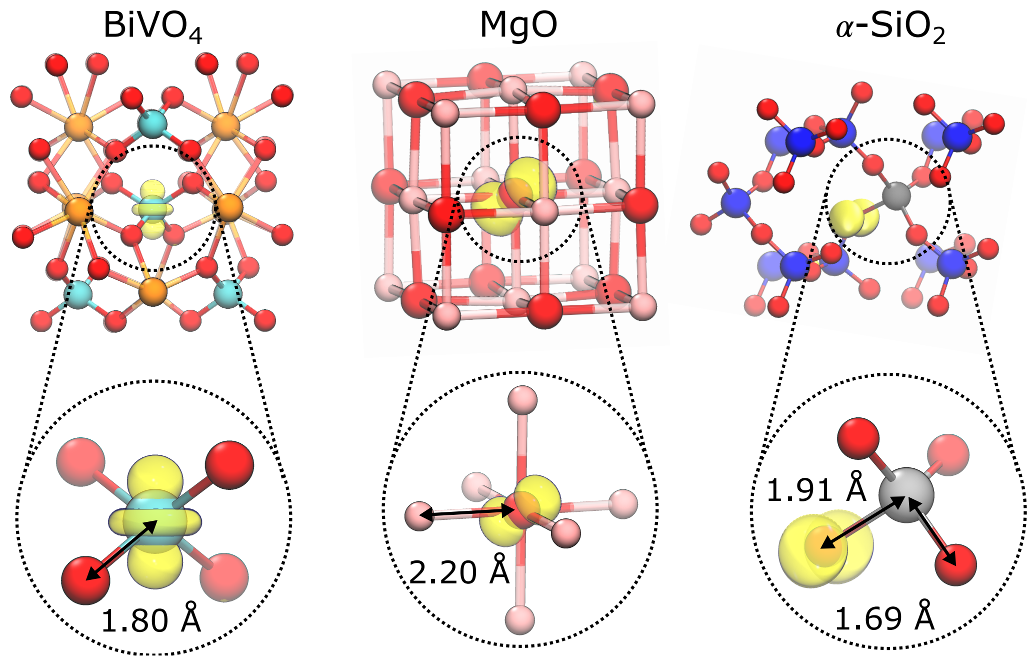

Figure 4.4 – Polaron isodensity surface at 5% of its maximum calculated with PBE0(α_k) for the electron polaron in BiVO$_4$, the hole polaron in MgO, and the Al-trapped hole in α-SiO$_2$ (Bi in orange, V in cyan, O in red, Mg in pink, Si in blue, Al in grey).

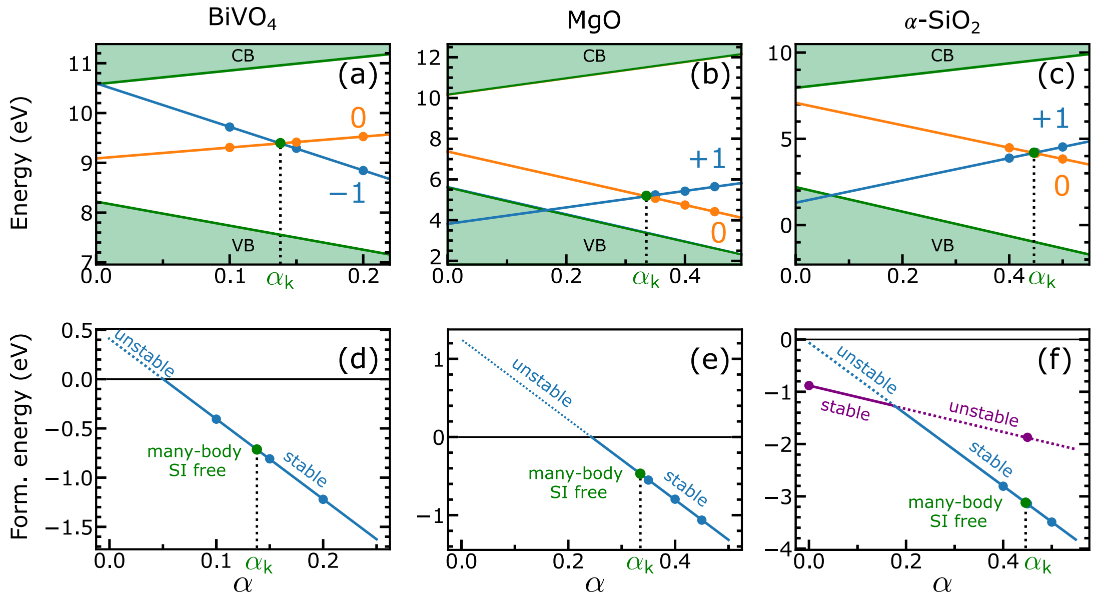

Figure 4.5 – (a-c) Energy levels and (d-f) formation energies obtained with PBE0(α) as a function α for the electron polaron in BiVO$_4$, the hole polaron in MgO, and the Al-trapped hole in α-SiO$_2$. The polaron levels are identified by their respective polaron charge. In all cases, the polaron geometry is obtained with PBE0(α_k).

the four nearest neighbor O atoms (Al-O bond lengths of 1.74 Å). Also in this case, the hole trapped at a single O atom is unstable at $\alpha = 0$, in accord with previous studies [149, 150]. At variance, for $\alpha = \alpha_\mathrm{k}$, the one-site polaron is found to be more stable than the four-site polaron by 1.25 eV.

4.5 Band gaps

To assess the overall quality of the electronic structure, it is of interest to compare the PBE0(α_k) band gaps with experimental values. The comparison with experiment requires the consideration of relevant effects, such as due to spin-orbit coupling, atomic vibrations (zero-point phonon renormalization), electron-hole interaction (for optical band gaps), and magnetic ordering [155–157]. For PBE0(α) functionals, the agreement with experiment is generally rather good when such effects are accounted for [40, 60, 64, 65, 67, 124, 148, 158]. In particular, for $BiVO_4$, MgO, and α-SiO_2, we indeed find errors of at most 0.25 eV when comparing PBE0(α_k) band gaps with relevant experimental values after including suitable corrections (see Table 7.1), consistent with typical values for the mean absolute errors in such comparisons [40, 67].

We remark that the enforcement of the piecewise linearity condition is in principle defect dependent. As investigated in Refs. [40, 64–66], α_k can vary up to ±0.03 de-

Table 4.3 – Band gaps calculated with PBE (E_g^0) and PBE0(α_k) ($E_\mathrm{g}^{\alpha_\mathrm{k}}$) compared to experimental values after including suitable corrections (ΔE_g). Energies are in eV.

System	E_g^0	$E_\mathrm{g}^{\alpha_\mathrm{k}}$	ΔE_g	$E_\mathrm{g}^{\alpha_\mathrm{k}} + \Delta E_\mathrm{g}$	Expt.
$BiVO_4$	2.38	3.41	-1.16^I	2.25	2.4-2.5 $^\mathrm{II}$
MgO	4.65	8.15	-0.53^III	7.62	7.77 $^\mathrm{IV}$
α-SiO_2	5.81	10.51	0.02^V	10.53	10.30 $^\mathrm{VI}$

[I] Ref. [155], including spin-orbit coupling, thermal vibrations, and exciton binding energy.
[II] Refs. [159–161], optical band gap at 300 K.
[III] Ref. [162], zero-point phonon renormalization.
[IV] Ref. [163], fundamental band gap at 6 K.
[V] Separation of 0.60 eV between fundamental band gap and first absorption peak [164], and zero-point phonon renormalization of −0.58 eV [165].
[VI] Ref. [166], first peak in reflectance spectrum.

pending on the defect under consideration. However, by selecting an optimal defect ensuring minimal hybridization with the delocalized band states, the uncertainty in α_{k} can be further reduced [65]. Accurate comparisons with experimental band gaps in Refs. [65, 67] show agreement within 0.25 eV. The dependence of α_{k} on the defect considered ultimately reflects the approximate nature of the PBE0(α) functional.

4.6 Discussion

We showed that implementing a constraint like the piecewise linearity from exact density functional theory in approximate functionals results in a successful description of the many-body self-interaction. Following the same lines, one could also specifically focus on including the long-range $-1/(\varepsilon_\infty r)$ dependence of the Coulomb potential [158], which is another property of the exact density functional [19]. In PBE0(α) functionals, these properties correspond to setting the fraction of Fock exchange to α_{k} and $\alpha_{\mathrm{lr}} = 1/\varepsilon_\infty$, respectively. For most materials, the values of α_{k} and α_{lr} are generally quite close, leading to similar band gaps [40, 64]. When α_{k} and α_{lr} differ noticeably, it is still possible to include both conditions coming from exact density functional theory through the consideration of more involved functionals, such as range-separated hybrid functionals [40, 66, 158, 167].

The class of PBE0(α) hybrid functionals is particularly relevant since it can cover straightforwardly either the one-body or the many-body self-interaction. In particular, for $\alpha = 1$ the one-body self-interaction is removed as in Hartree-Fock theory and band gaps are largely overestimated. At variance, for $\alpha = \alpha_{\mathrm{k}}$ the many-body self-interaction vanishes, leading to accurate polaron formation energies and band gaps.

5 Unified formulation for the self-interaction

We develop a unified theoretical framework encompassing one-body and many-body forms of self-interaction. We find an analytic expression for both the one-body and the many-body self-interaction energies, and quantitatively connect the two expressions through the dielectric constant. This demonstrates that the many-body notion of self-interaction accounts for additional electron screening effects, which are missing in the one-body notion of self-interaction. Moreover, the two forms of self-interaction are found to coincide in the absence of electron screening. This analysis allows us to confer superiority to the notion of many-body self-interaction over the notion of one-body self-interaction.

This chapter is adapted from:
Ref. [141]: S. Falletta, A. Pasquarello, *Many-body self-interaction and polarons*, Physical Review Letters 129, 126401 (2022).
Ref. [142]: S. Falletta, A. Pasquarello, *Polarons free from many-body self-interaction in density functional theory*, Physical Review B 106, 125119 (2022).

5.1 Introduction

In the previous Chapter, we studied polarons free from many-body self-interaction using hybrid functionals. We emphasized that piecewise-linear hybrid functionals lead to an overall improvement of the electronic structure, including band gaps. At variance, suppressing the one-body self-interaction leads to an overestimation of polaron formation energies and band gaps (cf. Fig. 4.5), thus suggesting that one should correct for the many-body self-interaction rather than for the one-body self-interaction. In this context, the family of hybrid functionals PBE0(α) allows one to investigate the notions of one-body and many-body self-interaction in a comparative fashion.

Here, we develop a unified formulation for both forms of self-interaction within the family of hybrid functionals PBE0(α). This can be used to quantify the connection between these two forms of self-interaction and thereby to determine which form of self-interaction should be addressed when modelling polarons. In the following, we start by presenting the assumptions of our formulation.

5.2 Assumptions

We consider a localized polaron with the atomic structure $\mathbf{R}_Q^{\alpha_\mathrm{k}}$ as obtained with the piecewise-linear PBE0(α_k) functional. The single-particle levels are known to depend linearly on α in PBE0(α) calculations [40, 43, 48, 60, 64, 65]. Furthermore, the total energy $E^\alpha(q)$ obtained with PBE0(α) generally shows a quadratic behavior upon addition of a fractional polaron charge q [20, 168]. Hence, through Janak's theorem [75] [cf. Eq. (4.2)], the polaron level $\epsilon_\mathrm{p}^\alpha(q)$ can be taken to depend linearly on both q and α. This assumption has implications on the wave functions $\psi_{i\sigma}^\alpha$. We denote ψ_p^α the polaron wave function, and $n_\mathrm{p}^\alpha = |\psi_\mathrm{p}^\alpha|^2$ the polaron density. The electron (hole) polaron state is identified as the last-occupied (first unoccupied) state in the spin channel σ_p. The density of valence electrons can be then expressed as

$$n_{\sigma\mathrm{val}}^\alpha(q) = n_\sigma^\alpha(q) + \delta_{\sigma,\sigma_\mathrm{p}} q n_\mathrm{p}^\alpha, \tag{5.1}$$

where δ is the Kronecker delta, and n_σ^α is the total density in the spin channel σ.

We first focus on the assumption of linearity of $\epsilon_\mathrm{p}^\alpha(q)$ with respect to q. Then, the first derivative of $\epsilon_\mathrm{p}^\alpha(q)$ with respect to q must be a constant. For simplicity, we consider the case $\alpha = 0$. Using the Hellmann-Feynman theorem and the chain rule for the derivatives with respect to q, we get

$$\frac{d\epsilon_\mathrm{p}^0(q)}{dq} = \langle\psi_\mathrm{p}^0|\frac{d\mathcal{H}_{\sigma_\mathrm{p}}^0}{dq}|\psi_\mathrm{p}^0\rangle = \sum_\sigma \int d\mathbf{r}d\mathbf{r}' \, \frac{\delta\mathcal{H}_{\sigma_\mathrm{p}}^0[n_\uparrow^0, n_\downarrow^0](\mathbf{r})}{\delta n_\sigma^0(\mathbf{r}')} \frac{dn_\sigma^0(\mathbf{r}')}{dq} n_\mathrm{p}^0(\mathbf{r}). \tag{5.2}$$

We note that the derivative dn_σ^0/dq can be split into contributions pertaining to the polaron and to the valence electrons. Using the definition of the density of valence electrons in Eq. (5.1), we can write

$$\frac{dn_\sigma^0}{dq} = \frac{dn_{\sigma\mathrm{val}}^0}{dq} - \delta_{\sigma,\sigma_\mathrm{p}}\left(n_\mathrm{p}^0 + q\frac{dn_\mathrm{p}^0}{dq}\right). \tag{5.3}$$

By inserting Eq. (5.3) in Eq. (5.2), one infers that $d\epsilon_\mathrm{p}^0(q)/dq$ is constant with q when neglecting the variations of the polaron density with q and the second-order derivative of the valence electron density with respect to q, i.e.

$$\frac{dn_\mathrm{p}^0}{dq} = 0 \qquad \text{and} \qquad \frac{d^2 n_{\sigma\mathrm{val}}^0}{dq^2} = 0. \tag{5.4}$$

Such conditions also apply to the respective wave functions and can be extended to the case $\alpha \neq 0$.

Next, we consider the assumption of linearity of $\epsilon_\mathrm{p}^\alpha(q)$ in α. Then, the first derivative of $\epsilon_\mathrm{p}^\alpha(q)$ with respect to α must be a constant. Using the Hellmann-Feynman theorem and expliciting the α-dependency of the Hamiltonian $\mathcal{H}_{\sigma_\mathrm{p}}^\alpha$, one has

$$\begin{aligned}\frac{d\epsilon_\mathrm{p}^\alpha(q)}{d\alpha} &= \langle\psi_\mathrm{p}^\alpha|\frac{d\mathcal{H}_{\sigma_\mathrm{p}}^\alpha}{d\alpha}|\psi_\mathrm{p}^\alpha\rangle = \langle\psi_\mathrm{p}^\alpha|\frac{d}{d\alpha}\left(\mathcal{H}_{\sigma_\mathrm{p}}^0 + \alpha\frac{\partial\mathcal{H}_{\sigma_\mathrm{p}}^\alpha}{\partial\alpha}\right)|\psi_\mathrm{p}^\alpha\rangle \\ &= \langle\psi_\mathrm{p}^\alpha|\left(\frac{d\mathcal{H}_{\sigma_\mathrm{p}}^0}{d\alpha} + \frac{\partial\mathcal{H}_{\sigma_\mathrm{p}}^\alpha}{\partial\alpha} + \alpha\frac{d}{d\alpha}\frac{\partial\mathcal{H}_{\sigma_\mathrm{p}}^\alpha}{\partial\alpha}\right)|\psi_\mathrm{p}^\alpha\rangle\,. \end{aligned} \tag{5.5}$$

Then, neglecting the explicit α-dependent term in Eq. (5.5), one obtains

$$\frac{d\epsilon_\mathrm{p}^\alpha(q)}{d\alpha} = \langle\psi_\mathrm{p}^\alpha|\left(\frac{d\mathcal{H}_{\sigma_\mathrm{p}}^0}{d\alpha} + \frac{\partial\mathcal{H}_{\sigma_\mathrm{p}}^\alpha}{\partial\alpha}\right)|\psi_\mathrm{p}^\alpha\rangle\,. \tag{5.6}$$

The first term in the right-hand side of Eq. (5.6) can be expressed using the chain rule, namely

$$\frac{d\mathcal{H}^0_{\sigma_\mathrm{p}}}{d\alpha} = \sum_\sigma \int d\mathbf{r}\, \frac{\delta\mathcal{H}^0_{\sigma_\mathrm{p}}[n^\alpha_\uparrow, n^\alpha_\downarrow]}{\delta n^\alpha_\sigma(\mathbf{r})} \frac{dn^\alpha_\sigma(\mathbf{r})}{dq}. \tag{5.7}$$

The second term in the right-hand side of Eq. (5.6) is easily reformulated using Eq. (2.7) as

$$\frac{\partial\mathcal{H}^\alpha_{\sigma_\mathrm{p}}}{\partial\alpha} = -V_{\mathrm{x}\sigma_\mathrm{p}}[n^\alpha_\uparrow, n^\alpha_\downarrow] + V_\mathrm{X}[\{\psi^\alpha_{i\sigma_\mathrm{p}}\}]. \tag{5.8}$$

Thus, Eq. (5.6) depends on α only through the wave functions $\psi^\alpha_{i\sigma}$. Therefore, the assumption of constant $d\epsilon^\alpha_\mathrm{p}(q)/d\alpha$ with α implies neglecting the variations of the wave functions with α, i.e.

$$\frac{d\psi^\alpha_{i\sigma}}{d\alpha} = 0. \tag{5.9}$$

Hence, in our formulation, the variations of the polaron wave function with q, the second-order derivative of the wave functions of the valence states with respect to q, and the variations of the wave functions with α can be taken to vanish.

We then expand $\epsilon^\alpha_\mathrm{p}(q)$ in α around α_k,

$$\epsilon^\alpha_\mathrm{p}(q) = \epsilon^{\alpha_\mathrm{k}}_\mathrm{p} + (\alpha - \alpha_\mathrm{k})\frac{d\epsilon^\alpha_\mathrm{p}(q)}{d\alpha}, \tag{5.10}$$

where $\epsilon^{\alpha_\mathrm{k}}_\mathrm{p}$ is independent of q because of the definition of α_k [cf. Eq. (4.4)]. By further expanding the right-hand side of Eq. (5.10) with respect to q around $q = 0$, we get

$$\epsilon^\alpha_\mathrm{p}(q) = \epsilon^{\alpha_\mathrm{k}}_\mathrm{p} + (\alpha - \alpha_\mathrm{k})\left[\frac{d\epsilon^\alpha_\mathrm{p}(0)}{d\alpha} + q\frac{d^2\epsilon^\alpha_\mathrm{p}(q)}{d\alpha dq}\right]. \tag{5.11}$$

By introducing the fractional charge q_k defined as

$$q_\mathrm{k} = -\frac{d\epsilon^\alpha_\mathrm{p}(0)}{d\alpha}\bigg/\frac{d^2\epsilon^\alpha_\mathrm{p}(q)}{d\alpha dq}, \tag{5.12}$$

we can rewrite Eq. (5.11) as

$$\epsilon_{\mathrm{p}}^{\alpha}(q) = \epsilon_{\mathrm{p}}^{\alpha_{\mathrm{k}}} + (\alpha - \alpha_{\mathrm{k}})(q - q_{\mathrm{k}})\frac{d^2\epsilon_{\mathrm{p}}^{\alpha}(q)}{d\alpha dq}. \tag{5.13}$$

The result in Eq. (5.13) can be equivalently obtained by first expanding $\epsilon_{\mathrm{p}}^{\alpha}(q)$ in q around q_{k} and then by expanding in α around α_{k}. In this case, we get the following expression for α_{k}

$$\alpha_{\mathrm{k}} = -\frac{d\epsilon_{\mathrm{p}}^{0}(q)}{dq} \Bigg/ \frac{d^2\epsilon_{\mathrm{p}}^{\alpha}(q)}{d\alpha dq}, \tag{5.14}$$

which is analogous to Eq. (5.12). By taking the ratio between the expressions in Eqs. (5.12) and (5.14), we find a relationship that links α_{k} and q_{k}:

$$\frac{q_{\mathrm{k}}}{\alpha_{\mathrm{k}}} = \frac{d\epsilon_{\mathrm{p}}^{\alpha}(0)}{d\alpha} \Bigg/ \frac{d\epsilon_{\mathrm{p}}^{0}(q)}{dq}, \tag{5.15}$$

which emphasizes the duality between α_{k} and q_{k} in the expression of $\epsilon_{\mathrm{p}}^{\alpha}(q)$ [cf. Eq. (5.13)]. In particular, as α_{k} represents the fraction of Fock exchange for which the polaron level is free from many-body self-interaction at any fractional charge q, q_{k} is the fractional charge for which the polaron level is free from many-body self-interaction at any fraction of Fock exchange α. This will be instrumental in the following derivations.

5.3 Many-body self-interaction

We define the many-body self-interaction energy correction to the PBE0(α) energy as

$$\Delta E^{\alpha}(q)|_{\mathrm{mb}} = [E^{\alpha}(0) - q\epsilon_{\mathrm{p}}^{\alpha_{\mathrm{k}}}] - E^{\alpha}(q), \tag{5.16}$$

such that the energy $E^{\alpha}(q) + \Delta E^{\alpha}(q)|_{\mathrm{mb}}$ is piecewise linear as a function of q. At $\alpha = \alpha_{\mathrm{k}}$, $\Delta E^{\alpha_{\mathrm{k}}}|_{\mathrm{mb}}$ vanishes by definition of α_{k}. The total energy $E^{\alpha}(q)$ in Eq. (5.16) can be expanded at second order in q as

$$E^{\alpha}(q) - E^{\alpha}(0) = -q\epsilon_{\mathrm{p}}^{\alpha}(0) - \frac{q^2}{2}\frac{d\epsilon_{\mathrm{p}}^{\alpha}(q)}{dq}, \tag{5.17}$$

where we have applied Janak's theorem for expressing the first and the second derivative of the total energy with respect to q in terms of the polaron level. By inserting Eq. (5.17) in Eq. (5.16) and by expressing $\epsilon_{\mathrm{p}}^{\alpha_{\mathrm{k}}} = \epsilon_{\mathrm{p}}^{\alpha}(q_{\mathrm{k}})$, we get

$$\Delta E^{\alpha}(q)|_{\mathrm{mb}} = q[\epsilon_{\mathrm{p}}^{\alpha}(0) - \epsilon_{\mathrm{p}}^{\alpha}(q_{\mathrm{k}})] + \frac{q^2}{2}\frac{d\epsilon_{\mathrm{p}}^{\alpha}(q)}{dq}. \tag{5.18}$$

By using the linearity of the polaron level in q, the latter equation becomes

$$\Delta E^{\alpha}(q)|_{\mathrm{mb}} = \frac{1}{2}\Big[(q - q_{\mathrm{k}})^2 - q_{\mathrm{k}}^2\Big]\frac{d\epsilon_{\mathrm{p}}^{\alpha}(q)}{dq}. \tag{5.19}$$

Expanding $\epsilon_{\mathrm{p}}^{\alpha}(q)$ in α and using the definition of α_{k} in Eq. (5.14), we obtain

$$\frac{d\epsilon_{\mathrm{p}}^{\alpha}(q)}{dq} = \Big(1 - \frac{\alpha}{\alpha_{\mathrm{k}}}\Big)\frac{d\epsilon_{\mathrm{p}}^{0}(q)}{dq} = -\Big(1 - \frac{\alpha}{\alpha_{\mathrm{k}}}\Big)\frac{d^2E^0(q)}{dq^2}, \tag{5.20}$$

where the second equality stems from Janak's theorem. This allows us to express Eq. (5.19) as

$$\Delta E^{\alpha}(q)|_{\mathrm{mb}} = -\frac{1}{2}\Big(1 - \frac{\alpha}{\alpha_{\mathrm{k}}}\Big)\Big[(q - q_{\mathrm{k}})^2 - q_{\mathrm{k}}^2\Big]\frac{d^2E^0(q)}{dq^2}. \tag{5.21}$$

Using the chain rule on the second derivative of the total energy with respect to q, we get

$$\begin{aligned}\Delta E^{\alpha}(q)|_{\mathrm{mb}} = -\Big(1 - \frac{\alpha}{\alpha_{\mathrm{k}}}\Big)\Big[(q - q_{\mathrm{k}})^2 - q_{\mathrm{k}}^2\Big]\Bigg\{ & E_{\mathrm{H}}\Big[\frac{dn}{dq}\Big] \\ & + \frac{1}{2}\sum_{\sigma\sigma'}\int d\mathbf{r}d\mathbf{r}'\,\frac{\delta^2E_{\mathrm{xc}}[n_\uparrow, n_\downarrow]}{\delta n_\sigma(\mathbf{r})\delta n_{\sigma'}(\mathbf{r}')}\frac{dn_\sigma(\mathbf{r})}{dq}\frac{dn_{\sigma'}(\mathbf{r})}{dq}\Bigg\},\end{aligned} \tag{5.22}$$

where the second derivatives of n_σ with respect to q have been taken to vanish and the superscript 0 in the densities n_σ has been skipped, consistently with the assumptions of our formulation. In Eq. (5.22), the Fock exchange effects are entirely described by q_{k} and α_{k}. Apart from the parameters q_{k} and α_{k}, $\Delta E^{\alpha}(q)|_{\mathrm{mb}}$ is herewith expressed in terms of a quantity that can be evaluated at the semilocal PBE level. By applying Janak's theorem to $\Delta E^{\alpha}(q)|_{\mathrm{mb}}$ in Eq. (5.21), we find the many-body self-interaction correction to the polaron level

$$\Delta\epsilon_{\mathrm{p}}^{\alpha}(q)\big|_{\mathrm{mb}} = -\frac{d}{dq}\,\Delta E^{\alpha}(q)|_{\mathrm{mb}} = -\Big(1 - \frac{\alpha}{\alpha_{\mathrm{k}}}\Big)(q - q_{\mathrm{k}})\frac{d\epsilon_{\mathrm{p}}^{0}(q)}{dq}, \tag{5.23}$$

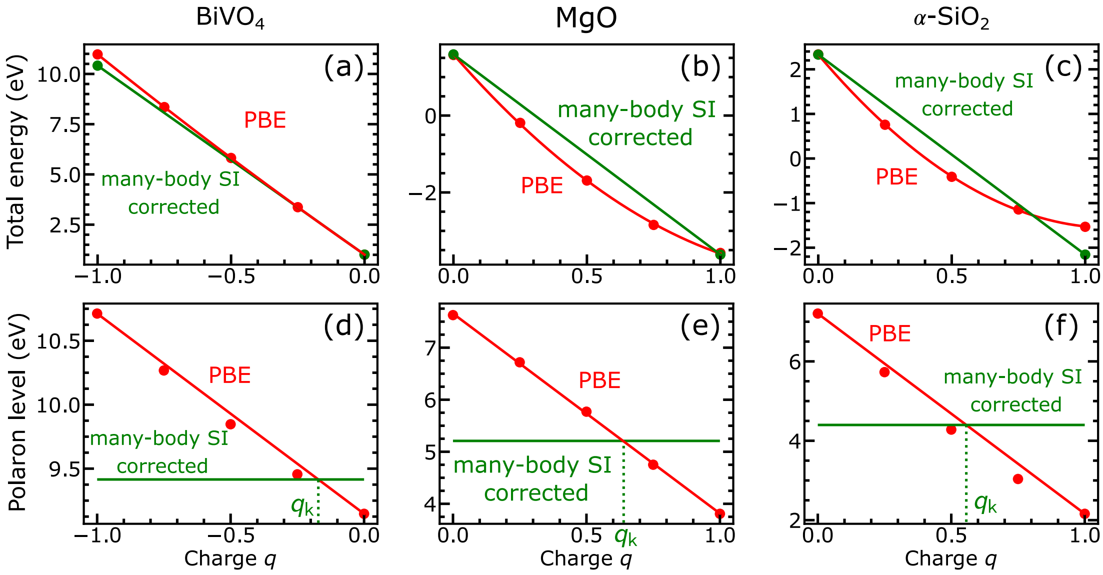

Figure 5.1 – Many-body self-interaction corrected (a-c) total energy $E^0(q)$ and (d-f) polaron level $\epsilon_\mathrm{p}^0(q)$ as a function of the charge q, for the electron polaron in BiVO$_4$, the hole polaron in MgO, and the trapped hole at the Al impurity in α-SiO$_2$. The localized polarons are obtained with the hybrid functional PBE0(α_k).

which vanishes at both $\alpha = \alpha_\mathrm{k}$ or $q = q_\mathrm{k}$, consistently with Eq. (5.13). Thus, the polaron level $\epsilon_\mathrm{p}^\alpha + \Delta\epsilon_\mathrm{p}^\alpha\big|_\mathrm{mb}$ is constant for varying polaron charge q. Applying the Hellmann-Feynman theorem to the derivative of $\epsilon_\mathrm{p}^0(q)$ with respect to q, we get

$$\frac{d\epsilon_\mathrm{p}^0(q)}{dq} = \langle\psi_\mathrm{p}|\frac{d\mathcal{H}_{\sigma_\mathrm{p}}^0(q)}{dq}|\psi_\mathrm{p}\rangle\,. \tag{5.24}$$

Then, using the chain rule on the derivative of the Hamiltonian $\mathcal{H}_{\sigma_\mathrm{p}}^0(q)$ with respect to q, Eq. (5.23) can be rewritten as

$$\Delta\epsilon_\mathrm{p}^\alpha(q)\big|_\mathrm{mb} = -\Big(1-\frac{\alpha}{\alpha_\mathrm{k}}\Big)(q-q_\mathrm{k})\int d\mathbf{r}\,\Bigg\{V_\mathrm{H}\left[\frac{dn}{dq}\right](\mathbf{r}) + \sum_\sigma\int d\mathbf{r}'\,\frac{\delta V_{\mathrm{xc}\sigma_\mathrm{p}}[n_\uparrow,n_\downarrow](\mathbf{r})}{\delta n_\sigma(\mathbf{r}')}\frac{dn_\sigma(\mathbf{r}')}{dq}\Bigg\}n_\mathrm{p}(\mathbf{r}). \tag{5.25}$$

We evaluate the many-body self-interaction corrected total energy and polaron level as a function of q for the cases studied. Here, we determine the polaron energetics at $\alpha = 0$ (PBE) at first-order perturbation theory using the wave functions and the atomic structure obtained with the hybrid functional PBE0(α_k). The many-

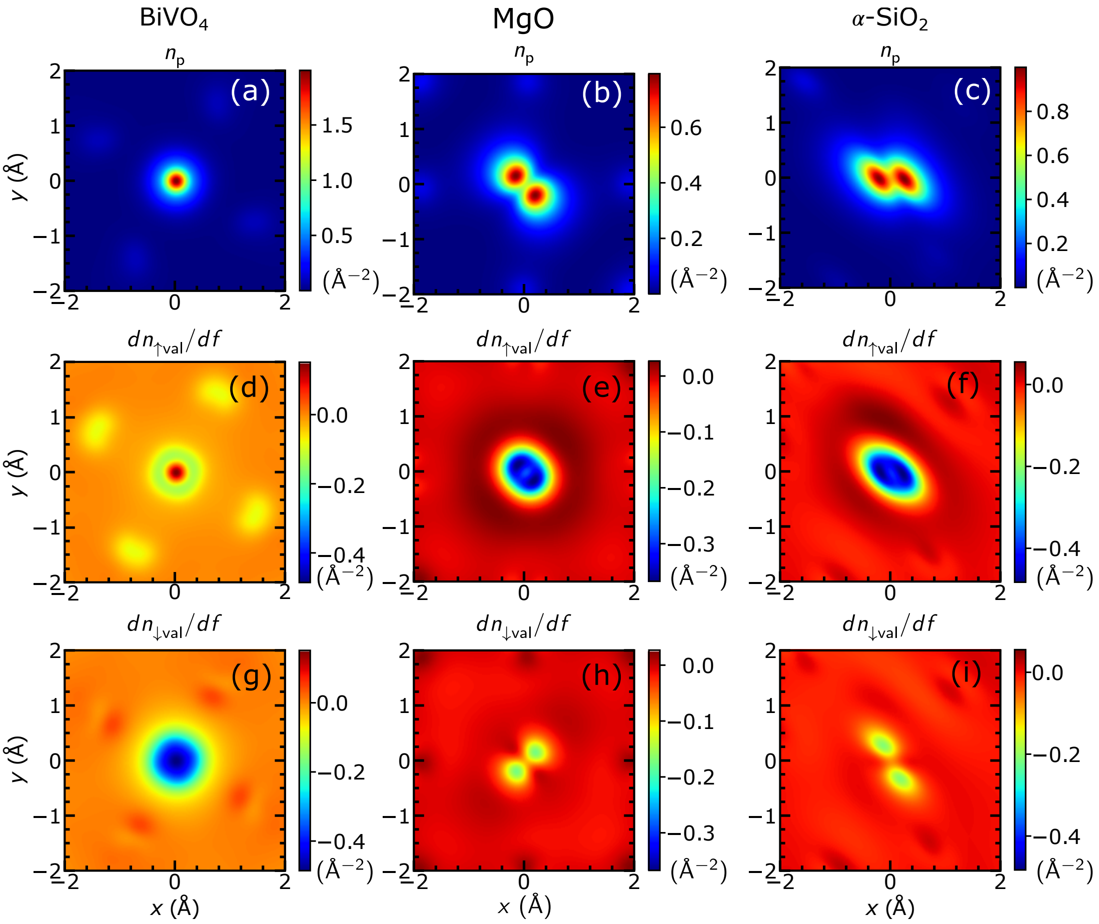

Figure 5.2 – (a-c) Polaron density n_{p} and (d-i) variation of the valence-electron densities $n_{\sigma\mathrm{val}}$ upon the occupation f of the polaron level (cf. Eq. (5.27)) for the electron polaron in BiVO$_4$, and the hole polaron in α-SiO$_2$, as obtained with the functional PBE0(α_{k}). The densities are integrated over the z direction and plotted in the xy plane. The results for the hole polaron in MgO are shown in Ref. [141].

body self-interaction corrections are evaluated using the following finite-difference expression for $d\epsilon_{\mathrm{p}}^0(q)/dq$

$$\frac{d\epsilon_{\mathrm{p}}^0(q)}{dq} = \frac{\epsilon_{\mathrm{p}}^0(Q) - \epsilon_{\mathrm{p}}^0(0)}{Q}, \tag{5.26}$$

where the levels $\epsilon_{\mathrm{p}}^0(Q)$ and $\epsilon_{\mathrm{p}}^0(0)$ are calculated with the semilocal functional PBE. As illustrated in Figs. 5.1(a-b) in the cases of BiVO$_4$ and α-SiO$_2$, the PBE total energy exhibits a concavity upon partial electron occupation, and a corresponding linear variation of the polaron level [cf. Figs. 5.1(c-d)]. Upon applying the corrections $\Delta E^0(q)|_{\mathrm{mb}}$ and $\Delta\epsilon_{\mathrm{p}}^0(q)\big|_{\mathrm{mb}}$, the total energy and the polaron level become linear and constant in q, respectively.

The electron screening affects the many-body self-interaction corrections in Eqs. (5.22) and (5.25) through the derivatives dn_σ/dq. To illustrate such screening effects, it is convenient to focus on the density of valence electrons [cf. Eq. (5.1)]. Then, the variations of $n_{\sigma\text{val}}(q)$ with respect to q can be calculated by finite differences as

$$\frac{dn_{\sigma\text{val}}(q)}{dq} = \frac{n_\sigma(Q) + \delta_{\sigma,\sigma_\text{p}} Q n_\text{p} - n_\sigma(0)}{Q}. \tag{5.27}$$

These variations are shown in Fig. 5.2 for both spin channels in the cases of the electron polaron in BiVO_4 and the Al-trapped hole in α-SiO_2. First, we remark that the response of the valence electrons with respect to the polaron charge is not negligible compared to the polaron charge density. Second, the screening effects in the two spin channels are noticeably different. This emphasizes the limitation of using the restricted open-shell Kohn-Sham constraint in the self-consistent optimization of the Kohn-Sham equations.

5.4 One-body self-interaction

We define the one-body self-interaction energy correction to $E^\alpha(q)$ as

$$\Delta E^\alpha(q)|_\text{ob} = [E^1(q) - E^1(0)] - [E^\alpha(q) - E^\alpha(0)], \tag{5.28}$$

which reproduces the q dependence of the energy found for the Hartree-Fock like regime at $\alpha = 1$. The correction $\Delta E^\alpha(q)|_\text{ob}$ vanishes for $\alpha = 1$. Given the linearity of the total energy with respect to α, Eq. (5.28) can be rewritten as

$$\Delta E^\alpha(q)|_\text{ob} = (1-\alpha)\frac{d}{d\alpha}[E^\alpha(q) - E^\alpha(0)]. \tag{5.29}$$

Using the total energy expansion in Eq. (5.17), the definitions of q_k and α_k in Eqs. (5.12) and (5.14), and Janak's theorem in Eq. (4.2), we find

$$\Delta E^\alpha(q)|_\text{ob} = -\frac{1}{2}\frac{(1-\alpha)}{\alpha_\text{k}}\left[(q-q_\text{k})^2 - q_\text{k}^2\right]\frac{d^2E^0(q)}{dq^2}. \tag{5.30}$$

Using Janak's theorem, the one-body energy correction to the polaron level is obtained as

$$\Delta\epsilon_{\mathrm{p}}^{\alpha}(q)\big|_{\mathrm{ob}} = -\frac{d}{dq}\,\Delta E^{\alpha}(q)|_{\mathrm{ob}} = -(q-q_{\mathrm{k}})\frac{(1-\alpha)}{\alpha_{\mathrm{k}}}\frac{d\epsilon_{\mathrm{p}}^{0}(q)}{dq}, \tag{5.31}$$

which corresponds to the energy difference $\epsilon_{\mathrm{p}}^{1}(q) - \epsilon_{\mathrm{p}}^{\alpha}(q)$.

5.5 Relationship between many-body and one-body self-interaction

Interestingly, the one-body self-interaction energy corrections can be derived starting from the many-body self-interaction energy corrections. For the total energy, one has

$$\Delta E^{\alpha}(q)|_{\mathrm{ob}} = \Delta E^{\alpha}(q)|_{\mathrm{mb}} - \Delta E^{1}(q)\big|_{\mathrm{mb}}\,. \tag{5.32}$$

Similarly, for the polaron level,

$$\Delta\epsilon_{\mathrm{p}}^{\alpha}(q)\big|_{\mathrm{ob}} = \Delta\epsilon_{\mathrm{p}}^{\alpha}(q)\big|_{\mathrm{mb}} - \Delta\epsilon_{\mathrm{p}}^{1}(q)\big|_{\mathrm{mb}}\,. \tag{5.33}$$

This relation is illustrated in Fig. 5.3 in the case of a hole polaron.

The relationship between the two forms of self-interaction can be further highlighted

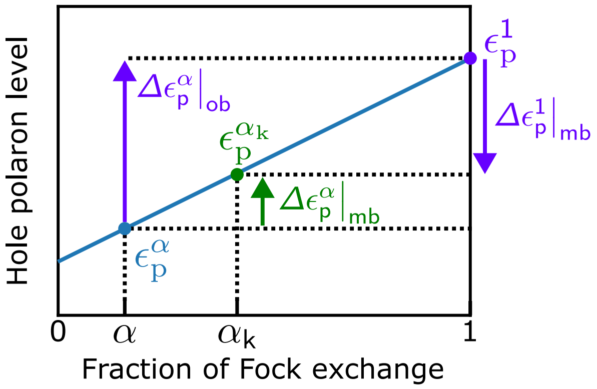
Hole polaron level
$\epsilon_{\mathrm{p}}^{1}$
$\Delta\epsilon_{\mathrm{p}}^{\alpha}|_{\mathrm{ob}}$
$\Delta\epsilon_{\mathrm{p}}^{1}|_{\mathrm{mb}}$
$\epsilon_{\mathrm{p}}^{\alpha_{\mathrm{k}}}$
$\Delta\epsilon_{\mathrm{p}}^{\alpha}|_{\mathrm{mb}}$
$\epsilon_{\mathrm{p}}^{\alpha}$
0
α
α_{k}
1
Fraction of Fock exchange

Figure 5.3 – One-body and many-body self-interaction energy corrections for a hole polaron level $\epsilon_{\mathrm{p}}^{\alpha}(Q=+1)$, illustrating Eq. (5.33).

by taking the ratio between $\Delta E^{\alpha}(q)|_{\text{mb}}$ and $\Delta E^{\alpha}(q)|_{\text{ob}}$ in Eqs. (5.21) and (5.30):

$$\Delta E^{\alpha}(q)|_{\text{mb}} = \frac{\alpha_{\text{k}} - \alpha}{1-\alpha}\, \Delta E^{\alpha}(q)|_{\text{ob}}\,, \tag{5.34}$$

which reveals that these two forms of self-interaction are related by a proportionality relation. For $\alpha = 0$ (PBE), Eq. (5.34) takes the simple form

$$\Delta E^{0}(q)\big|_{\text{mb}} = \alpha_{\text{k}}\, \Delta E^{0}(q)\big|_{\text{ob}}\,. \tag{5.35}$$

The parameter α_{k} is generally related to electron screening, as represented by the high-frequency dielectric constant ε_∞ [169, 170]. In particular, $\alpha_{\text{k}} \simeq 1/\varepsilon_\infty$ reproduces the correct asymptotic potential in the long-range limit [19, 167] and generally yields band gaps in good agreement with state-of-the-art *GW* calculations [40, 171, 172]. Hence, Eq. (5.35) can be rewritten as

$$\Delta E^{0}(q)\big|_{\text{mb}} \simeq \frac{1}{\varepsilon_\infty}\, \Delta E^{0}(q)\big|_{\text{ob}}\,, \tag{5.36}$$

which establishes a quantitative relationship between these self-interaction energies in case of $\alpha = 0$. Equation (5.36) carries similarity with the Hartree-Fock theory of excitons [173, 174]. Indeed, when calculating the exciton binding energy, the bare Coulomb kernel $1/|\mathbf{r}-\mathbf{r}'|$ is replaced with the screened kernel $1/(\epsilon_\infty|\mathbf{r}-\mathbf{r}'|)$, which includes the dielectric constant analogously to Eq. (5.36). Hence, the account of screening effects in the many-body self-interaction emphasizes its superiority over the one-body self-interaction.

The connection between many-body and one-body forms of self-interaction can be further highlighted by turning off the electron screening. This can be achieved by setting equal to zero the variations of the wave functions with respect to q. Starting from Eq. (5.1), this gives

$$\left.\frac{dn_\sigma}{dq}\right|_{\text{bare}} = -\delta_{\sigma,\sigma_{\text{p}}} n_{\text{p}}. \tag{5.37}$$

In this limit, we apply the Hellmann-Feynmann theorem to $d\epsilon_{\text{p}}^{\alpha}(q)/dq$ and obtain

$$\left.\frac{d\epsilon_{\text{p}}^{\alpha}(q)}{dq}\right|_{\text{bare}} = \langle\psi_{\text{p}}|\left.\frac{d\mathcal{H}_{\sigma_{\text{p}}}^{\alpha}(q)}{dq}\right|_{\text{bare}}|\psi_{\text{p}}\rangle\,. \tag{5.38}$$

Using the chain rule similarly to Eq. (5.25), neglecting the variations of the valence

Table 5.1 – Screening effects in electron density and Coulomb kernel for the various forms of self-interaction.

Screening	many-body	one-body	bare
Electron density	✓	✓	✗
Coulomb kernel	✓	✗	✗

wave functions with q, and noticing that

$$\langle\psi_{\mathrm{p}}|\frac{|\psi_{\mathrm{p}}\rangle\langle\psi_{\mathrm{p}}|}{|\mathbf{r}-\mathbf{r}'|}|\psi_{\mathrm{p}}\rangle = \langle\psi_{\mathrm{p}}|V_{\mathrm{H}}[n_{\mathrm{p}}]|\psi_{\mathrm{p}}\rangle\,, \tag{5.39}$$

we get

$$\left.\frac{d\epsilon^{\alpha}_{\mathrm{p}}(q)}{dq}\right|_{\mathrm{bare}} = -\langle\psi_{\mathrm{p}}|\left\{(1-\alpha)V_{\mathrm{H}}[n_{\mathrm{p}}]+\int d\mathbf{r}\,\frac{\delta V^{\alpha}_{\mathrm{xc}\sigma_{\mathrm{p}}}[n_{\uparrow},n_{\downarrow}]}{\delta n_{\sigma_{\mathrm{p}}}(\mathbf{r})}n_{\mathrm{p}}(\mathbf{r})\right\}|\psi_{\mathrm{p}}\rangle\,. \tag{5.40}$$

Considering that $V^{\alpha}_{\mathrm{xc}\sigma_{\mathrm{p}}} = (1-\alpha)V_{\mathrm{x}\sigma_{\mathrm{p}}} + V_{\mathrm{c}\sigma_{\mathrm{p}}}$ [cf. Eq. (2.8)], one finds that the right hand side of Eq. (5.40) vanishes for $\alpha = 1$, apart from weaker correlation terms. Hence, the piecewise linearity condition of Eq. (4.4) is satisfied for $\alpha^{\mathrm{bare}}_{\mathrm{k}} = 1$. In the limit in which the electron screening is turned off, the many-body and one-body forms of self-interaction coincide and are equal to

$$\begin{aligned}\Delta E^{\alpha}(q)|_{\mathrm{bare}} = {} & -(1-\alpha)\left[(q-q^{\mathrm{bare}}_{\mathrm{k}})^2-(q^{\mathrm{bare}}_{\mathrm{k}})^2\right] \\ & \cdot\left\{E_{\mathrm{H}}[n_{\mathrm{p}}]+\frac{1}{2}\int d\mathbf{r}d\mathbf{r}'\,\frac{\delta^2 E_{\mathrm{xc}}[n_{\uparrow},n_{\downarrow}]}{\delta n_{\sigma_{\mathrm{p}}}(\mathbf{r})\delta n_{\sigma_{\mathrm{p}}}(\mathbf{r}')}n_{\mathrm{p}}(\mathbf{r})n_{\mathrm{p}}(\mathbf{r}')\right\}.\end{aligned} \tag{5.41}$$

A summary of the screening effects in the density and Coulomb kernel for the various forms of self-interaction studied in this work is given in Table 5.1.

It is interesting to note that the expression in Eq. (5.41) evaluated at $\alpha = 0$ essentially coincides with the self-interaction energy correction found by Sio *et al.* [49, 50]:

$$\Delta E^{0}(q)|_{\mathrm{bare}^*} = -q^2\left\{E_{\mathrm{H}}[n_{\mathrm{p}}]+\frac{1}{2}\int d\mathbf{r}d\mathbf{r}'\,\frac{\delta^2 E_{\mathrm{xc}}[n_{\uparrow},n_{\downarrow}]}{\delta n_{\sigma_{\mathrm{p}}}(\mathbf{r})\delta n_{\sigma_{\mathrm{p}}}(\mathbf{r}')}n_{\mathrm{p}}(\mathbf{r})n_{\mathrm{p}}(\mathbf{r}')\right\}. \tag{5.42}$$

Indeed, in their derivation, Sio *et al.* neglected the electron screening effects like in our bare approximation. The only difference between the two expressions arises from the q-dependent prefactor, which is related to the different definitions adopted for the self-interaction-corrected energy functional. In our case [cf. Eq. (5.16)],

$$E^0(q)\big|_{\mathrm{bare}} + \Delta E^0(q)\big|_{\mathrm{bare}} = E^0(0) - q\,\epsilon^0_{\mathrm{p}}(q^{\mathrm{bare}}_{\mathrm{k}})\big|_{\mathrm{bare}}\,, \tag{5.43}$$

whereas, in the case of Sio *et al.*, the total energy $E^0(q)$ is expanded in q around $q = 0$ and the second order derivative of $E^0(q)$ with respect to q is removed. This results in

$$E^0(q)\big|_{\mathrm{bare}} + \Delta E^0(q)\big|_{\mathrm{bare}*} = E^0(0) - q\epsilon^0_{\mathrm{p}}(0). \tag{5.44}$$

Hence, in the absence of electron screening, the difference between our bare expression and that derived in Refs. [49, 50] can be associated with the slope of the linear dependence of self-interaction corrected energy functional with q, which corresponds to the polaron level at $q = 0$ in the case of Sio *et al.* and to the polaron level at $q = q^{\mathrm{bare}}_{\mathrm{k}}$ in our case. This comparison clarifies the underlying assumptions leading to previous expressions for the self-interaction in the literature. In particular, we remark that when the electron screening is allowed, as in realistic conditions, the self-interaction-corrected energy $E^0(q) + \Delta E^0(q)|_{\mathrm{bare}*}$ no longer satifies the piecewise linearity condition.

In Table 5.2, we quantify the differences between the various forms of self-interaction discussed in this work by comparing the corresponding polaron formation energies. The formation energies free from many-body self-interaction are calculated with the PBE0(α_{k}) functional [cf. Fig. 4.5(d-f)]. The formation energies corrected for the one-body self-interaction are obtained by extrapolating the results in Fig. 4.5(d-f) to the fraction of Fock exchange $\alpha = 1$. We determine the formation energies corrected for the self-interaction proposed by Sio *et al.* as

$$E^0_{\mathrm{f}}(Q)\big|_{\mathrm{bare}*} = E^0_{\mathrm{f}}(Q) + \ \Delta E^0(Q)\big|_{\mathrm{bare}*}\,, \tag{5.45}$$

where $E^0_{\mathrm{f}}(Q)$ corresponds to the formation energies at $\alpha = 0$ in Figs. 4.5(d-f) [cf. Eq. (4.1)] and $\Delta E^0(Q)|_{\mathrm{bare}*}$ is evaluated using the wave functions obtained with PBE0(α_{k}). As already pointed out in Ref. [141], the binding energies free from one-body self-interaction are considerably larger than those corrected for many-body self-interaction, because of the large shift of the band edges with α [cf. Figs. 4.5(a-c)]. Moreover, we also find larger values for the formation energies

Table 5.2 – Polaron binding energies corrected for different forms of self-interaction. For self-trapped polarons, the binding energy coincides with the formation energy in absolute value. In the case of α-SiO$_2$, the binding energy measures the stability of the hole localized at one O atom with respect to the hole delocalized over four O atoms. The binding energies free from many-body and one-body self-interaction are obtained with PBE0(α_k) and PBE0($\alpha = 1$), respectively. The binding energy including the self-interaction correction proposed by Sio *et al.* is obtained through Eq. (5.45).

System	Many-body	One-body	Eq. (5.45)
BiVO$_4$	0.63	7.73	3.34
MgO	0.53	3.88	1.98
α-SiO$_2$	1.25	3.83	1.56

corrected with $\Delta E^0(Q)|_{\mathrm{bare}^*}$, which reflects the neglect of screening effects in Eq. (5.42).

5.6 Screening model

The many-body self-interaction corrections $\Delta E^\alpha(q)|_\mathrm{mb}$ and $\Delta\epsilon_\mathrm{p}^\alpha(q)\big|_\mathrm{mb}$ depend on the parameters α_k and q_k defined by Eqs. (5.14) and (5.12). In principle, the evaluation of these parameters requires the use of hybrid functionals on the polaron supercell. However, computationally expensive hybrid functional calculations can be avoided.

Here, we develop an electrostatic screening model to estimate α_k and q_k. The model is based on the following assumptions. First, as far as the polaron state is concerned, we consider to be dominant the Hartree-like terms, including the diagonal Fock exchange contribution. Second, we neglect the variations of the wave functions with α. Third, we describe the variations of the total electron density n upon polaron occupation f according to classical electrostatics,

$$\frac{dn(f)}{df} = \frac{n_\mathrm{p}}{\varepsilon_\infty}, \tag{5.46}$$

where ε_∞ accounts for the electron response of the system.

We first focus on α_k. Applying the Hellmann-Feynman theorem to both sides of

Eq. (5.20), we obtain

$$\langle\psi_{\mathrm{p}}|\frac{d\mathcal{H}^{\alpha}_{\sigma_{\mathrm{p}}}(q)}{dq}|\psi_{\mathrm{p}}\rangle = \left(1-\frac{\alpha}{\alpha_{\mathrm{k}}}\right)\langle\psi_{\mathrm{p}}|\frac{d\mathcal{H}^{0}_{\sigma_{\mathrm{p}}}(q)}{dq}|\psi_{\mathrm{p}}\rangle\,. \tag{5.47}$$

Considering only the Hartree-like contributions and using the screening model in Eq. (5.46), we write Eq. (5.47) as

$$\left(\frac{1}{\varepsilon_\infty}-\alpha\right)E_{\mathrm{H}}[n_{\mathrm{p}}] = \left(1-\frac{\alpha}{\alpha_{\mathrm{k}}}\right)\frac{1}{\varepsilon_\infty}E_{\mathrm{H}}[n_{\mathrm{p}}], \tag{5.48}$$

from which one derives $\alpha_{\mathrm{k}} = 1/\varepsilon_\infty$, which is a common approximation in the literature [19, 40, 167, 169–172]. This confirms the validity of the assumptions of our electrostatic model.

We now turn to q_{k}. Starting from Eq. (5.32), the one-body self-interaction energy correction at $\alpha = 0$ is given by

$$\Delta E^0(Q)\big|_{\mathrm{ob}} = \Delta E^0(Q)\big|_{\mathrm{mb}} - \Delta E^1(Q)\big|_{\mathrm{mb}} = -\frac{1}{2}\frac{1}{\alpha_{\mathrm{k}}}\Big[(Q-q_{\mathrm{k}})^2 - q_{\mathrm{k}}^2\Big]\frac{d^2E^0(q)}{dq^2}. \tag{5.49}$$

For convenience, we rewrite the right-hand side of Eq. (5.49) in terms of the polaron occupation rather than the polaron charge. Hence, we introduce the occupation f_{k} pertaining to q_{k} such that $f_{\mathrm{k}} = -q_{\mathrm{k}}$ for electron polarons, and $f_{\mathrm{k}} = 1 - q_{\mathrm{k}}$ for hole polarons. Then, in the case of an electron polaron ($Q = -1$), Eq. (5.49) becomes

$$\Delta E^0(Q)\big|_{\mathrm{ob}} = -\frac{1}{2}\frac{1}{\alpha_{\mathrm{k}}}\Big[(1-f_{\mathrm{k}})^2 - (f_{\mathrm{k}})^2\Big]\frac{d^2E^0(f)}{df^2}. \tag{5.50}$$

Proceeding in the same way as in Eq. (5.47) and taking $\alpha_{\mathrm{k}} = 1/\varepsilon_\infty$, we get

$$\Delta E^0(Q)\big|_{\mathrm{ob}} \approx E_{\mathrm{H}}[f_{\mathrm{k}}n_{\mathrm{p}}] - E_{\mathrm{H}}[(1-f_{\mathrm{k}})n_{\mathrm{p}}]. \tag{5.51}$$

For $f_{\mathrm{k}} = 1/\varepsilon_\infty$, this result lends itself to a meaningful physical interpretation. To the extent that the Hartree contributions are dominant, the right-hand side of Eq. (5.51) can be seen as the difference between the one-body self-interaction of the screened polaron density $n_{\mathrm{p}}/\varepsilon_\infty$ and the one-body self-interaction of the polaron screening density $-(1-1/\varepsilon_\infty)n_{\mathrm{p}}$, as in classical electrostatics. This is physically meaningful because in the Hartree-Fock regime, the self-interaction of the bare polaron density is already cancelled and the first term on the right-hand side accounts for the self-interaction of the polaron screening charge. At variance,

Table 5.3 – Parameters α_k and q_k calculated with PBE0(α) and with our electrostatic screening model.

	Hybrid functional			Screening model		
System	α_k	q_k	E_f	α_k	q_k	E_f
$\mathrm{BiVO_4}$	0.14	−0.20	−0.63	0.17	−0.17	−0.62
MgO	0.34	+0.62	−0.53	0.36	+0.64	−0.40
α-$\mathrm{SiO_2}$	0.45	+0.60	−3.11	0.44	+0.56	−3.03

in PBE, the screened polaron density needs to be corrected in its entirety, which is taken care of by the second term on the right-hand side. An equivalent reasoning applies to hole polarons and also leads to $f_\mathrm{k} = 1/\varepsilon_\infty$. Thus, we take $q_\mathrm{k} = -1/\varepsilon_\infty$ for electron polarons and $q_\mathrm{k} = 1 - 1/\varepsilon_\infty$ for hole polarons.

We evaluate the accuracy of our screening model for α_k and q_k by comparison with the reference PBE0(α_k) values calculated through Eqs. (5.14) and (5.12). We find that our approximate values for α_k and q_k deviate from the reference values by at most 0.03 and 0.04, respectively (cf. Table 5.3). This further confirms the validity of the electrostatic screening model.

Furthermore, using the values of α_k and q_k determined with the screening model, we calculate the polaron formation energy resulting from the application of our many-body self-interaction corrections $\Delta E^0(q)\big|_\mathrm{mb}$ and $\Delta\epsilon_\mathrm{p}^0(q)\big|_\mathrm{mb}$ to the PBE energetics. We hence introduce the following many-body self-interaction corrected formation energy at PBE

$$E_\mathrm{f}^\mathrm{0sic}(Q) = Q[\epsilon_\mathrm{b}^{\alpha_\mathrm{k}} - \epsilon_\mathrm{p}^0(q_\mathrm{k})] + [E^0(0) - E_\mathrm{ref}^0], \tag{5.52}$$

where the band-edge $\epsilon_\mathrm{b}^{\alpha_\mathrm{k}}$ can be determined through a simple hybrid-functional calculation for the primitive cell of the pristine bulk system. This expression is targeted to reproduce the formation energy obtained with the hybrid functional PBE0(α_k), with an accuracy relying on the assumption of linearity of the polaron level with α and q. Using the wave functions the wave functions $\psi_{i\sigma}^{\gamma_\mathrm{k}}$ and the geometry $\mathbf{R}_Q^{\gamma_\mathrm{k}}$, we find formation energies of −0.62 eV, −0.40 eV, −3.03 eV for $\mathrm{BiVO_4}$, MgO, and α-$\mathrm{SiO_2}$, respectively. These values differ from the PBE0(α_k) results by 0.01, 0.13, and 0.08 eV, which corresponds to 0.3%, 1.6%, and 0.8% of the band gaps in the three cases, respectively. This agreement corroborates the validity of the involved assumptions and approximations.

5.7 Connection with other previous literature

Following the work of Lany and Zunger [17], the electron addition energy can be expressed as

$$E^{\alpha}(q) - E^{\alpha}(0) = -q\epsilon^{\alpha}_{\mathrm{p}}(0) + \Pi^{\alpha}_{\mathrm{p}}(q) + \Sigma^{\alpha}_{\mathrm{p}}(q), \tag{5.53}$$

where $\Pi^{\alpha}_{\mathrm{p}}$ is defined as self-interaction energy of the polaron in the absence of electron screening, and $\Sigma^{\alpha}_{\mathrm{p}}$ is the energy contribution arising from wave-function relaxation. We here find the expression of $\Pi^{\alpha}_{\mathrm{p}}$ and $\Sigma^{\alpha}_{\mathrm{p}}$ within our formulation. We start by expanding the total energy $E^{\alpha}(q)$ in q around $q = 0$:

$$E^{\alpha}(q) - E^{\alpha}(0) = q\left.\frac{dE^{\alpha}(q)}{dq}\right|_{0} + \frac{q^2}{2}\frac{d^2E^{\alpha}(q)}{dq^2} = -q\epsilon^{\alpha}_{\mathrm{p}}(0) + \frac{q^2}{2}\frac{d^2E^{\alpha}(q)}{dq^2}, \tag{5.54}$$

where we used Janak's theorem. Next, we split the second order derivative of $E^{\alpha}(q)$ with respect to q into bare and screening contributions, namely

$$\frac{d^2E^{\alpha}(q)}{dq^2} = \left.\frac{d^2E^{\alpha}(q)}{dq^2}\right|_{\mathrm{bare}} + \left(\frac{d^2E^{\alpha}(q)}{dq^2} - \left.\frac{d^2E^{\alpha}(q)}{dq^2}\right|_{\mathrm{bare}}\right). \tag{5.55}$$

We remark that

$$\frac{d^2E^{\alpha}(q)}{dq^2} = \left(1 - \frac{\alpha}{\alpha_{\mathrm{k}}}\right)\frac{d^2E^{0}(q)}{dq^2}, \tag{5.56}$$

and that, similarly to Eq. (5.40),

$$\left.\frac{d^2E^{\alpha}(q)}{dq^2}\right|_{\mathrm{bare}} = (1-\alpha)\left.\frac{d^2E^{0}(q)}{dq^2}\right|_{\mathrm{bare}}. \tag{5.57}$$

Then, comparing Eqs. (5.53) and (5.54), and using Eq. (5.42), one identifies the following expressions for $\Pi_{\mathrm{p}}^{\alpha}$ and $\Sigma_{\mathrm{p}}^{\alpha}$:

$$\Pi_{\mathrm{p}}^{\alpha}(q) = \frac{1}{2}(1-\alpha)q^2 \left.\frac{d^2E^0(q)}{dq^2}\right|_{\mathrm{bare}} = (1-\alpha)\,\Delta E^0(q)\big|_{\mathrm{bare}^*}\,, \tag{5.58}$$

$$\Sigma_{\mathrm{p}}^{\alpha}(q) = \frac{1}{2}\left(1-\frac{\alpha}{\alpha_{\mathrm{k}}}\right)q^2\frac{d^2E^0(q)}{dq^2} - (1-\alpha)\,\Delta E^0(q)\big|_{\mathrm{bare}^*}\,. \tag{5.59}$$

Through our formulation, we thus find a connection between the approaches in Ref. [17] and Refs. [49, 50].

5.8 Discussion

In conclusion, we developed a unified theoretical formulation encompassing many-body and one-body forms of self-interaction. We found an analytic expression for both forms of self-interaction and highlighted their connection in terms of the dielectric constant. In particular, the many-body self-interaction accounts for the presence of electron screening in the Coulomb kernel, which is not accounted for in the one-body self-interaction. Moreover, the two forms of self-interaction are found to coincide when the electron screening is turned off. This analysis thus confers superiority to the notion of many-body self-interaction with respect to that of one-body self-interaction.

It is of interest to identify a semilocal functional incorporating the many-body self-interaction corrections of the polaron state in a self-consistent calculation. However, the variational minimization of the functional $E^0 + \Delta E^0|_{\mathrm{mb}}$ carries some limitations. On the one hand, this would require the knowledge of q_{k}, which is inherent to the hybrid-functional calculation, as can be seen in Eq. (5.12). On the other hand, such a variational implementation would not guarantee polaron localization, since the self-interaction of the electron states pertaining to the relevant delocalized band edge has not been corrected. For instance, in the case of the hole polaron in MgO, the polaron level $\epsilon_{\mathrm{p}}^{\alpha_{\mathrm{k}}}$ free from many-body self-interaction is in resonance with the PBE valence band [cf. Fig. 4.5(b)]. The competition between localized and delocalized states prevents polaron localization in this case. Indeed, to achieve polaron localization and a negative formation energy, the polaron level must lie sufficiently deep in the band gap to overcome the energy cost of lattice distortions [cf. Eq. (4.6)].

6 Semilocal γDFT scheme for polaron localization

We develop a semilocal density functional scheme that addresses the many-body self-interaction of polarons, thereby overcoming the limitations of standard density functional theory. Polaron localization is achieved through the addition of a weak local potential in the Kohn-Sham Hamiltonian that enforces the piecewise linearity of the total energy upon partial electron occupation. The implementation of this scheme does not produce any computational overhead compared to standard semilocal calculations and achieves fast convergence. Possible resonances involving the polaron state and the delocalized band states are addressed by including to the Hamiltonian a scissor operator, which is constructed with the self-consistent wave functions. This approach results in polaron properties, including the atomic geometry, the electron density and the formation energy, which are close to those achieved with a hybrid functional that similarly satisfies the piecewise linearity condition. This suggests that addressing the many-body self-interaction results in a polaron description that is robust with respect to the functional adopted. We illustrate our approach through applications to the electron polaron in $BiVO_4$, the hole polaron in MgO, and the Al-trapped hole in α-SiO_2.

This chapter is adapted from:
Ref. [141]: S. Falletta, A. Pasquarello, *Many-body self-interaction and polarons*, Physical Review Letters 129, 126401 (2022).
Ref. [142]: S. Falletta, A. Pasquarello, *Polarons free from many-body self-interaction in density functional theory*, Physical Review B 106, 125119 (2022).

6.1 Introduction

Given the superiority of the many-body self-interaction over the one-body self-interaction, we are interested in localizing polarons free from many-body self-interaction at the semilocal level of theory. Considering that the localized and delocalized forms of the polaron state are generally found in close energetic competition [175, 176], polaron localization could be achieved by favoring the localized solution over the delocalized one. Such an approach would have the advantage of avoiding resonances between the electron (hole) polaron level and the conduction (valence) band edge, thereby not requiring accounting for the many-body self-interaction of the band edges. This would enable efficient polaron calculations, thus avoiding computationally-expensive hybrid functional calculations.

6.2 Methodology

We assume that the localization can be achieved by adding a weak local potential to the PBE Hamiltonian in Eq. (2.1), which favors the localized state with respect to the delocalized band states. We denote this potential V_σ^γ, where γ is a parameter that regulates the strength of the potential. This leads to the following set of equations

$$(\mathcal{H}_\sigma^0 + V_\sigma^\gamma)\psi_{i\sigma}^\gamma = \epsilon_{i\sigma}^\gamma \psi_{i\sigma}^\gamma, \tag{6.1}$$

where $\psi_{i\sigma}^\gamma$ and $\epsilon_{i\sigma}^\gamma$ are the resulting wave functions and eigenvalues, respectively. We find that a suitable expression for V_σ^γ is

$$V_\sigma^\gamma(q) = q\gamma \frac{\partial V_{\mathrm{xc}\sigma}}{\partial q}. \tag{6.2}$$

The use of the exchange-correlation potential in the definition of V_σ^γ ensures its locality. Using the chain rule for the derivative of $V_{\mathrm{xc}\sigma}$ with respect to q and considering Eq. (5.1), V_σ^γ can be rewritten as

$$V_\sigma^\gamma(q) = -q\gamma \int d\mathbf{r}\, \frac{\delta V_{\mathrm{xc}\sigma}^0[n_\uparrow^\gamma, n_\downarrow^\gamma]}{\delta n_{\sigma_\mathrm{p}}^\gamma(\mathbf{r})} n_\mathrm{p}^\gamma(\mathbf{r}), \tag{6.3}$$

where n_σ^γ is the total density in the spin channel σ, and n_p^γ is the density of the polaron state. The dominant contribution to the potential V_σ^γ is given by the exchange term, which only occurs in the spin channel $\sigma = \sigma_{\rm p}$ [cf. Eq. (2.3)]. For $q = 0$, the potential V_σ^γ vanishes, thus recovering the PBE Hamiltonian.

The total energy corresponding to the Kohn-Sham equations in Eq. (6.1) is given by

$$E^\gamma(q) = E^0(q) + \Delta E^\gamma(q), \tag{6.4}$$

where $E^0(q)$ is the semilocal PBE energy, and ΔE^γ the energy correction related to the potential V_σ^γ. We here derive the analytic expression of ΔE^γ.

We assume that the total energy is well described by an expansion up to second order in q [141, 142]. Then, ΔE^γ can be written as

$$\Delta E^\gamma(q) = \Delta E^\gamma(0) + q\,\frac{d\Delta E^\gamma}{dq}\bigg|_{q=0} + \frac{q^2}{2}\frac{d^2(\Delta E^\gamma)}{dq^2}. \tag{6.5}$$

We remark that $\Delta E^\gamma(0) = 0$ since the potential V_σ^γ vanishes at $q = 0$. Moreover, since V_σ^γ is linear in q then also $d(\Delta E^\gamma)/dq$ is linear in q, which thus vanishes at $q = 0$. Hence, by using the chain rule for derivatives with respect to q, Eq. (6.5) can be rewritten as

$$\Delta E^\gamma(q) = \frac{q^2}{2}\sum_{\sigma\sigma'}\int d\mathbf{r}d\mathbf{r}'\,\frac{\delta^2(\Delta E^\gamma)}{\delta n_\sigma^\gamma(\mathbf{r})\delta n_{\sigma'}^\gamma(\mathbf{r}')}\frac{dn_\sigma^\gamma(\mathbf{r})}{dq}\frac{dn_{\sigma'}^\gamma(\mathbf{r}')}{dq}. \tag{6.6}$$

Similarly, the potential V_σ^γ can be expanded in q as follows

$$V_\sigma^\gamma(\mathbf{r}) = q\sum_{\sigma'}\int d\mathbf{r}'\,\frac{\delta V_\sigma^\gamma(\mathbf{r})}{\delta n_{\sigma'}^\gamma(\mathbf{r}')}\frac{dn_{\sigma'}^\gamma(\mathbf{r}')}{dq}. \tag{6.7}$$

Using the variational relation $V_\sigma^\gamma(\mathbf{r}) = \delta(\Delta E^\gamma)/\delta n_\sigma^\gamma(\mathbf{r})$ in Eq. (6.7), and inserting the resulting expression in Eq. (6.6), one gets

$$\Delta E^\gamma(q) = \frac{q}{2}\sum_\sigma\int d\mathbf{r}\,V_\sigma^\gamma(\mathbf{r})\frac{dn_\sigma^\gamma(\mathbf{r})}{dq}, \tag{6.8}$$

which can be easily evaluated by finite differences, namely

$$\Delta E^\gamma(q) = \frac{1}{2}\sum_\sigma\int d\mathbf{r}\,V_\sigma^\gamma(\mathbf{r})[n_\sigma^\gamma(q,\mathbf{r}) - n_\sigma^\gamma(0,\mathbf{r})]. \tag{6.9}$$

We remark that the expression in Eq. (6.9) is valid for any potential V_σ^γ with a prefactor q in V_σ^γ, under the assumption of quadraticity of the total energy with q.

The structural relaxations are performed in the presence of the polaron charge Q through the usual Hellmann-Feynmann forces, as defined in Eq. (2.24). We denote the resulting relaxed geometry of the polaron $\mathbf{R}_Q^\gamma$. We remark that the Hellmann-Feynmann theorem and Janak's theorem are still satisfied when introducing the potential V_σ^γ in the Kohn-Sham equations.

We find the value of the parameter $\gamma = \gamma_\mathrm{k}$ for which the piecewise linearity of the total energy upon electron occupation is enforced, i.e.,

$$\frac{d}{dq}\epsilon_\mathrm{p}^\gamma(q)\bigg|_{\gamma=\gamma_\mathrm{k}} = 0, \tag{6.10}$$

where $\epsilon_\mathrm{p}^\gamma$ is the polaron level. In Eq. (6.10), γ_k and $\mathbf{R}_Q^{\gamma_\mathrm{k}}$ are obtained self-consistently. By using the Hellmann-Feynman theorem, Eq. (6.10) can be rewritten as

$$\frac{d\epsilon_\mathrm{p}^\gamma(q)}{dq} = \langle\psi_\mathrm{p}^{\gamma_\mathrm{k}}|\left(\frac{d\mathcal{H}_{\sigma_\mathrm{p}}^0}{dq} + \frac{dV_{\sigma_\mathrm{p}}^\gamma}{dq}\right)|\psi_\mathrm{p}^{\gamma_\mathrm{k}}\rangle = \frac{d\epsilon_\mathrm{p}^0(q)}{dq} + \langle\psi_\mathrm{p}^{\gamma_\mathrm{k}}|\frac{dV_{\sigma_\mathrm{p}}^{\gamma_\mathrm{k}}}{dq}|\psi_\mathrm{p}^{\gamma_\mathrm{k}}\rangle = 0. \tag{6.11}$$

Using finite-difference expressions, Eq. (6.11) becomes

$$\langle\psi_\mathrm{p}^{\gamma_\mathrm{k}}|V_{\sigma_\mathrm{p}}^{\gamma_\mathrm{k}}(Q)|\psi_\mathrm{p}^{\gamma_\mathrm{k}}\rangle = \epsilon_\mathrm{p}^0(0) - \epsilon_\mathrm{p}^0(Q), \tag{6.12}$$

which gives a self-consistent procedure to evaluate γ_k. We remark that, for a sufficiently large system, finite-size effects in Eq. (6.12) are negligible. For small systems, one needs to take into account the finite-size corrections on the left-hand side of Eq. (6.12).

Since the piecewise linearity condition is satisfied for γ_k, the total energy can be written as

$$E^{\gamma_\mathrm{k}}(Q) = E^{\gamma_\mathrm{k}}(0) - Q\epsilon_\mathrm{p}^{\gamma_\mathrm{k}}. \tag{6.13}$$

Therefore, the corresponding polaron formation energy is

$$E_\mathrm{f}^{\gamma_\mathrm{k}}(Q) = Q(\epsilon_\mathrm{b}^{\gamma_\mathrm{k}} - \epsilon_\mathrm{p}^{\gamma_\mathrm{k}}) + [E^{\gamma_\mathrm{k}}(0) - E_\mathrm{ref}^{\gamma_\mathrm{k}}(0)]. \tag{6.14}$$

The quantities in Eq. (6.14) are all calculated at the semilocal level of theory, thus avoiding computationally expensive hybrid functional calculations. Moreover, the band edge $\epsilon_{\mathrm{b}}^{\gamma_{\mathrm{k}}}$ and the total energies $E^{\gamma_{\mathrm{k}}}(0)$ and $E_{\mathrm{ref}}^{\gamma_{\mathrm{k}}}(0)$ coincide with their respective PBE values, because of the vanishing prefactor q in Eq. (6.2). For simplicity of notation, we consider all energies to be corrected by finite-size effects in all formulas. We denote this semilocal scheme γDFT.

The γDFT scheme guarantees a symmetric treatment in the case of electron and hole polarons. This stems from the fact that the potential V_{σ}^{γ} acts in the same way on all the states, irrespectively of their occupation. Hence, electron and hole polarons, which correspond to the last-occupied and the first-unoccupied Kohn-Sham states, respectively, localize in a analogous manner under the action of this potential.

The γDFT scheme can be compared with previously proposed methods. The idea that a localized potential might be sufficient for correcting the self-interaction through enforcing the piecewise linearity condition has previously been used in the DFT+U scheme [68] and in the scheme proposed by Lany and Zunger [17]. In both these schemes, the U correction applies to specific atomic orbitals. At variance, the γDFT scheme leads to a localized potential, which self-consistently originates from the electron or hole density and which acts on all the states of the system rather than on selected atomic orbitals.

6.3 Computational advantages

In practical calculations, the potential V_{σ}^{γ} in Eq. (6.2) can be implemented through finite differences. For an electron polaron ($q=-1$, $\sigma_{\mathrm{p}}=\uparrow$), we use

$$V_{\sigma}^{\gamma}(-1)=\gamma\Big(V_{\mathrm{xc}\sigma}^{0}[n_{\uparrow}^{\gamma}(-1),n_{\downarrow}^{\gamma}(-1)]-V_{\mathrm{xc}\sigma}^{0}[n_{\uparrow}^{\gamma}(-1)-n_{\mathrm{p}}^{\gamma}(-1),n_{\downarrow}^{\gamma}(-1)]\Big). \tag{6.15}$$

where the densities are found through self-consistent calculations with $q=-1$. Analogously, for a hole polaron ($q=+1$, $\sigma_{\mathrm{p}}=\downarrow$), we have

$$V_{\sigma}^{\gamma}(+1)=\gamma\Big(V_{\mathrm{xc}\sigma}^{0}[n_{\uparrow}^{\gamma}(+1),n_{\downarrow}^{\gamma}(+1)]-V_{\mathrm{xc}\sigma}^{0}[n_{\uparrow}^{\gamma}(+1),n_{\downarrow}^{\gamma}(+1)+n_{\mathrm{p}}^{\gamma}(+1)]\Big). \tag{6.16}$$

The expressions in Eqs. (6.15) and (6.16) can be easily determined using available exchange-correlation subroutines.

In previous one-body self-interaction schemes [50, 57, 58], it is common to adopt the restricted open-shell constraint, which consists in setting $\psi_{i\uparrow} = \psi_{i\downarrow}$ for all states. The restricted open-shell condition is useful to avoid multiminima problems encountered in self-interaction-corrected calculations [50, 57, 58]. However, this approximation enforces the same screening in the two spin channels, which is not generally the case as seen in Fig. 5.2. This could affect the polaron energetics. At variance, our methodology does not require the restricted open-shell constraint and reaches convergence as fast as standard PBE calculations.

The γDFT scheme guarantees the orthogonalization of the wave functions without requiring any modification of the available algorithms for the diagonalization of the Hamiltonian, like the Davidson or the conjugate-gradient method. Indeed, the potential V_σ^γ acts as a local potential on all the states in the spin channel σ [cf. Eq. (6.1)]. This is a great advantage compared to previous self-interaction approaches [50, 55, 57, 58], which feature orbital-dependent Hamiltonians [21, 56, 177, 178]. In particular, in the self-interaction correction scheme of Perdew and Zunger [55], a different Hamiltonian acts on each state. In more recent self-interaction methods [49, 50, 57, 58], a distinct Hamiltonian is only used for the polaron state. Such orbital-dependent Hamiltonians require more sophisticated diagonalization algorithms [56], which are not necessary in our methodology.

The γDFT scheme is only marginally affected by the rotational invariance problem [21, 177, 178]. We note that the potential V_σ^γ depends on the polaron density n_p^γ. In the case of hole polarons, the occupied manifold preserves the rotational invariance under unitary transformations, since n_p^γ pertains to an unoccupied state. On the other hand, in the case of electron polarons, the rotational invariance is not formally satisfied, since the polaron state is occupied. However, the diagonalization of the Hamiltonian $\mathcal{H}_\sigma^0 + V_\sigma^\gamma$ is only affected to a minor extent because the energy separation between the polaron level and the other occupied levels is generally sizable. This is a great advantage of our methodology compared to previous self-interaction-correction schemes [50, 55, 57, 58].

We implemented the γDFT scheme in the code PW of QUANTUM ESPRESSO [153]. In particular, this implementation has been merged in the developer version of QUANTUM ESPRESSO and it is ready to be incorporated in the official release of the code. In the self-consistent iteration, the polaron density n_p^γ is mixed with the polaron densities at previous steps in the same way as the total electron density.

Then, the addition of the potential V_σ^γ requires only minimal changes to existing codes. Implementation details are given in Appendix B.

6.4 Self-consistent scissor operator

In the γDFT scheme, the inclusion of the potential V_σ^γ to the semilocal Hamiltonian increases the energy separation between the polaron level and the respective delocalized band edge. In the case of electron polarons, the polaron level is stabilized by going down in energy with respect to the conduction band. At variance, in the case of hole polarons, the polaron level is stabilized by going up in energy with respect to the valence band. Considering that in semilocal density functional theory the band gap is underestimated, resonances involving the electron (hole) polaron state with the valence (conduction) band states could occur, which may prevent polaron localization.

This problem can be overcome by including in the Hamiltonian a scissor operator $\mathcal{S}_\sigma$ that artificially increases the band gap of the system. The scissor operator only affects electron bands that are unrelated to the polaronic state. This allows one to address resonances between the polaron level and the delocalized band states, without affecting the polaron properties. The adopted scissor operator has the following expression

$$\mathcal{S}_\sigma = \Delta \sum_{i \in \mathcal{M}_\sigma^\gamma} |\psi_{i\sigma}^\gamma\rangle\langle\psi_{i\sigma}^\gamma| \,, \tag{6.17}$$

where $\psi_{i\sigma}^\gamma$ are the wave functions obtained in the self-consistent optimization of the Kohn-Sham equations, and Δ is a constant. For electron polarons, $\mathcal{M}_\sigma^\gamma$ denotes the manifold of valence-band states and Δ is taken to be negative, while for hole polarons $\mathcal{M}_\sigma^\gamma$ denotes the manifold of conduction-band states and Δ is taken to be positive. The energy levels of all states belonging to the manifold $\mathcal{M}_\sigma^\gamma$ are then shifted by the amount Δ. When $\mathcal{M}_\sigma^\gamma$ denotes the valence band manifold, the inclusion of $\mathcal{S}_\sigma$ in the Hamiltonian shifts the total energy by a contribution $N\Delta$, where N is the number of valence electrons. In Appendix A, we show an example of scissor operator to open band gaps in bulk systems.

We implemented the self-consistent scissor operator in the code PW of QUANTUM ESPRESSO [153]. This implementation is incorporated in the developer version of the code. Details on the implementation are given in Appendix B.

6.5 Results

First, we calculate the value γ_k for which the piecewise linearity condition is satisfied. Following Eq. (6.10), we perform structural relaxations for different values of γ and obtain the corresponding polaron geometries $\mathbf{R}_Q^\gamma$. For each structure $\mathbf{R}_Q^\gamma$, we calculate the energy levels $\epsilon_\mathrm{p}^\gamma(0)$ and $\epsilon_\mathrm{p}^\gamma(Q)$ pertaining to the charge states 0 and Q, as illustrated in Fig. 6.1. We thus determine γ_k such that those energy levels coincide, resulting in $\gamma_\mathrm{k} = 1.80$, 1.96, 2.40 for BiVO$_4$, MgO, and α-SiO$_2$, respectively. In all cases, the polaron level is situated in the band gap and provides the required electronic energy gain to counterbalance the energy cost of the lattice distortions. This yields stable localized polarons.

We now present the electronic and atomic properties obtained with the γDFT scheme in comparison with the hybrid-functional PBE0(α_k) results. We show in Figs. 6.2(a-c) the polaron density integrated over the xy planes, namely

$$n_\mathrm{p}(z) = \int dxdy\, n_\mathrm{p}(x, y, z), \tag{6.18}$$

and find an excellent agreement between the two schemes. To compare the polaron structures, we report in Table 7.2 the lengths of the distorted bonds. For all investigated polarons, the agreement between the semilocal and the hybrid-functional values is very good. The differences are all within 0.03 Å, except for the weak Al-O

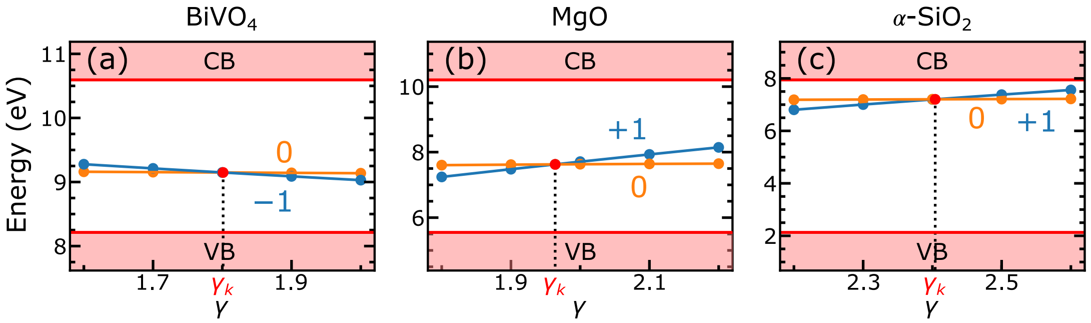

Figure 6.1 – Polaron energy levels $\epsilon_\mathrm{p}^\gamma(Q)$ and $\epsilon_\mathrm{p}^\gamma(0)$ for the structure $\mathbf{R}_Q^\gamma$ as a function of γ for the electron polaron in BiVO$_4$, the hole polaron in MgO, and the Al-trapped hole in α-SiO$_2$. The polaron levels are identified by their respective polaron charge. The value γ_k is found such that $\epsilon_\mathrm{p}^{\gamma_\mathrm{k}}(Q) = \epsilon_\mathrm{p}^{\gamma_\mathrm{k}}(0)$.

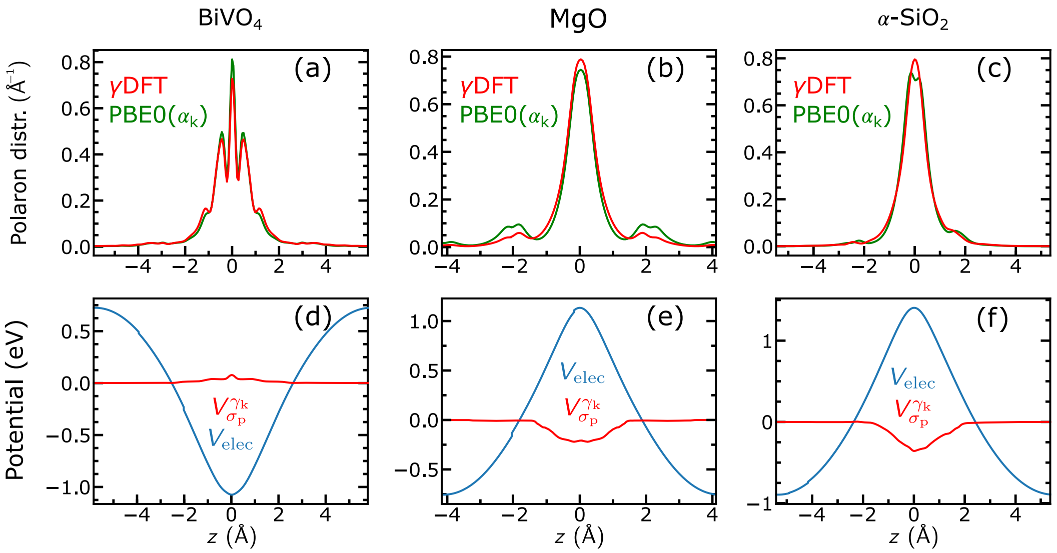

Figure 6.2 – (a-c) Polaron densities for the electron polaron in BiVO$_4$, the hole polaron in MgO, and the Al-trapped hole in α-SiO$_2$ as obtained with the hybrid functional PBE0($\alpha_{\rm k}$) and with the γDFT scheme. The polaron densities are integrated over xy-planes. (d-f) Electrostatic potential $V_{\rm elec} = V_{\rm H}[Qn_{\rm p}^{\gamma_{\rm k}}]$ and potential $V_{\sigma_{\rm p}}^{\gamma_{\rm k}}(Q)$ averaged over xy-planes ($Q = -1$ for electron polarons, $Q = +1$ for hole polarons).

bond in α-SiO$_2$, which differs by 0.12 Å.

Next, we determine the polaron formation energies and give the results in Table 6.2. With our semilocal scheme, we find formation energies of -0.44 eV, -0.50 eV, and -2.75 eV for BiVO$_4$, MgO, and α-SiO$_2$, respectively. These values differ from the hybrid functional values by 0.19, 0.03, and 0.36 eV, respectively. This agreement is remarkable given the large differences in formation energies found as a function of α in Figs. 4.5(d-f). Furthermore, this agreement suggests that enforcing the piecewise linearity condition leads to robust polaron formation energies, irrespective of the choice of the functional.

We validate the expression of the energy $\Delta E^{\gamma}(q)$ in Eq. (6.9) by calculating the difference between two ways of estimating the total energy $E^{\gamma_{\rm k}}(q)$, namely

$$\delta = \left|[E^0(q) + \Delta E^{\gamma_{\rm k}}(q)] - [E^0(0) - q\epsilon_{\rm p}^{\gamma_{\rm k}}]\right|, \tag{6.19}$$

which should vanish by definition of $\gamma_{\rm k}$, because of the piecewise linearity condition. For the three polarons considered, we find a mean average δ of 0.1 eV. This agreement is satisfactory, considering the assumption of quadraticity underlying

Table 6.1 – Bond lengths (in Å) of the distorted polaronic structures ($q = Q$) as obtained with the hybrid functional PBE0(α_k) and with the semilocal γDFT scheme. For α-SiO$_2$, we give the lengths of the short/long Al-O bonds. For reference, we also report the corresponding bond lengths as obtained with PBE in the absence of the polaron ($q = 0$).

	$q = 0$	$q = Q$	
System	PBE	γDFT	PBE0(α_k)
BiVO$_4$	1.73	1.82	1.80
MgO	2.11	2.23	2.20
α-SiO$_2$	1.74/1.74	1.71/2.03	1.69/1.91

Table 6.2 – Polaron formation energy obtained with the hybrid functional PBE0(α_k) and with the semilocal γDFT scheme. Energies are in eV.

System	γDFT	PBE0(α_k)
BiVO$_4$	-0.44	-0.63
MgO	-0.50	-0.53
α-SiO$_2$	-2.75	-3.11

Eq. (6.9).

The γDFT scheme allows one to carry out convergence tests with cell size and **k**-point sampling overcoming computational limitations inherent to hybrid-functional calculations. We calculate the polaron formation energy for larger supercell sizes and finer **k**-point sampling for the three systems studied in this work, as given in Table 6.3. The converged results deviate by at most 0.07 eV from the results in Table 6.2. This further corroborates the accuracy of the employed finite-size correction scheme [117]. For the electron polaron in BiVO$_4$, we calculate with $\alpha_\mathrm{k} = 0.14$ a converged formation energy of -0.38 eV, to be compared with the value of -1.09 eV obtained in Ref. [41] with $\alpha = 0.22$ and with a different electronic-structure set-up. This is consistent with the variation of the formation energy by -0.65 eV when α increases from 0.14 to 0.22, as can seen in Fig. 4.5(d). For the hole polaron in MgO, the converged formation energy with $\alpha_\mathrm{k} = 0.34$ is found to be -0.49 eV, in good agreement with the value of -0.38 eV found in Ref. [117] with a different electronic structure set-up and with $\alpha = 0.33$. Accounting for the variation of the formation energy when α goes from 0.33 to 0.34 [cf. Fig. 4.5(e)], reduces the discrepancy to only 0.04 eV.

Table 6.3 – Polaron formation energies $E_\mathrm{f}^{\gamma_\mathrm{k}}$ as calculated with the γDFT scheme for various supercell sizes and $\mathbf{k}$-point samplings.

System	Number of atoms	$\mathbf{k}$-point grid	$E_\mathrm{f}^{\gamma_\mathrm{k}}$
$BiVO_4$	96	Γ	−0.44
	96	2×2×2	−0.36
	216	2×2×2	−0.38
MgO	64	Γ	−0.50
	64	2×2×2	−0.49
	512	2×2×2	−0.49
α-SiO_2	64	Γ	−2.75
	64	2×2×2	−2.69
	243	2×2×2	−2.68

We remark that the formation energies obtained with the γDFT scheme are close to the PBE0(α_k) values, despite the fact that the band gaps are underestimated like in PBE. This can be understood by considering that the polaron states of interest in our study are mainly constructed with band states to which the polaron belongs, i.e. conduction band states for electron polarons and valence band states for hole polarons. In such conditions, the description of the band gap is thus not a stringent requirement for achieving accurate formation energies.

In the case of MgO, the robustness of the results for the self-trapped hole polaron is of particular interest. Indeed, the experimental situation concerning the self-trapped hole remains difficult to interpret in a clear way [179, 180] and the theoretical description is controversial [39, 48, 117, 181]. In these regards, the hybrid-functional and semilocal schemes with vanishing many-body self-interaction consistently predict a self-trapped hole with almost identical formation energy (see Table 6.2).

It is important to formally investigate the relationship between the formation energies obtained with the semilocal γDFT the and hybrid functional PBE0(α_k) schemes. Indeed, the piecewise linearity in these functionals is achieved in remarkably different ways, either through the local potential $V_\sigma^{\gamma_\mathrm{k}}$ or through the nonlocal Fock exchange terms. The difference between the formation energies in Eqs. (4.6) and (6.14) can be expressed as

$$E_{\mathrm{f}}^{\alpha_{\mathrm{k}}}(Q) - E_{\mathrm{f}}^{\gamma_{\mathrm{k}}}(Q) = Q(\epsilon_{\mathrm{b}}^{\alpha_{\mathrm{k}}} - \epsilon_{\mathrm{b}}^{0}) - Q(\epsilon_{\mathrm{p}}^{\alpha_{\mathrm{k}}} - \epsilon_{\mathrm{p}}^{\gamma_{\mathrm{k}}}), \tag{6.20}$$

where we focus on the electronic gain due to localization, assuming that the cost of lattice distortions is similar in the two schemes. Given the linear dependence of the band-edge levels with α [cf. Fig. 4.5(a-c)], the band contributions in Eq. (6.20) can be expanded in α as

$$\epsilon_{\mathrm{b}}^{\alpha_{\mathrm{k}}} - \epsilon_{\mathrm{b}}^{0} = \alpha_{\mathrm{k}} \frac{d\epsilon_{\mathrm{b}}^{\alpha}}{d\alpha}. \tag{6.21}$$

Moreover, using the linearity of the polaron level with α [cf. Fig. 4.5(a-c)], the polaron terms in Eq. (6.20) can be rewritten as

$$\epsilon_{\mathrm{p}}^{\alpha_{\mathrm{k}}} - \epsilon_{\mathrm{p}}^{\gamma_{\mathrm{k}}} = \epsilon_{\mathrm{p}}^{\alpha_{\mathrm{k}}}(0) - \epsilon_{\mathrm{p}}^{0}(0) = \alpha_{\mathrm{k}} \frac{d\epsilon_{\mathrm{p}}^{\alpha}(0)}{d\alpha}, \tag{6.22}$$

where we used the facts that $\epsilon_{\mathrm{p}}^{\alpha_{\mathrm{k}}}$ and $\epsilon_{\mathrm{p}}^{\gamma_{\mathrm{k}}}$ are constant with q and that $\epsilon_{\mathrm{p}}^{\gamma_{\mathrm{k}}} = \epsilon_{\mathrm{p}}^{0}(0)$ due to the presence of the prefactor q in $V_{\sigma}^{\gamma_{\mathrm{k}}}$ [cf. Eq. (6.2)]. Hence, through the use of Eqs. (6.21) and (6.22), Eq. (6.20) becomes

$$E_{\mathrm{f}}^{\alpha_{\mathrm{k}}}(Q) - E_{\mathrm{f}}^{\gamma_{\mathrm{k}}}(Q) = Q\alpha_{\mathrm{k}} \left[\frac{d\epsilon_{\mathrm{b}}^{\alpha}}{d\alpha} - \frac{d\epsilon_{\mathrm{p}}^{0}(0)}{d\alpha} \right]. \tag{6.23}$$

This expression indicates that when the piecewise linearity is satisfied the formation energies obtained with γDFT and PBE0(α) functionals coincide, provided that the polaron level at $q = 0$ and the associated band edge vary with α in the same way. This condition is generally closely satisfied because these states belong to the same electronic manifold. A schematical representation of Eq. (6.23) is given in Fig. 6.3. This analysis emphasizes the robustness of the polaron formation energies achieved through the enforcement of the piecewise linearity, irrespective of the detailed features of the employed functional.

We verify that $V_{\sigma}^{\gamma_{\mathrm{k}}}(Q)$ is indeed a weak potential. For this purpose, we compare $V_{\sigma_{\mathrm{p}}}^{\gamma_{\mathrm{k}}}(Q)$ and the electrostatic potential $V_{\mathrm{H}}[Qn_{\mathrm{p}}^{\gamma_{\mathrm{k}}}]$ generated by the polaron charge density $Qn_{\mathrm{p}}^{\gamma_{\mathrm{k}}}$, where $Q = -1$ for electron polarons and $Q = +1$ for hole polarons. In Figs. 6.2(d-f), we show these potentials averaged over xy planes as a function of

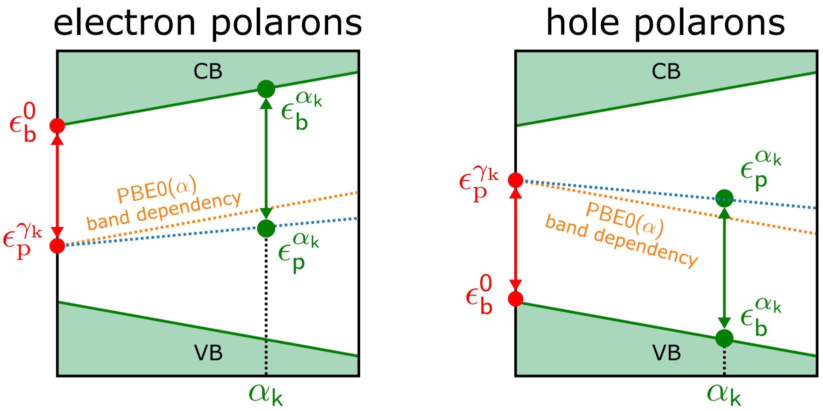
electron polarons
CB
VB
ϵ_b^0
$\epsilon_\mathrm{p}^{\gamma_\mathrm{k}}$
$\epsilon_\mathrm{b}^{\alpha_\mathrm{k}}$
$\epsilon_\mathrm{p}^{\alpha_\mathrm{k}}$
PBE0(α) band dependency
α_k
hole polarons
CB
VB
$\epsilon_\mathrm{p}^{\gamma_\mathrm{k}}$
ϵ_b^0
$\epsilon_\mathrm{p}^{\alpha_\mathrm{k}}$
$\epsilon_\mathrm{b}^{\alpha_\mathrm{k}}$
PBE0(α) band dependency
α_k

Figure 6.3 – Graphical representation related to Eq. (6.23) to show the robustness of polaron formation energies obtained with γDFT and PBE0(α_k) schemes.

the z coordinate, namely

$$V(z) = \frac{1}{\mathcal{A}_{xy}} \int dxdy\, V(x, y, z), \tag{6.24}$$

where $\mathcal{A}_{xy}$ denotes the area of xy planes in the supercell. In all cases, we find that the potential $V_{\sigma_\mathrm{p}}^{\gamma_\mathrm{k}}(Q)$ is considerably weaker than the electrostatic potential. Moreover, the peak of the potential $V_{\sigma_\mathrm{p}}^{\gamma_\mathrm{k}}(Q)$ amounts to a small fraction of an electronvolt [cf. Fig. 6.2(d-f)]. This confirms *a posteriori* that the polaron can be localized by adding a weak potential to the PBE Hamiltonian. Additionally, we remark that the potential $V_{\sigma_\mathrm{p}}^{\gamma_\mathrm{k}}(Q)$ carries an opposite sign with respect to the electrostatic potential. To understand this property, let us focus on the case of electron polarons [e.g., in BiVO$_4$, Fig. 6.2(d)]. The electrostatic potential $V_\mathrm{H}[-n_\mathrm{p}^{\gamma_\mathrm{k}}]$ generated by the polaron charge density results in a potential well which repels the negative charge of the electron polaron. Hence, $V_\mathrm{H}[-n_\mathrm{p}^{\gamma_\mathrm{k}}]$ tends to delocalize the electron polaron charge density. The potential $V_{\sigma_\mathrm{p}}^{\gamma_\mathrm{k}}(Q)$ opposes this electrostatic potential, thereby favoring polaron localization. A similar reasoning applies to the case of hole polarons.

6.6 Discussion

In conclusion, we introduced a scheme that addresses the many-body self-interaction of polarons at the semilocal level of theory. Polaron localization is achieved by the inclusion of a weak local potential in the Kohn-Sham Hamiltonian that enforces the piecewise linearity of the total energy upon electron occupation. Our methodology is particularly advantageous from the computational point of view. In particular, it does not entail any computational overhead compared to regular semilocal calculations, does not suffer from diagonalization problems related to orbital-dependent Hamiltonians, and avoids the use of the restricted open-shell constraint. Possible resonances involving the polaron state and the delocalized band edges are overcome by adding a scissor operator to the Hamiltonian. We applied our scheme to various polarons, and obtained structural and electronic properties of polarons in agreement with those achieved with a hybrid functional satisfying the same constraint. This agreement suggests that the suppression of the many-body self-interaction leads to polaron properties that are robust with respect to the adopted functional. This is expected to hold also in the case of competitive polaronic states at surfaces [182] or in amorphous materials [183].

7 Hubbard U through polaronic defect states

We define a selection criterion or the Hubbard parameter U in DFT+U based on the use of polaronic defect states for the enforcement of the piecewise linearity of the total energy upon electron occupation. A good agreement with results from piecewise linear hybrid functionals is found for the electronic and structural properties of polarons, including the formation energies. The values of U determined in this way are found to give a robust description of the polaron energetics upon variation of the considered state. In particular, we also address a polaron hopping pathway, finding that the determined value of U leads to accurate energetics without requiring a configurational-dependent U. It is emphasized that the selection of U should be based on physical properties directly associated with the orbitals to which U is applied, rather than on more global properties such as band gaps and band widths. For comparison, we also determine U through a well-established linear-response scheme finding noticeably different values of U and consequently different formation energies. Possible origins of these discrepancies are discussed. As case studies, we consider the self-trapped electron in $BiVO_4$, the self-trapped hole in MgO, the Li-trapped hole in MgO, and the Al-trapped hole in α-SiO_2.

This chapter is adapted from:
Ref. [184]: S. Falletta, A. Pasquarello, *Hubbard U through polaronic defect states*, *npj Computational Materials* 8(1), 263.

7.1 Introduction

Density functional theory including a Hubbard U correction has been largely used to overcome limitations of standard density functional theory for correlated systems [68, 185–193], including the account for the electron self-interaction [17, 68]. However, since the preliminary work of Anisimov and co-workers, the determination of the Hubbard U parameter has remained under intense discussion. In 2005, Cococcioni and de Gironcoli introduced a nonempirical linear-response approach based on density-functional perturbation theory [68], which has largely been applied [73, 194–202]. In other studies, the parameter U is chosen to reproduce specific experimental properties, such as band gaps [99, 203], reaction enthalpies [204–206], oxidation energies [207], activation energies [99], atomic structures [208], density of states [209], or magnetic arrangements [210]. Alternative strategies consist in fixing U to yield states in the middle of the band gap [100], to comply with criteria based on energy barriers [211], to have vanishing quasiparticle corrections to the fundamental band gap [212], or to match hybrid-functional results [213]. The parameter U has also been calculated through an alternative linear-response method [214], through unrestricted Hartree-Fock approach [215, 216], through the random-phase approximation [217–220], through Monte Carlo sampling [221], and through machine-learning techniques based on Bayesian optimization [222]. Clearly, a general consensus on the way U should be determined is still lacking, including a criterion for U that suppresses the self-interaction.

7.2 Selection criterion for U

Taking advantage of the our developments in the previous Chapters, we introduce a selection criterion for U that consists in enforcing the piecewise linearity through polaronic defect states associated with the orbitals subject to the correction U. The piecewise linearity can then be determined nonempirically by finding the value $U = U_\mathrm{k}$ such that the concavity of the total energy upon partial electron occupation vanishes, namely

$$\left.\frac{d^2}{dq^2}E^U(q)\right|_{U=U_\mathrm{k}} = 0, \tag{7.1}$$

where q is the fractional charge. Through Janak's theorem, the condition in Eq. (7.1) turns into a constraint on the energy level of the localized state,

$$\frac{d}{dq}\epsilon_{\mathrm{p}}^{U}(q)\bigg|_{U=U_{\mathrm{k}}} = 0, \tag{7.2}$$

which requires the energy level to be independent of electron occupation. Equation (7.2) can be rewritten as

$$\frac{d\epsilon_{\mathrm{p}}^{0}}{dq} + \frac{d}{dq}\langle\psi_{\mathrm{p}}^{U_{\mathrm{k}}}|V_{\sigma}^{U_{\mathrm{k}}}|\psi_{\mathrm{p}}^{U_{\mathrm{k}}}\rangle = 0, \tag{7.3}$$

where $\psi_{\mathrm{p}}^{U_{\mathrm{k}}}$ is the wave function of the localized state and $d\epsilon_{\mathrm{p}}^{0}/dq$ the variation of the energy level with q as calculated with PBE. We remark that the second term on the right-hand side of Eq. (7.3) includes complex derivatives of the matrix elements $n_{mm'}^{I\sigma}$ with respect to q. Therefore, it is more practical to determine U_{k} by solving Eq. (7.2) by finite differences, namely by imposing that the energy levels calculated at integer charges $q = 0$ and $q = Q$ coincide ($Q = -1$ for localized electrons, $Q = +1$ for localized holes).

For a Hubbard parameter U, the formation energy of the polaronic defect state is calculated as [76]

$$E_{\mathrm{f}}^{U}(Q) = E^{U}(Q) - E_{\mathrm{ref}}^{U}(0) + Q\epsilon_{\mathrm{b}}^{U}, \tag{7.4}$$

where $E^{U}(Q)$ and $E_{\mathrm{ref}}^{U}(0)$ are the total energies of the defect state and of the reference bulk system, respectively, and $\epsilon_{\mathrm{b}}^{U}$ is the relevant band edge of the pristine system. In Eq. (7.4), the defect and reference systems contain the same atoms. We remark that finite-size electrostatic corrections due to the use of periodic boundary conditions need to be applied [77, 78, 86, 117]. For simplicity of notation, we consider all total energies, formation energies, and energy levels to be corrected by finite-size effects.

7.3 Results

As case studies, we consider self-trapped and impurity-trapped polaronic defects. In particular, we take the self-trapped electron in $BiVO_4$ [41], the self-trapped hole in MgO [39], the Li-trapped hole in MgO [223, 224], and the Al-trapped hole in

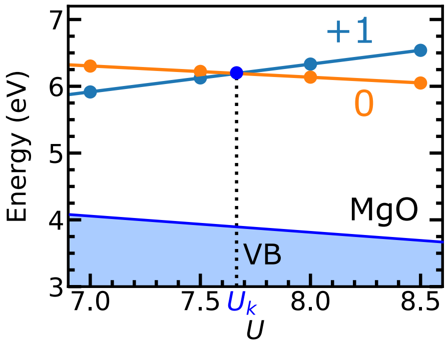

Figure 7.1 – Energy levels $\epsilon_{\mathrm{p}}^{U}(+1)$ and $\epsilon_{\mathrm{p}}^{U}(0)$ as a function of U for the self-trapped hole in MgO. The defect levels are identified by their respective charge. The value U_{k} is found such that $\epsilon_{\mathrm{p}}^{U_{\mathrm{k}}}(+1) = \epsilon_{\mathrm{p}}^{U_{\mathrm{k}}}(0)$.

α-SiO$_2$ [39, 57, 149–152]. The calculations are performed using the Quantum Espresso suite [153]. The computational set-up is the same given in Sec. 4.3.

We remark that, when using the PBE functional, such polaronic states are unstable. Thus, upon structural relaxation, the lattice distortions vanish and the defect charge delocalizes. In particular, self-trapped polarons delocalize over the entire system, and impurity-trapped holes distribute over the O atoms surrounding the impurity. At variance, for the polaronic defects under consideration, DFT+U can stabilize the localized states. We apply the U correction to the orbitals that constitute the localized states, namely the $3d$ orbitals of V atoms in BiVO$_4$, the $2p$ orbitals of O atoms in MgO, and the $2p$ orbitals of O atoms in α-SiO$_2$. In BiVO$_4$, the self-trapped electron localizes on a V atom. In MgO, the self-trapped hole localizes on a O atom. In Li-doped MgO, the hole localizes on a O atom neighboring the Li site. In α-SiO$_2$, the hole localizes on a O atom neighboring the Al site.

We determine the Hubbard parameter U_{k} through the enforcement of Eq. (7.2). We proceed as follows. We obtain the defect structure at various values of U by performing self-consistent structural relaxations. At such fixed structures, we calculate the energy levels $\epsilon_{\mathrm{p}}^{U}(Q)$ and $\epsilon_{\mathrm{p}}^{U}(0)$ accounting for finite-size effects. By imposing that $\epsilon_{\mathrm{p}}^{U_{\mathrm{k}}}(Q) = \epsilon_{\mathrm{p}}^{U_{\mathrm{k}}}(0)$, we then obtain $U_{\mathrm{k}} = 3.5$, 7.7, 7.5, and 8.3 eV for the self-trapped electron in BiVO$_4$, the self-trapped hole in MgO, the Li-trapped hole in MgO, and Al-trapped hole in α-SiO$_2$, respectively. This procedure is illustrated in Fig. 7.1 for the self-trapped hole in MgO. We remark that the values of U_{k} obtained for the self-trapped and the Li-trapped holes in MgO differ by only 0.2

eV, indicating that our scheme is robust upon varying the polaronic defect. This is analogous to the case of hybrid functionals, where one observes a weak dependence of α_k on the defect used for enforcing the piecewise linearity [40, 64–66]. In this context, we remark that finite-size corrections crucially affect the value of U_k. Indeed, without such corrections, we would have obtained $U_\mathrm{k}^\mathrm{uncor} = 1.7$, 4.9, 4.6, 5.1 eV for our respective case studies, with differences with respect to the corrected values amounting up to 3.2 eV. This emphasizes the importance of correcting for finite-size errors.

7.4 Band gaps and density of states

It is of interest to investigate the band gaps resulting from our selection of U. In Fig. 7.2, we show the evolution of the band gaps obtained with DFT+U as function of U and of the band gaps obtained with PBE0(α) as a function of α. In correspondence of U_k, DFT+U yields band gaps of 2.52, 6.67, and 8.82 eV for $\mathrm{BiVO_4}$, MgO, and α-$\mathrm{SiO_2}$, respectively. For MgO, we here use the value of U_k calculated for the self-trapped hole, considering the negligible difference with respect to the value for the Li-trapped hole. After the inclusion of appropriate corrections due to spin-orbit coupling, phonon renormalization, and exciton binding energies [142], the DFT+U_k band gaps are found to noticeably differ from their experimental counterparts (cf. Table 7.1). These discrepancies contrast with the case of hybrid functionals, for which the agreement with experiment is within 0.25 eV (cf. Table 7.1). The good performance of hybrid functionals derives from a global improvement of the electronic structure, in accord with numerous previous studies [40, 60, 64, 65, 67, 124, 148, 158]. From this analysis, we infer that an accurate description of band gaps should generally not be expected from DFT+U_k. We assign this to the fact that the U correction only applies to a subset of orbitals, which are not necessarily involved in both valence and conduction bands. Nevertheless, we expect that physical properties directly associated with the U-corrected orbitals should be properly described in DFT+U_k. For instance, in the case of polaronic defects, the formation energies express the relative stability of localized and delocalized states both being constituted by the same U-corrected orbitals.

Similar arguments apply when considering the effect of the Hubbard parameter U_k on the density of states. As test case, we take α-$\mathrm{SiO_2}$ and compare the density of states obtained with DFT+U_k with respect to experiment. As illustrated in Fig.

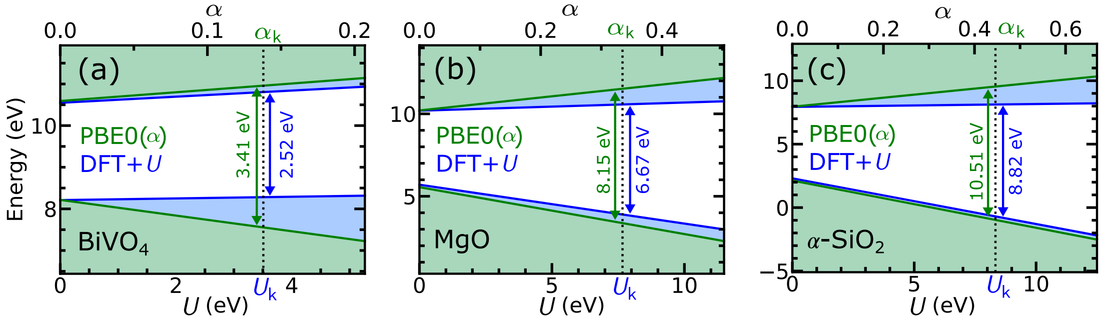

Figure 7.2 – Band edges as obtained with DFT+U and PBE0(α) as a function of U and α, respectively, for BiVO$_4$, MgO, and α-SiO$_2$. For MgO, we consider U_k and α_k calculated for the self-trapped hole. The vertical red line denotes the choice of the parameter for which the piecewise linearity condition is retrieved. The energy levels are aligned with respect to the average electrostatic potential [225].

Table 7.1 – Band gaps calculated with DFT+U_k ($E_\text{g}^{U_\text{k}}$) and PBE0(α_k) ($E_\text{g}^{\alpha_\text{k}}$) compared to reference experimental values after adding appropriate corrections (ΔE_g) taken from Ref. [142]. The reference experimental values correspond to the optical band gap at 300 K for BiVO$_4$ [159–161], the fundamental band gap at 6 K for MgO [163], and the first peak in the reflectance spectrum for α-SiO$_2$. In MgO, U_k is obtained from the self-trapped hole. Energies are in eV.

System	$E_\text{g}^{U_\text{k}}$	$E_\text{g}^{\alpha_\text{k}}$	ΔE_g	$E_\text{g,cor}^{U_\text{k}}$	$E_\text{g,cor}^{\alpha_\text{k}}$	Expt.
BiVO$_4$	2.52	3.41	-1.16	1.36	2.25	2.4-2.5
MgO	6.67	8.15	-0.53	6.14	7.62	7.77
α-SiO$_2$	8.82	10.51	0.02	8.84	10.53	10.30

7.3, DFT+U_k yields a valence band width of 8.1 eV, which is lower than both the corresponding PBE value of 9.3 eV and the experimental value of 11.0 eV [226]. This confirms the common finding that DFT+U narrows the band widths [227]. Hence, in analogy to our discussion on band gaps, DFT+U_k should not be expected to reproduce more global properties such as the density of states, even though the polaronic properties are reasonably well captured. This should be contrasted with the case of the hybrid functional PBE0(α_k), where the globally improved functional also yields an improved band width. Indeed, in the case of α-SiO$_2$, we find a PBE0(α_k) band width of 10.0 eV, improving upon the PBE value of 9.3 eV (cf. Fig. 7.3).

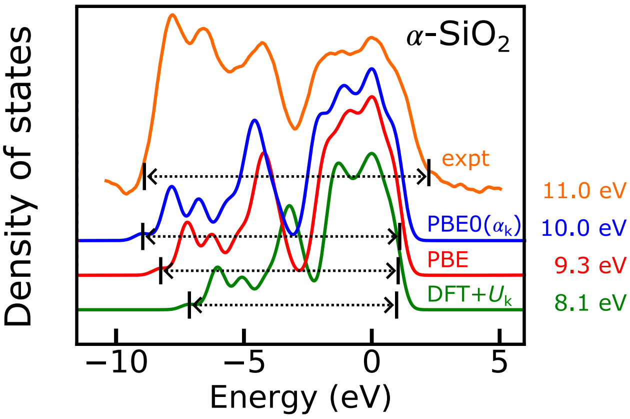

Figure 7.3 – Density of valence band states for α-SiO$_2$ as calculated with PBE0(α_k), PBE, and DFT+U_k, compared with the experimental XPS spectrum from Ref. [226]. The corresponding band widths are indicated. The theoretical band widths correspond to differences between Kohn-Sham levels, whereas the experimental band width is obtained from extrapolations of the wings. The curves are aligned with respect to the position of the highest energy peak.

7.5 Polaronic defects

We calculate electronic and structural properties of the polaronic defects studied in this work using the DFT+U_k functional and compare the results with those from PBE0(α_k) hybrid functionals. The hybrid functional results for the self-trapped polarons in BiVO$_4$ and MgO, and the Al-trapped hole in α-SiO$_2$ are taken from Chapter 4. For the Li-trapped hole in MgO, we obtain $\alpha_k = 0.33$, which is in good agreement with the value $\alpha_k = 0.34$ found for the self-trapped hole [141, 142]. The corresponding formation energy is -1.82 eV and is given in Table 7.3. As illustrated in Fig. 7.4, we find very good agreement between the defect densities calculated with the DFT+U_k and PBE0(α_k) functionals. Moreover, the lattice distortions practically coincide, with bond lengths deviating by at most 0.03 Å (cf. Table 7.2). Using Eq. (7.4), we calculate the respective formation energies $E_f^{U_k} = -0.49, -0.64, -2.01$, and -3.27 eV. These values are given in Table 7.3. Deviations from PBE0(α_k) results amount to at most 0.19 eV (cf. Table 7.3). This extends the robustness of piecewise-linear functionals to DFT+U schemes [141, 142], and concurrently validates our criterion for determining the value of U.

We further investigate the accuracy of the DFT+U_k energetics along a polaron hopping pathway. As test case, we consider the hopping of a hole polaron between two neighboring sites in MgO. We construct a 7-image migration pathway through

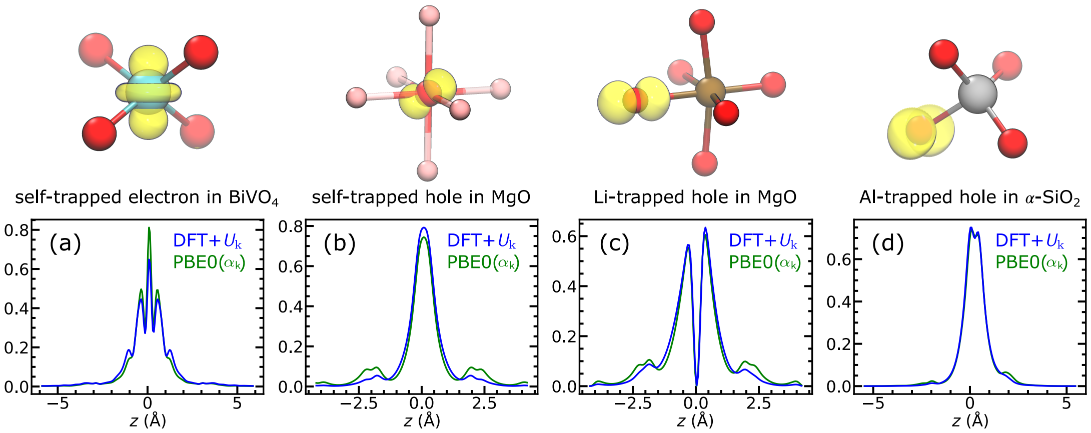

Figure 7.4 – Electron densities obtained with DFT+U_k and PBE0(α_k) functionals for the self-trapped electron in BiVO$_4$, the self-trapped hole in MgO, Li-trapped hole in MgO, and the Al-trapped hole in α-SiO$_2$. The defect density is integrated over xy-planes. On top, isodensity surfaces at 5% of their maximum (Bi in orange, V in cyan, O in red, Mg in pink, Li in brown, Si in blue, Al in grey).

Table 7.2 – Bond lengths (in Å) of the polaronic defect structures obtained with DFT+U_k and PBE0(α_k) functionals. For the Li-trapped hole in MgO, we give the lengths of the short/intermediate/long Li-O bonds. For the Al-trapped hole in α-SiO$_2$, we give the lengths of the short/long Al-O bonds.

Polaronic defect	DFT+U_k	PBE0(α_k)
BiVO$_4$ (self-trapped)	1.82	1.80
MgO (self-trapped)	2.22	2.20
MgO (Li-trapped)	1.92/2.17/2.30	1.90/2.17/2.33
α-SiO$_2$ (Al-trapped)	1.67/1.92	1.69/1.91

Table 7.3 – Hubbard parameter U_k obtained with the scheme introduced in this work compared with the parameter U_LR resulting from the linear-response method [68], together with the corresponding defect formation energies. For reference, we also give the formation energies $E_\mathrm{f}^{\alpha_\mathrm{k}}$ obtained with the piecewise linear PBE0(α_k) hybrid functional.

Polaronic defect	U_k	U_LR	$E_\mathrm{f}^{U_\mathrm{k}}$	$E_\mathrm{f}^{U_\mathrm{LR}}$	$E_\mathrm{f}^{\alpha_\mathrm{k}}$
BiVO$_4$ (self-trapped)	3.5	5.4	−0.49	−1.34	−0.63
MgO (self-trapped)	7.7	10.9	−0.64	−1.67	−0.53
MgO (Li-trapped)	7.5	10.9	−2.01	−3.09	−1.82
α-SiO$_2$ (Al-trapped)	8.3	10.1	−3.27	−4.00	−3.11

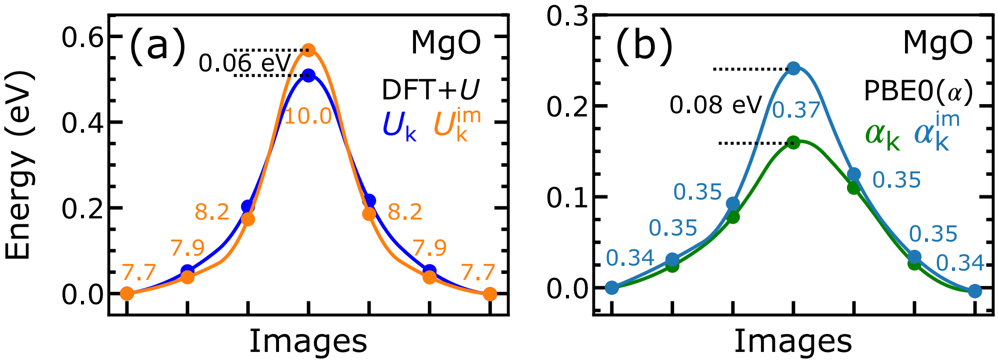

Figure 7.5 – Energy along a polaron pathway connecting two neighboring O atoms in MgO, as calculated (a) with fixed U_k and image-dependent U_k^im in DFT+U calculations, and (b) with fixed α_k and image-dependent $\alpha_\mathrm{k}^\mathrm{im}$ in PBE0(α) calculations. The values of U_k^im and $\alpha_\mathrm{k}^\mathrm{im}$ for individual images are given.

linear interpolation of the initial and final states. First, we evaluate the energy along the path using the determined value of U_k, as given in Fig. 7.5(a). Next, we determine U_k^im through the enforcement of the piecewise linearity for each image, finding the largest deviation with respect to U_k in correspondence of the transition state. This is due to the fact that at the transition state the polaron density is equally distributed among two neighboring O sites, thus deviating the most from the case of the hole polaron trapped at a single O site. Then, we calculate the energy along the pathway as $E^{U_\mathrm{k}^\mathrm{im}}[\text{polaron,im}] - E^{U_\mathrm{k}^\mathrm{im}}[\text{bulk}]$ for each image. As illustrated in Fig. 7.5(a), the difference between the energy barriers calculated with either fixed U_k or image-dependent U_k^im amounts to only 0.06 eV. This validates the choice of a fixed U_k for polaron hopping calculations. We carry out the same analysis with the PBE0(α) hybrid functional, finding a difference of 0.08 eV between the barriers calculated with either fixed α_k or image-dependent $\alpha_\mathrm{k}^\mathrm{im}$ [cf. Fig. 7.5(b)]. The energy barriers obtained with DFT+U_k and PBE0(α_k) differ by 0.32 eV, which is comparable with the typical accuracy achieved upon enforcing the piecewise linearity with different functionals (cf. Table 7.3 and Refs. [141, 142]).

7.6 Comparison with linear-response method

For comparison, we also determine U using the linear-response approach introduced by Cococcioni and de Gironcoli [68]. In this method, the parameter U is chosen to enforce the piecewise linearity in density-functional perturbation theory as given in Eq. (2.19). We calculate the Hubbard parameters using the code HP

[202]. We determine U_{LR} on neutral bulk structures using the PBE wave functions. We find $U_{\text{LR}} = 5.4, 10.9, 10.1$ eV for BiVO$_4$, MgO, and α-SiO$_2$, respectively. The resulting formation energies of the polaronic defects studied in this work are $E_{\text{f}}^{U_{\text{LR}}} = -1.34$, -1.67, 3.09, and -4.00 eV, as given in Table 7.3. We remark that U_{LR} is noticeably larger than U_{k} in all cases. Consequently, the respective formation energies calculated with U_{k} and U_{LR} differ by 0.85, 1.03, 1.08, and 0.73 eV. These large variations are in part due to the shift of the band edges upon variation of U (cf. Fig. 7.2), which enter in the definition of the formation energy in Eq. (7.4). To assess the dependence on the adopted configuration in the context of this comparison, we also use the linear-response approach on the very same polaron configuration used for the determination of U_{k} in the direct piecewise linear scheme. In this way, the same configurational set-up is used in the two approaches, thereby enabling a direct comparison. We take the U'_{LR} parameter resulting from the linear-response scheme for the atom where the polaron is localized. Focusing on the hole polaron in MgO, we find $U'_{\text{LR}} = 9.4$ eV, to be compared with the respective value $U_{\text{k}} = 7.7$ eV found through the direct application of the piecewise linearity condition. Thus, this analysis further confirms that the structural configuration is not at the origin of the differences between the two schemes for the determination of U. Additionally, we remark that our U_{k} is found for a Hubbard correction acting on all the atoms of the same species at the same time, whereas in the linear-response approach U_{LR} is found through a variation on a single atom. Hence, for an even closer comparison, we also determine the value U'_{k} by enforcing the piecewise linearity upon the application of U to the sole atom where the polaron localizes. In the case of the hole polaron in MgO, we find $U'_{\text{k}} = 8.5$ eV, which still differs sizably from $U'_{\text{LR}} = 9.4$ eV. This further confirms that the differences between the two methods are not only related to the computational setup.

The significant differences between U_{k} and U_{LR} call for a deeper investigation. Since both approaches are designed to enforce the piecewise linearity, we explicitly verify the extent by which the piecewise linearity is satisfied in the two schemes. This can be achieved by studying the total energy and the defect level as a function of q for the two choices of the parameter U. As illustrated in Fig. 7.6, U_{k} indeed yields a piecewise linear total energy and a constant defect level with respect to partial electron occupation. At variance, for U_{LR}, the total energy is convex with q, and the defect level is not constant. To understand these differences, we remark that the Hamiltonian in Eq. (2.16) used to determine U in the linear-response approach

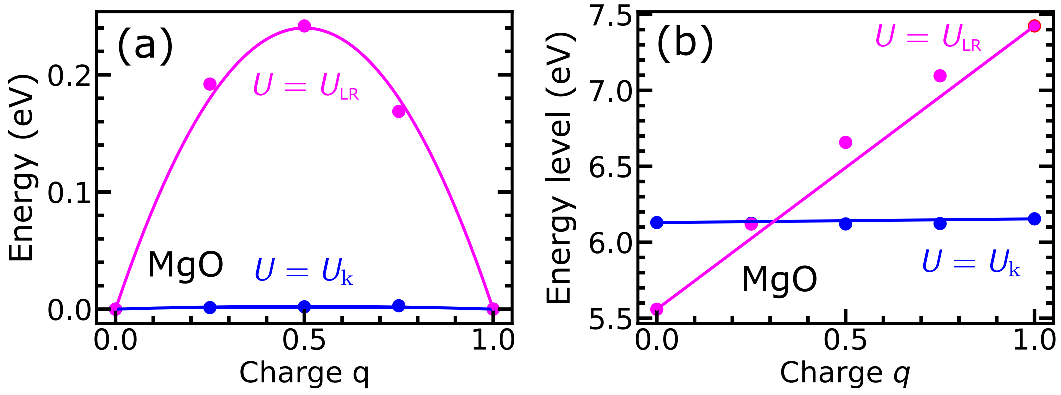

Figure 7.6 – (a) Deviation from the piecewise linearity of the total energy and (b) dependence of the defect level on the charge q, for the self-trapped hole in MgO. Results for U_{k} and U_{LR} are compared. The solid lines are a guide to the eye.

differs from the DFT+U Hamiltonian in Eq. (2.14). Thus, the U values that enforce the piecewise linearity in the two cases could be different. This would explain the departure from the piecewise linearity observed in Fig. 7.6 for DFT+U_{LR}. However, we remark that despite the different defect formation energies, the electron densities and the structural distortions of the polaronic defects obtained with U_{k} and U_{LR} practically coincide.

7.7 Discussion

In conclusion, we addressed the determination of the Hubbard U in the DFT+U functional through enforcing the piecewise linearity condition on polaronic defect states. Our selection of U yields electronic and structural properties of such defects in good agreement with results from hybrid functionals satisfying the same constraint. Our scheme is further validated by the excellent agreement found for formation energies obtained with piecewise-linear functionals. We emphasize that our approach targets physical properties related to the U-corrected orbitals, while more global properties, such as band gaps, are not directly involved. For comparison, we also calculate U through a widely-used linear-response method, finding values of U that break the piecewise linearity condition and give larger formation energies. To sum up, we showed that polaronic defect states can effectively be used for determining the value of the Hubbard U parameter in DFT+U. Additionally, we demonstrated that the resulting electronic, structural, and energetic properties of such defects closely correspond to those obtained with hybrid functionals, but at a noticeably lower computational cost.

8 Polaron hopping through piecewise-linear functionals

We use piecewise-linear functionals to study the polaron energy landscape and hopping rates in β-Ga_2O_3, which we adopt as an example of an anisotropic material hosting multiple polaronic states. We illustrate various functionals for polaron localization, including a hybrid functional and two types of semilocal functionals, and discuss how to ensure the piecewise linearity condition. Then, we determine the formation energies of stable polarons, and show that single-site and multi-site polaronic states can be found in close energetic competition. We perform nudged-elastic-band calculations to determine energy landscapes and hole transfer rates of all first-nearest-neighbor polaron hoppings. We show that when the piecewise linearity condition is ensured polaron properties are robust upon variation of the functional adopted, including formation energies, energy barriers, and charge transfer rates. This supports the use of semilocal functionals for calculating polaron transport properties.

This chapter is adapted from:
Ref. [228]: S. Falletta, A. Pasquarello, *Polaron hopping though piecewise-linear functionals*, in preparation.

8.1 Introduction

Polarons have a large impact on transport properties of materials and on related applications in photovoltaics [23]. From an experimental point of view, it has been shown that small polarons follow an Arrhenius-like behavior, which is characterized by a thermally activated carrier concentration and by an increasing mobility as a function of temperature [229]. From a theoretical point of view, most of the studies on polaron hopping are based on Marcus theory [90, 91] or on Emin-Holstein-Austin-Mott theory [92–94], which are equivalent for such hopping processes [99]. In these approaches, the initial and final polaron states are represented through independent Born-Oppenheimer surfaces, and a reaction pathway is defined to determine the transition state. The difference between the energies of the transition state and of the initial state gives the activation energy for the hopping process. Depending on the coupling between the initial and final states, two regimes are distinguished: for large coupling the regime is adiabatic, for small coupling the regime is diabatic [95]. Depending on the regime, different analytic expressions for the polaron hopping rate have been derived [95]. Such expressions can be incorporated within the Landau-Zener formula [96, 97], and have largely been applied to polaron hopping processes [46, 98–113]. The theoretical framework for studying polaron hopping is thus well defined. However, in such framework, the hopping rate depends exponentially on the activation energy, which hence needs to be accurately determined to yield reliable theoretical predictions.

The potential of piecewise-linear functionals in the determination of polaron properties can be systematically assessed when considering an anisotropic system, which can host multiple polaronic states. Indeed, the presence of various polaronic states allows for a multitude of polaron hopping pathways. This enables an extended comparison of polaron properties obtained with different piecewise-linear functionals. For this reason, as a test case, we consider monoclinic gallium oxide (β-$\mathrm{Ga_2O_3}$), a promising semiconductor for power electronics and optoelectronics due to its large band gap and large breakdown field [230–235]. In particular, it has been shown that β-$\mathrm{Ga_2O_3}$ can host both self-trapped holes [39, 60, 236–246] and impurity-trapped holes [246–258]. Hybrid functional and DFT+U calculations have shown that self-trapped holes can localize at differently-coordinated oxygen sites [39, 60, 236–246], due to the anisotropic structure of β-$\mathrm{Ga_2O_3}$. Paramagnetic resonance experiments suggest the existence of self-trapped holes at only one type of O site in β-Ga_2O_3 [250, 257]. Experimental results of self-trapped holes at other O sites are missing. Additionally, previous theoretical results may also not be accurate, due to the choice of the adopted functional. For these reasons, β-Ga_2O_3 represents a prototypical material for our study.

8.2 Stable polaronic states

We consider functionals that can address the many-body self-interaction of polarons, namely the hybrid functional PBE0(α) [53], the γDFT functional [141, 142], and the Hubbard-corrected DFT+U functional [68, 185–193]. All these functionals depend on a parameter, which we denote ξ. In particular, for the PBE0(α) functional, ξ corresponds to the fraction of Fock exchange α admixed to the semilocal exchange. For the γDFT functional, ξ is the strength γ of a weak local potential dependent on the polaron density. For the DFT+U functional, ξ is the Hubbard interaction U. In this notation, the polaron formation energy is written as

$$E_{\mathrm{f}}^{\xi}(q) = E^{\xi}(q) - E_{\mathrm{ref}}^{\xi}(0) + q\epsilon_{\mathrm{b}}^{\xi}, \tag{8.1}$$

where $E^{\xi}(q)$ is the total energy of the polaron system, $E_{\mathrm{ref}}^{\xi}(0)$ is the total energy of the reference pristine system, and $\epsilon_{\mathrm{b}}^{\xi}$ is the band level corresponding to the delocalized state. When the piecewise linearity is enforced, Eq. (8.1) becomes

$$E_{\mathrm{f}}^{\xi_{\mathrm{k}}}(q) = q(\epsilon_{\mathrm{b}}^{\xi_{\mathrm{k}}} - \epsilon_{\mathrm{p}}^{\xi_{\mathrm{k}}}) + [E^{\xi_{\mathrm{k}}}(0) - E_{\mathrm{ref}}^{\xi_{\mathrm{k}}}(0)]. \tag{8.2}$$

The calculations are performed using the Quantum Espresso suite [153]. The core-valence interactions are described by normconserving pseudopotentials [154]. We model β-Ga_2O_3 with a 120-atom monoclinic supercell ($a = 12.38$ Å, $b = 9.28$, $c = 11.76$ Å). The energy cutoff is set to 60 Ry. The lattice parameters are determined at the PBE level of theory for the pristine system. The Brillouin zone is sampled at the Γ point. Through the application of finite electric fields [87] at the PBE level of theory, we determine the high-frequency and static dielectric constants, $\epsilon_\infty = 3.75$ and $\epsilon_0 = 11.98$, which are used for the finite-size corrections [77, 117]. We remark that in β-Ga_2O_3 there are three differently-coordinated O atoms. As illustrated in Fig. 8.1(a), we denote O_{I} the oxygen atom shared by two GaO_6 octahedra and one GaO_4 tetrahedron, O_{II} the oxygen atom shared by one

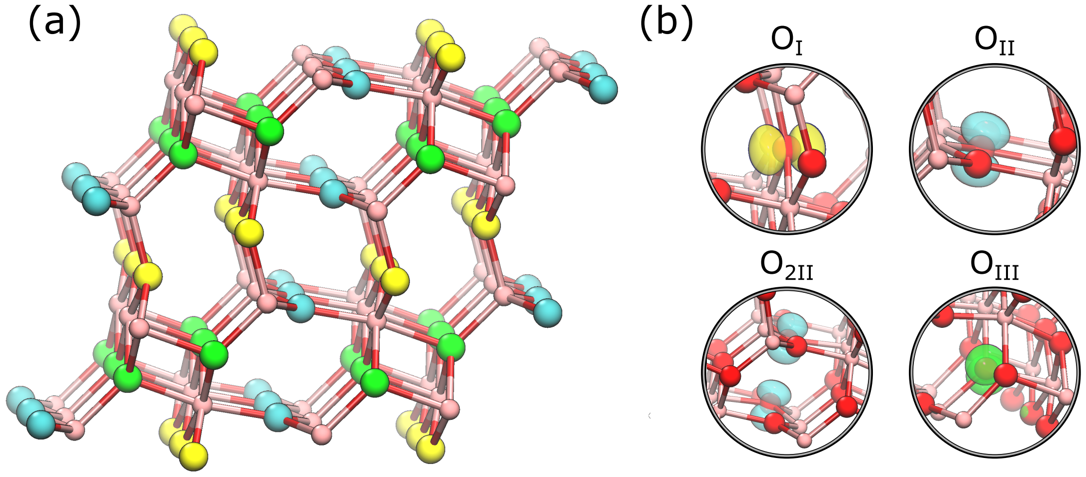

Figure 8.1 – (a) Bulk structure of β-Ga_2O_3 (O_{I} in yellow, O_{II} in cyan, O_{III} in green, Ga in pink). (b) Polaron isosurfaces at 5% of their maximum for the various hole polarons in β-Ga_2O_3 (Ga atoms in pink, O atoms in red).

GaO_6 octahedron and two GaO_4 tetrahedra, and O_{III} the oxygen atom coordinated with four oxygen atoms.

Using the hybrid functional PBE0(α), the enforcement of the piecewise linearity leads to hole polarons localized either at a single O_{I} site, at two neighboring O_{II} sites, which we denote $O_{2\mathrm{II}}$, or at a single O_{III} site. For these states, we find $\alpha_{\mathrm{k}} = 0.25$, 0.26, and 0.24. Considering that α_{k} is essentially independent of the polaronic defect, we set $\alpha_{\mathrm{k}} = 0.25$ and calculate the formation energies of the three polaron states, obtaining -0.63, -0.71, and -0.39 eV, respectively.

With the semilocal functional γDFT, the enforcement of the piecewise linearity yields hole polarons localized either at a single O_{I} site, at a single O_{II} site, or at a single O_{III} site, with respective $\gamma_{\mathrm{k}} = 1.37$, 1.45, and 1.40. Considering that γ_{k} is essentially independent of the polaronic defect, we take a fixed $\gamma_{\mathrm{k}} = 1.4$ and find respective formation energies of -0.59, -0.56, and -0.11 eV. To avoid resonances between the polaron level and the conduction band, the conduction band manifold has been shifted by a constant amount $\Delta = 3$ eV through the use of the self-consistent scissor operator introduced in Sec. 6.4.

In the DFT+U calculations, following Ref. [184], we apply the Hubbard U correction to the $2p$ orbitals of the O atoms, which constitute the localized polaron state. The enforcement of the piecewise linearity leads to polarons localized either at a single

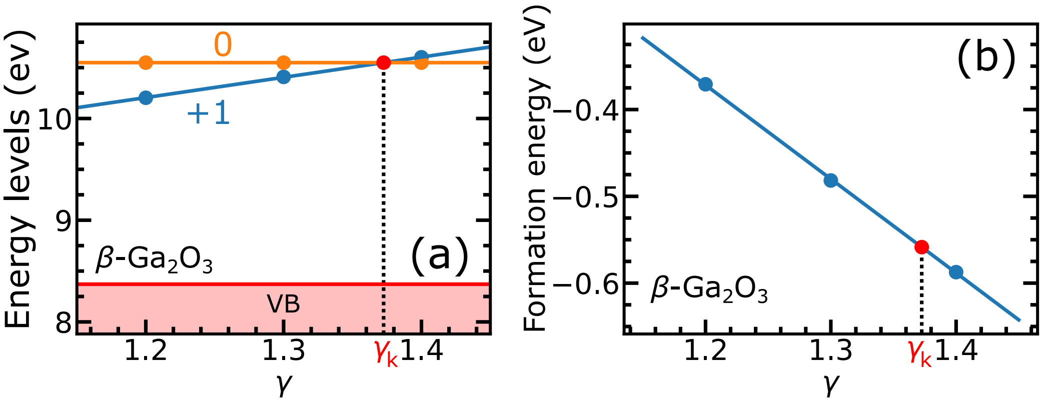

Figure 8.2 – (a) Energy levels and (b) formation energy obtained with γDFT as a function of γ for the hole polaron trapped at the O_I site in β-Ga$_2$O$_3$. In (a), the polaron levels are identified by their respective charge states.

Table 8.1 – Polaron formation energies obtained with piecewise-linear PBE0(α), γDFT, and DFT+U functionals. The formation energies of the metastable states are given in parentheses. Energies in eV.

	PBE0(α)	γDFT	DFT+U
O_I	−0.63	−0.59	−0.74
O_{II}	(−0.66)	−0.56	−0.54
O_{2II}	−0.71	(−0.25)	(−0.28)
O_{III}	−0.39	−0.11	−0.42

O_I site, at a single O_{II} site, or at a single O_{III} site, with respective $U_k = 4.7$, 5.1, and 4.9 eV. Considering that U_k is essentially independent of the polaronic defect, we take a fixed $U_k = 4.9$ eV and determine the respective formation energies of −0.74, −0.54, and −0.42 eV. We illustrate the various polaron states in Fig. 8.1(b) and give all the formation energies in Table 8.1.

We remark that polarons localized at single O_I and O_{III} sites are achieved with all piecewise-linear functionals. However, different descriptions are found for the polaronic state involving O_{II} sites. In particular, PBE0(α) stabilizes the double-site O_{2II} state, while γDFT and DFT+U stabilize the single-site O_{II} state. The localization of hole polarons at O_I and O_{2II} sites was already reported in previous studies [39, 60, 241, 244, 255, 257], while the localization of the hole polaron at a O_{III} site was only recently found in the work of Frodason *et al.* [244]. All

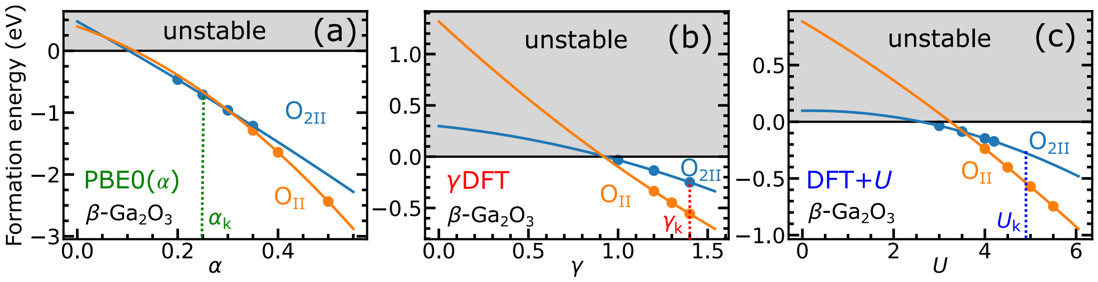

Figure 8.3 – Energy competition between the hole polarons localized either at the O_{II} site or at the O_{2II} site, as obtained with PBE0(α), γDFT, and DFT+U functionals.

such previous studies employ hybrid functionals, namely the PBE0 functional [39, 60, 241, 255, 257] and a range-separated hybrid functional [244]. The adopted fraction of Fock exchange α in these works ranges from 0.26 to 0.35 [39, 60, 241, 244, 255, 257]. For comparison, we consider the recent study of Frodason *et al.* [244], in which the O_I, O_{2II}, and O_{III} states are found. In particular, these authors calculated polaron formation energies of −0.48, −0.49, and −0.33 eV, respectively. These results systematically underestimate our PBE0(α) values in Table 8.1, while showing similar relative stability. However, a direct comparison with all such previous studies [39, 60, 241, 244, 255, 257] remains ambiguous, due to the disparity in the functional adopted and in the treatment of finite-size effects.

Our findings suggest that the hole polaron localized at the O_{II} site is in competition with the hole polaron localized over two O_{II} sites (O_{2II}). In particular, the piecewise-linear PBE0(α) functional stabilizes the O_{2II} state, while the piecewise-linear γDFT and DFT+U functionals stabilize the O_{II} state. Here, we determine the energy of the metastable state for each functional. In the PBE0(α) calculations, we find the structure of the O_{II} state using large values of α, for which the O_{II} state is more stable than the O_{2II} state. Then, we progressively optimize the structure by lowering α to approximately α_k. Similarly, in γDFT and DFT+U calculations, we find the structures of the O_{2II} state using low values of γ and U, which we subsequently increase until approaching γ_k and U_k, respectively. As illustrated in Fig. 8.3, we extrapolate the formation energies of these metastable states at α_k, γ_k, and U_k, and find that for the three functionals considered the energies of the competing O_{II} and O_{2II} states lie within 0.05, 0.31, and 0.26 eV, respectively. These values are comparable with the accuracy of piecewise-linear functionals in the determination of polaron formation energies (cf. Table 8.1). For comparison, we add to Table 8.1 the formation energies of these metatable states.

The competing $\mathrm{O_{II}}$ and $\mathrm{O_{2II}}$ states show very different polaron distributions [cf. Fig. 8.1(b)]. Hence, it is of interest to evaluate the parameter ξ'_{k} that enforces the piecewise linearity for the metastable polaronic states, namely the $\mathrm{O_{I}}$ state in PBE0(α), the $\mathrm{O_{2II}}$ state in γDFT, and the $\mathrm{O_{2II}}$ state in DFT+U. At fixed atomic structure, the enforcement of the piecewise linearity for such states gives $\alpha'_{\mathrm{k}} = 0.26$, $\gamma'_{\mathrm{k}} = 2.23$, and $U'_{\mathrm{k}} = 7.44$ eV. This shows that the values of α_{k} and α'_{k} obtained for the $\mathrm{O_{2II}}$ and $\mathrm{O_{II}}$ states pratically coincide, in accord with previous studies showing that α_{k} is essentially independent of the considered defect [40, 64–66, 184]. This is due to the fact that the hybrid functional PBE0(α) addresses the self-interaction on the entire electronic manifold. At variance, the values of γ'_{k} and U'_{k} obtained for the $\mathrm{O_{2II}}$ state vary from the values of γ_{k} and U_{k} obtained for the $\mathrm{O_{II}}$ state. This can be related to the fact that γDFT and DFT+U mainly address the self-interaction of the polaron state, and hence the values of γ_{k} and U_{k} are consequently affected by the polaron distribution. Additionally, we remark that γ'_{k} and U'_{k} are both larger than γ_{k} and U_{k}, respectively. Moreover, the $\mathrm{O_{II}}$ state becomes more stable than the $\mathrm{O_{2II}}$ state for sufficiently large values of γ and U [cf. Fig. 8.3]. This implies that self-consistent electronic and structural optimizations for the enforcement of the piecewise linearity using γDFT and DFT+U functionals yield the $\mathrm{O_{II}}$ state. This suggests that piecewise-linear functionals may have the tendency of favoring single-site localization over multi-site localization.

We now compare the properties of the stable polaronic states obtained with the various piecewise-linear functionals. As illustrated in Fig. 8.4, the polaron electron densities are practically independent of the adopted functional. An excellent agreement is also found for the polaronic lattice distortions, with deviations smaller than 0.05 Å (cf. Table 8.2), with the sole exception of the weak bonds for the $\mathrm{O_{III}}$ state for which a deviation of 0.10 Å is observed. Similarly, differences in the formation energies due to the choice of the functional are within 0.15 eV in all cases, except for the $\mathrm{O_{III}}$ state where we find a larger discrepancy of 0.31 eV (cf. Table 8.1). Overall, this analysis confirms the robustness of the polaron properties obtained with piecewise-linear functionals [141, 142, 184].

It is of interest to determine the accuracy by which γ_{k}, U_{k}, and α_{k} enforce the piecewise linearity condition. This can be achieved by taking the difference between the formation energies obtained with the expressions in Eqs. (8.2) and (8.1) at $\xi = \xi_{\mathrm{k}}$. Indeed, these two expressions are formally equivalent for all partial charge occupations q when the piecewise linearity condition is satisfied. We hence

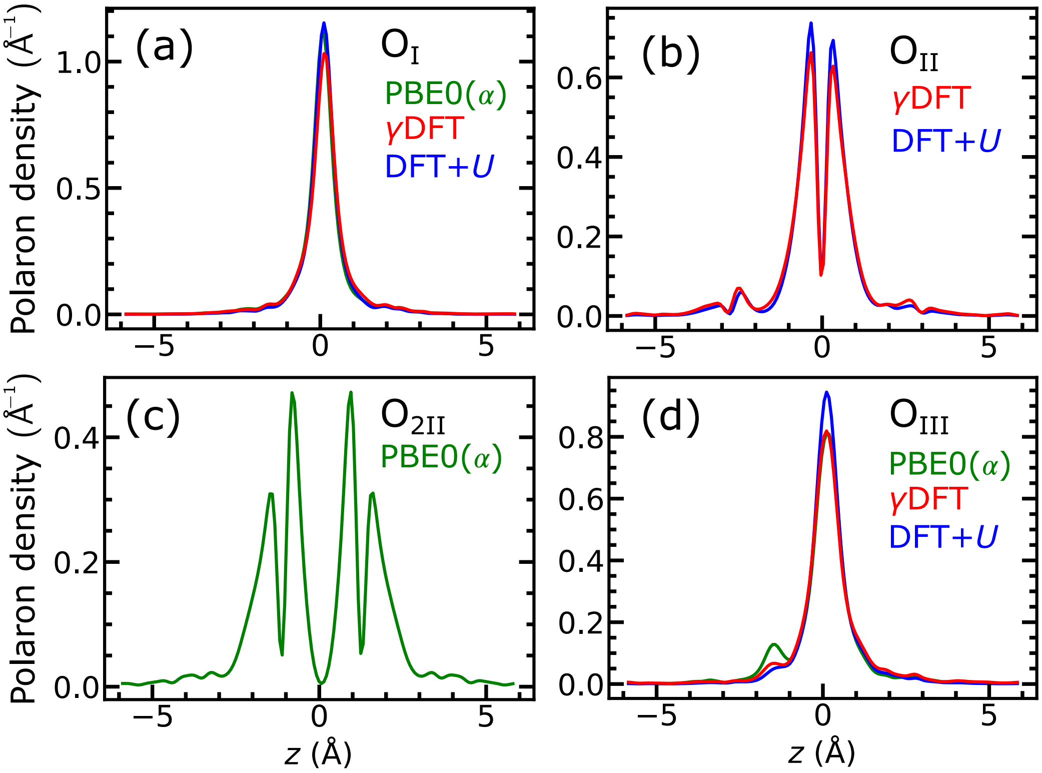

Figure 8.4 – Polaron densities integrated over xy planes obtained with piecewise-linear PBE0(α), γDFT, and DFT+U functionals for the hole polarons localized at the O_I, O_{II}, O_{2II}, and O_{III} sites.

Table 8.2 – Lengths of Ga-O polaronic bonds (in increasing order) obtained with piecewise-linear PBE0(α), γDFT, and DFT+U functionals. The bond lenghts of the less-stable states are given in parentheses. Bond lengths in Å.

	PBE0(α)	γDFT	DFT+U
O_I	1.97/2.17/2.17	2.02/2.16/2.16	1.98/2.20/2.20
O_{II}	(1.97/1.97/2.21)	2.02/2.02/2.18	1.99/1.99/2.22
O_{2II}	1.93/1.93/2.09	(1.94/1.94/2.06)	(1.93/1.93/2.08)
O_{III}	1.96/2.09/2.24/2.69	2.01/2.12/2.23/2.73	1.97/2.12/2.33/2.65

determine the quantity

$$\delta = \left|E^{\xi_k}(q) - [E^{\xi_k}(0) - q\epsilon_p^{\xi_k}]\right|, \tag{8.3}$$

and find for the stable polarons a mean average δ of 0.02, 0.06, and 0.02 eV using

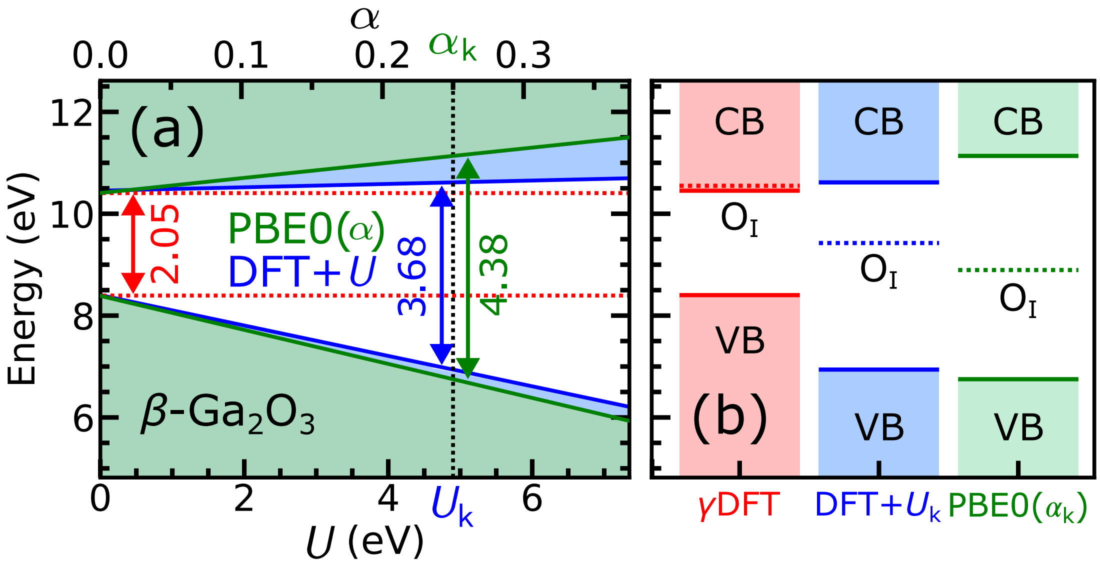

Figure 8.5 – (a) Band edges of β-Ga_2O_3 as obtained with PBE0(α) and DFT+U as a function of α and U, respectively. The vertical line denotes the choice of the parameter for which the piecewise linearity condition is retrieved. The energy levels are aligned with respect to the average electrostatic potential [225]. (b) Band gaps and energy levels of the hole polaron localized at the O_I site, as obtained with γDFT, DFT+U_k, and PBE0(α_k). The γDFT band gap coincides with that obtained with PBE. The polaron level calculated with γDFT is found by applying the scissor operator to the conduction band manifold (cf. Sec. 6.4).

γDFT, DFT+U, and PBE0(α) functionals, respectively. This agreement validates the parameters chosen to enforce the piecewise linearity condition.

We now highlight the role of the band gap in the determination of accurate polaron energetics. As illustrated in Fig. 8.5(a), we obtain band gaps of 4.38, 2.05, and 3.68 eV with PBE0(α_k), PBE, and DFT+U_k, respectively. The PBE0(α_k) band gap is in very good agreement with the range of experimental values 4.4−4.8 eV for β-Ga_2O_3 [259, 260]. This is in accord with previous findings showing the accuracy of band gaps obtained with piecewise-linear hybrid functionals with respect to the experiment [19, 40, 60–67, 141, 142]. At variance, both PBE and DFT+U_k noticeably underestimate the experimental band gap. Nevertheless, the incorrect description of the band gap in γDFT and DFT+U is not critical for the accurate determination of polaron properties [184]. Additionally, we remark that the energy level of the hole polaron localized on a O_I site calculated with the piecewise-linear γDFT functional is in resonance with the PBE conduction band. This demonstrates the necessity of including a self-consistent scissor operator in the γDFT Hamiltonian to avoid the delocalization of the polaron wave function (cf. Sec. 6.4).

8.3 Polaron hopping

We now study the minimal energy path for hopping of hole polarons in β-Ga_2O_3 by perfoming nudged-elastic-band calculations with piecewise-linear γDFT and DFT+U functionals. We avoid the use of the hybrid functional PBE0(α) for nudged-elastic-band calculations, which would require an excessively large amount of computational resources. We consider all the 21 first-nearest-neighbor hoppings, which are indexed in Table 8.3 by the pairs of O sites involved in the hopping and their respective distance. This requires performing 14 nudged-elastic-band calculations with each functional, since hoppings involving two different O sites provide information on both forward and backward transitions. In particular, for each nudged elastic band we take a 15-image path connecting the initial and final states. We use a fixed ξ_k instead of an image-dependent one, as this affects the activation energies in a minor fashion [184]. In this way, we determine the energy landscape as a function of the reaction coordinate Q.

For each transition, we determine the activation energy E_a as the difference between the transition-state energy and the ground-state energy of the initial state. For illustration, we show in Fig. 8.6 the hopping process between two O_I sites connected through a Ga atom. In this case, we find very good agreement

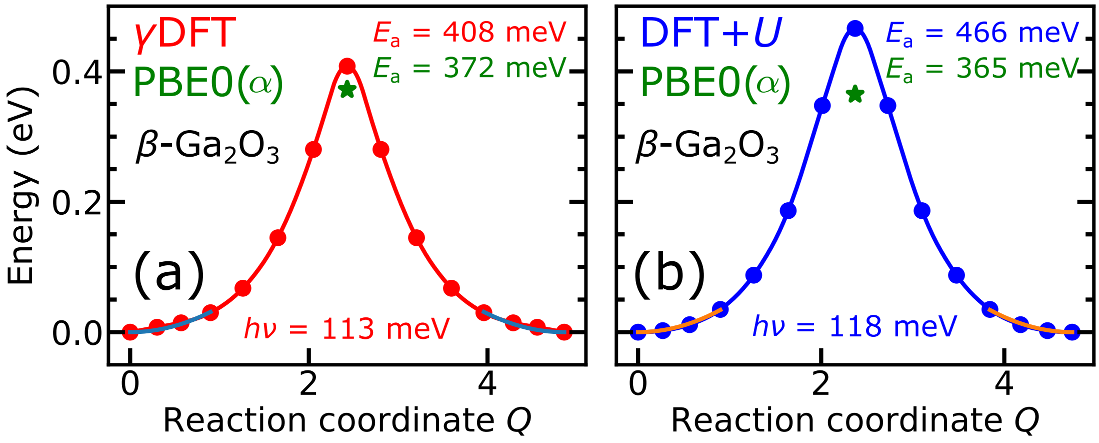

Figure 8.6 – Energy landscape of a polaron hopping between two neighboring O_I sites connected through a Ga atom in β-Ga_2O_3 (transition index #2 in Table 8.3), as obtained with piecewise-linear (a) γDFT and (b) DFT+U functionals through the nudged-elastic-band method. The activation energies E_a and the effective nuclear frequencies ν are indicated. In green, we give the activation energies calculated with the piecewise-linear functional PBE0(α) for the same nudged-elastic-band pathway.

between the activation energies obtained with piecewise-linear γDFT and DFT+U functionals. In particular, the activation energies in the two cases differ by only 58 meV. In Fig. 8.6, we also give the energy barriers calculated with the piecewise-linear PBE0(α) functional for the nudged-elastic-band pathways obtained with γDFT and DFT+U, finding a negligible difference of 7 meV between the two paths. This further corroborates the reliability of piecewise functionals and their mutual equivalence.

When considering all other hopping processes, we find overall a similar good agreement between the activation energies obtained with γDFT and DFT+U, as given in Table 8.1. In particular, the mean absolute error of activation energies amounts to only 85 meV [cf. Fig. 8.7(a)]. The largest variations are observed for the transitions $\mathrm{O}_{\mathrm{III}} \rightarrow \mathrm{O}_{\mathrm{II}}$ (indexes #18 and #19), which can be related to the discrepancy in the energy difference between final and initial states involved in the nudged-elastic-band calculation (cf. Table 8.1). This can be related to the Bell-Evans-Polanyi principle, which establishes a linear relationship between the activation energy and the energy difference between final and initial states [261, 262].

Then, we focus on the determination of the hole transfer rates for all transitions. First, we calculate the effective nuclear frequency ν through quadratic interpolation of the energy profile around the initial state, as shown in Fig. 8.6. Then, we determine the couplings J for all transitions as half the separation between occupied and unoccupied defect energy levels at the transition state [116], as illustrated in Fig. 8.8. Given the activation energies E_{a}, the effective nuclear frequencies ν, and the couplings J, we calculate the probabilities P defined in Eq. (2.45) at $T = 300$ K. We find that $P = 1$ in all cases, with the exception of the transition #18 calculated with DFT+U for which $P = 0.9$. This indicates that essentially all the transitions are adiabatic. We then calculate the hole transfer rates at $T = 300$ K for all hopping processes using Eq. (2.42). The effective nuclear frequencies ν, the couplings J, and the rates k_{t} obtained for all the hoppings are given in Table 8.3.

As shown in Fig. 8.7(b), we also find good agreement for the hole transfer rates calculated with γDFT and DFT+U, characterized by a mean value of $|\log_{10}(k_{\mathrm{t}}^{\gamma_{\mathrm{k}}}/k_{\mathrm{t}}^{U_{\mathrm{k}}})|$ equal to 1.5, which represents the mean absolute error on the order of magnitude of k_{t}. This is quite satisfactory considering that even small variations of the activation energy can affect the hole transfer rate by several orders of magnitude due to

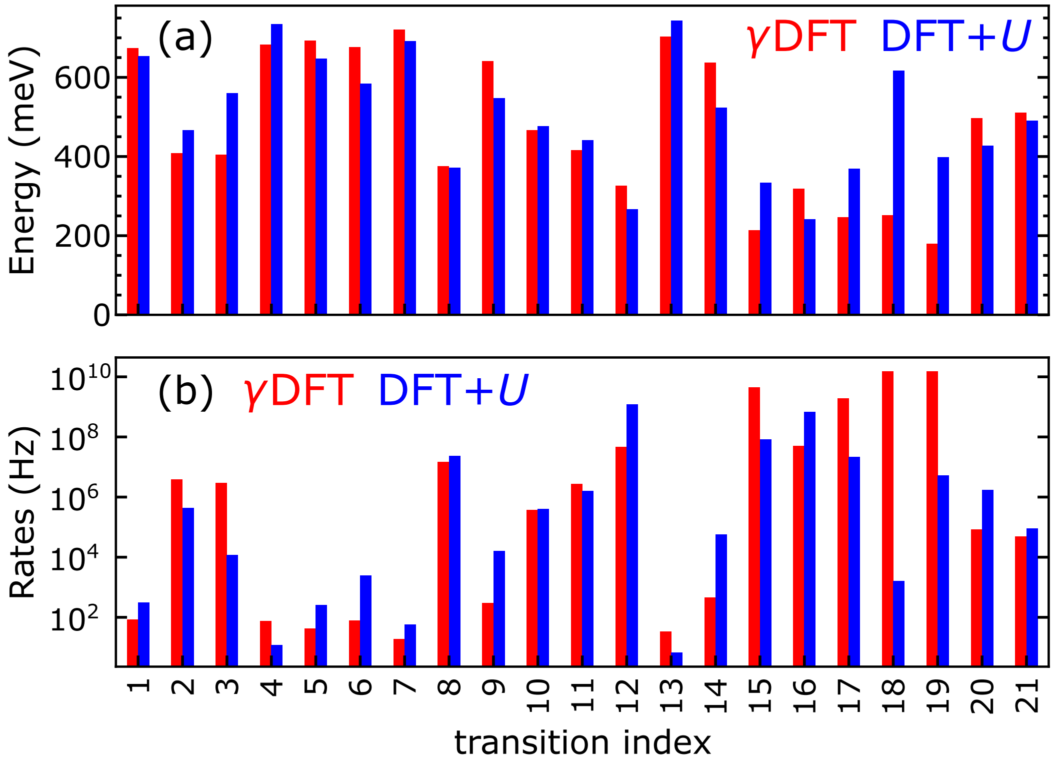

Figure 8.7 – (a) Activation energies and (b) hole transfer rates at 300 K for the hole polaron hoppings in β-Ga$_2$O$_3$ listed in Table 8.3.

the exponential dependence of the transfer rate on the activation energy [cf. Eq. (2.42)]. This analysis sets the overall accuracy of piecewise-linear functionals in the determination of electron-transfer rates, and shows that the robustness of the polaron properties obtained with piecewise-linear functionals also holds for activation energies and hopping rates.

We remark that some of the activation barriers in Table 8.3 are higher than the formation energies of the initial state. In such a case, the transition state is less stable than the delocalized state in which the polaron charge delocalizes uniformily over the entire system and the polaronic lattice distortions vanish. This indicates that the hole polaron diffusion in β-Ga$_2$O$_3$ cannot be uniquely described by polaron hopping, and that more complex scattering mechanisms combining polaron hopping and polaron delocalization should be considered in the calculation of polaron mobilities.

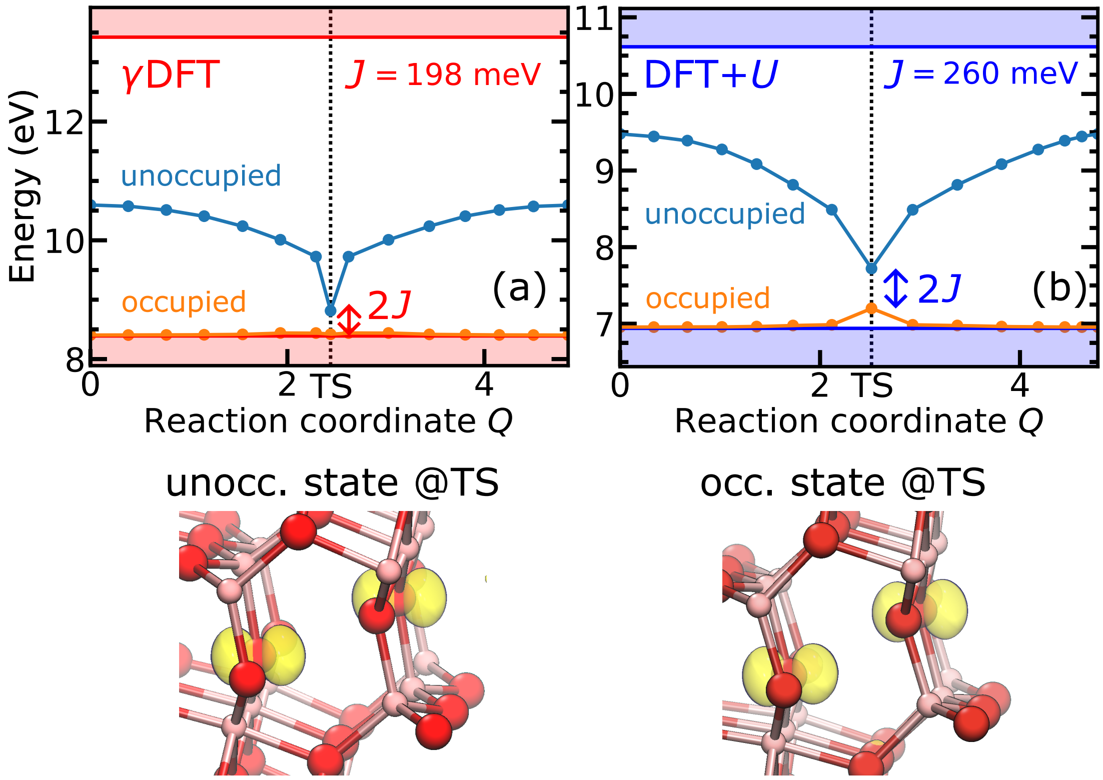

Figure 8.8 – Occupied and unoccupied defect energy levels as a function of the reaction coordinate for a polaron hopping between two neighboring O_I sites in β-Ga_2O_3 (transition index #1 in Table 8.3), as obtained with piecewise-linear (a) γDFT and (b) DFT+U functionals. Defect energy levels are corrected by finite-size effects. Below, isodensity surfaces at 5% of their maximum for the densities of the occupied and unoccupied defect states at the transition state, as calculated with γDFT.

8.4 Discussion

In conclusion, we investigated the use of piecewise-linear functionals for the determination of polaronic ground-state and transport properties. We showed that enforcing the piecewise linearity condition leads to robust polaron properties upon variation of the functional. Considered properties include electron densities, lattice bonds, formation energies, activation energies, and transfer rates. Such a robustness validates the accuracy and the reliability of the calculated polaron properties. This is particularly relevant when considering formation energies, which are subject to large variations upon varying the parameters of the functionals.

By consequence, our work demonstrates that semilocal functionals yield essentially

Table 8.3 – Distance d^{ξ_k} between hopping sites (in Å), activation energy $E_a^{\xi_k}$ (in meV), phonon frequencies $h\nu_n^{\xi_k}$ (in meV), and hole-transfer rate $k_T^{\xi_k}$ (in Hz) at 300 K for all first-nearest-neighbor polaron hoppings in β-Ga$_2$O$_3$, as obtained with piecewise-linear γDFT and DFT+U functionals.

		γDFT					DFT+U				
Hopping	index	d	E_a	$h\nu$	J	k_t	d	E_a	$h\nu$	J	k_t
$O_I \to O_I$	1	3.16	674	74	198	8.4×10^1	3.28	653	119	260	3.1×10^2
	2	3.09	408	113	647	3.8×10^6	3.09	466	118	696	4.3×10^5
$O_I \to O_{II}$	3	2.88	404	77	607	3.0×10^6	2.83	560	124	676	1.2×10^4
	4	2.98	673	45	171	7.6×10^1	2.94	734	106	302	1.2×10^1
$O_I \to O_{III}$	5	2.65	693	74	602	4.2×10^1	2.67	647	82	680	2.6×10^2
	6	2.88	677	77	645	7.9×10^1	2.90	554	271	790	3.2×10^4
	7	3.24	720	99	564	1.9×10^1	3.23	692	97	623	5.7×10^1
$O_{II} \to O_I$	8	2.88	375	123	607	1.5×10^7	2.83	372	168	676	2.3×10^7
	9	2.98	642	136	171	5.4×10^2	2.94	547	174	302	2.7×10^4
$O_{II} \to O_{II}$	10	3.04	467	106	344	3.7×10^5	3.06	477	168	350	4.0×10^5
	11	3.09	416	109	443	2.7×10^6	3.09	441	164	490	1.6×10^6
	12	2.84	326	59	547	4.7×10^7	2.82	267	146	725	1.2×10^9
$O_{II} \to O_{III}$	13	2.94	703	90	479	3.3×10^1	2.96	744	86	144	6.7×10^0
	14	2.99	637	96	589	4.6×10^2	2.98	524	147	567	5.7×10^4
$O_{III} \to O_I$	15	2.65	214	73	602	4.5×10^9	2.67	334	140	680	8.4×10^7
	16	2.88	205	129	645	1.1×10^{10}	2.90	241	31	790	6.7×10^8
	17	3.24	246	106	564	1.9×10^9	3.23	369	146	623	2.2×10^7
$O_{III} \to O_{II}$	18	2.94	251	76	479	1.1×10^9	2.96	617	165	144	1.6×10^3
	19	2.99	179	61	589	1.5×10^{10}	2.98	398	103	567	5.2×10^6
$O_{III} \to O_{III}$	20	2.69	497	77	428	8.3×10^4	2.70	427	106	610	1.7×10^6
	21	3.09	511	76	349	4.9×10^4	3.09	491	65	489	9.0×10^4

the same polaron properties, thereby supporting their use for exploring polaronic energy landscapes and for determining polaron transport properties. This becomes important when considering anisotropic materials, which can be characterized by numerous polaronic hopping pathways for which hybrid-functional calculations would be computationally beyond reach.

In summary, our work provides a paradigm shift for the study of polaron transport properties, through the use of piecewise-linear functionals as opposed to standard functionals. This also lends justification to the use of efficient semilocal functionals, thus paving the way to accurate and systematic studies of polaronic transport properties from first principles.

9 Conclusion

In this thesis, we investigated the concept of many-body self-interaction in relation to polarons in density functional theory, thereby enabling the use of semilocal functionals for modelling polarons in a computationally-efficient way.

First, we developed a method for correcting energies and single-particle levels of defects involving frozen lattice distortions, which is necessary for modelling isolated polarons when using supercells. We highlighted the role of the ionic polarization charge in the determination of such corrections. We showed that our scheme yields accurate corrections through extrapolation to the limit of an infinitely large supercell for various defects. As a further validation, we demonstrated that our corrections for vertical transition energies satisfy a sum rule connecting them to state-of-the-art corrections for structurally relaxed defects.

Then, we addressed the self-interaction of polarons using hybrid functionals. We showed that the many-body self-interaction can be suppressed by selecting the fraction of Fock exchange admixed to semilocal exchange such that the polaron energy level is independent of its occupation. This yields a piecewise-linear energy with respect to electron occupation, thereby recovering a property of the exact energy functional. Then, we determined the electronic and structural properties of polarons, including the formation energy. We emphasized that hybrid functionals lead to an overall improvement of the electronic structure, including band gaps.

Within the family of hybrid functionals, by which both forms of self-interaction can be addressed, we developed an analytical formulation for both many-body and one-body descriptions of the self-interaction and showed that they are related through the dielectric constant. In particular, we demonstrated that correcting for the many-body self-interaction accounts for additional electron screening effects, which are missing when addressing the one-body self-interaction. Additionally, we found that these two forms of self-interaction coincide in the absence of electron screening. Hence, through this analysis, we demonstrated the superiority of the many-body form of self-interaction over the one-body form of self-interaction.

Given the preeminence of the many-body self-interaction, we then introduced an efficient methodology to obtain localized polarons free from many-body self-interaction at the semilocal level of theory. The charge localization is achieved by adding a weak local potential to the semilocal Hamiltonian. Possible resonances involving the polaron state and the delocalized band states are addressed by including to the Hamiltonian a scissor operator, which is constructed with the self-consistent wave functions. This approach yields polarons with charge densities, atomic structures, and formation energies in close agreement to those obtained with piecewise-linear hybrid functionals but at the computational cost of a semilocal calculation. This shows that electronic and structural properties of polarons free from many-body self-interaction are robust upon variation of the functional adopted.

Taking advantage of our findings, we introduced a selection criterion for the Hubbard parameter U in Hubbard-corrected density functional theory based on suppressing the many-body self-interaction of polaronic defect states. The resulting polaron properties are in good agrement with results from piecewise-linear hybrid functionals, thereby further corroborating the robustness of polaron properties obtained with functionals free from many-body self-interaction. The resulting energetics is accurate also for polaron hoppings, whereby the use of configurational-dependent U values can be avoided. In this approach, the selection of U is based on physical properties that are directly associated with the orbitals to which U is applied, without involving more global properties, such as band gaps and density of states.

Finally, we applied piecewise-linear functionals to study the ground-state and transport properties of polarons in an anisotropic system, which can host multiple polaronic states. We studied the energy landscape pertaining to all first-nearest-neighbor polaron hoppings with semilocal functionals, and therefrom calculated the corresponding polaron transfer rates. We demonstrated that the robustness of the polaron properties obtained with piecewise-linear functionals also extends to hopping energy landscapes and transition rates. This further supports the use of semilocal functionals for efficient calculations of polarons.

In conclusion, we introduced a theoretical formulation for the electron self-interaction that solves the problem of polaron localization in density functional theory. This leads to significant developments to the long-standing problem of self-interaction, from both the conceptual and the methodological point of view. From the conceptual point of view, we demonstrated that polaron calculations should account for the many-body self-interaction rather than for the one-body self-interaction to include all relevant screening effects. As a result, the polaron properties obtained with piecewise-linear functionals are found to be robust upon variation of the functional. From the methodological point of view, we introduced a semilocal scheme for polaron localization and a selection criterion for Hubbard-corrected functionals, which both address the many-body self-interaction. This gives access to accurate polaron stabilities through computationally-efficient schemes, thus carring several advantages. First, our methodology enables the study of polarons in large systems, which are often inaccessible at the hybrid functional level of theory, especially for plane-wave-based codes. Moreover, our scheme allows for systematic studies of polarons involving large sets of materials, thus opening up the possibility to perform high-throughput studies of polarons. Additionally, our approach enables the accurate modelling of polarons in liquid phases in molecular dynamics evolving over long time periods, which can be used for calculating polaron mobilities. Finally, our method allows for the exploration of polaronic energy landscapes and for the calculation of polaron transfer rates. To summarize, our study paves the way to unprecedented calculations of polarons for various applications, opening up new horizons in polaron physics.

A Appendix: Scissor operator for opening the band gap

We present a method for opening the band gap in semilocal density functional theory through the use of a self-consistent scissor operator, which acts separately on the valence and conduction manifolds. The shifts partaining to valence and conduction bands are chosen in order to reproduce the band levels obtained with a reference hybrid functional. We demonstrate that this methodology allows one to obtain accurate electronic and atomic properties of bulk systems when compared to reference hybrid functional calculations, but at a significantly lower computational cost. As test cases, we consider Ge, GaN, and GaAs.

A.1 Introduction

One of the most notorious shortcomings of density functional theory due to the electron self-interaction is the band gap problem [85, 263], which consists of incorrectly predicting the energy gap between the valence and conduction band manifold. This is critical when modelling semiconductors, since it affects their optical and photovoltaics properties. Several schemes have been proposed to address the band gap problem. The state-of-the-art method for predicting band gaps is the *GW* approximation [264], which gives very accurate results with respect to experiment [122, 265]. At a lower computational cost, hybrid functionals have been successfully applied to predict band gaps, with an accuracy comparable to that of *GW* calculations [172]. However, hybrid functionals are still computationally very expensive for large systems in high-throughput screening of materials. Another method for the band-gap problem consists in using the DFT+U functional, which has a computational cost comparable to semilocal density functional theory. However, the band edges are not guaranteed to accurately reproduce those obtained with state-of-the-art *GW* calculations. Other attempts to solve the band gap problem involve the use of an *a-posteriori* scissor operator [266–271], which however is not suitable for defect levels close to the band edges [271]. Other strategies consist in using cluster models [272], or in sampling the Brillouin zone at a single off-centered point [273]. In this context, it is of interest to develop a computationally-advantageous scheme to open the band gap at the semilocal level of theory.

A.2 Methodology

Taking advantage of our developments in Sec. 6.4, we include a scissor operator to the semilocal Hamiltonian and solve the following set of Kohn-Sham equations

$$(\mathcal{H}_\sigma^0 + \mathcal{S}_\sigma)\psi_{i\sigma}^s = \epsilon_{i\sigma}^s \psi_{i\sigma}^s, \tag{A.1}$$

where $\mathcal{H}_\sigma^0$ is the semilocal PBE Hamiltonian [10], $\mathcal{S}_\sigma$ the scissor operator acting on the spin channel σ, $\psi_{i\sigma}^s$ are the wave functions, and $\epsilon_{i\sigma}^s$ the corresponding eigenvalues. We define the scissor operator $\mathcal{S}_\sigma$ as

$$\mathcal{S}_\sigma = \Delta_\mathrm{v} \sum_{j\in\mathcal{M}_\sigma^\mathrm{v}} |\psi_{j\sigma}^s\rangle\langle\psi_{j\sigma}^s| + \Delta_\mathrm{c} \sum_{j\in\mathcal{M}_\sigma^\mathrm{c}} |\psi_{j\sigma}^s\rangle\langle\psi_{j\sigma}^s|\,, \tag{A.2}$$

where $\mathcal{M}_\sigma^{\mathrm{v}}$ and $\mathcal{M}_\sigma^{\mathrm{c}}$ denote the manifolds of valence and conduction band states, respectively, and Δ_{v} and Δ_{c} are the corresponding energy shifts. The $\psi_{j\sigma}^s$ in Eq. (A.2) are the self-consistent wave functions obtained in the optimization of the Kohn-Sham equations. The expression in Eq. (A.2) has the effect of shifting the energy levels pertaining to the valence (conduction) band manifold by Δ_{v} (Δ_{c}). Indeed, due to the orthonormality of the wave functions, $\mathcal{S}_\sigma$ applied to a wave function $\psi_{i\sigma}$ yields

$$\mathcal{S}_\sigma \left|\psi_{i\sigma}^s\right\rangle = \begin{cases} \Delta_{\mathrm{v}} \left|\psi_{i\sigma}^s\right\rangle, & \text{if } i\sigma \in \mathcal{M}_\sigma^{\mathrm{v}} \\ \Delta_{\mathrm{c}} \left|\psi_{i\sigma}^s\right\rangle, & \text{if } i\sigma \in \mathcal{M}_\sigma^{\mathrm{c}} \end{cases}. \tag{A.3}$$

Generally, one takes $\Delta_{\mathrm{v}} < 0$ and $\Delta_{\mathrm{c}} > 0$, in order to reproduce the opening of the band gap as obtained in hybrid functional calculations. The total energy corresponding to Eq. (A.1) is given by

$$E^s = E^0 + \Delta E^s, \tag{A.4}$$

where the energy contribution ΔE^s is a constant shift given by

$$\Delta E^s = N\Delta_{\mathrm{v}}, \tag{A.5}$$

where N is the number of electrons in the system. We denote this scheme PBE+$\mathcal{S}$.

A.3 Results

We perform the calculations using the QUANTUM ESPRESSO suite of codes. As case studies, we consider germanium (Ge), gallium nitride (GaN), and gallium arsenide (GaAs). We model Ge with a 64-atom cubic supercell ($a = 11.32$ Å), wurtzite GaN with a 96 atom orthorombic supercell ($a = 9.57$ Å, $b = 11.05$ Å, $c = 10.37$ Å), GaAs with a 64-atom cubic supercell ($a = 11.30$ Å). The lattice parameters are fixed to the experimental values [274–276]. The Brillouin zone is sampled with a 2×2×2 grid and the energy cutoff is set to 80 Ry in all cases.

As reference, we consider the band edges obtained with the hybrid functional PBE0(α_{g}), where α_{g} is the fraction of Fock exchange that reproduces the experimental band gap. Then, by comparing the bands levels obtained with PBE and PBE0(α_{g}), we determine the energy shifts Δ_{v} and Δ_{c} for each material, as given in

Table A.1 – Experimental band gap $E_\mathrm{g}^\mathrm{exp}$, fraction α_g of Fock exchange that reproduces $E_\mathrm{g}^\mathrm{exp}$, and shifts Δ_v and Δ_c in Ge, GaN, and GaAs. Energies in eV.

System	$E_\mathrm{g}^\mathrm{exp}$	α_g	Δ_v	Δ_c
Ge	0.74	0.13	−0.46	0.26
GaN	3.50^I	0.22	−0.94	0.62
GaAs	1.52^II	0.17	−0.63	0.36

$^\mathrm{I}$ Ref. [277], $^\mathrm{II}$ Ref. [278].

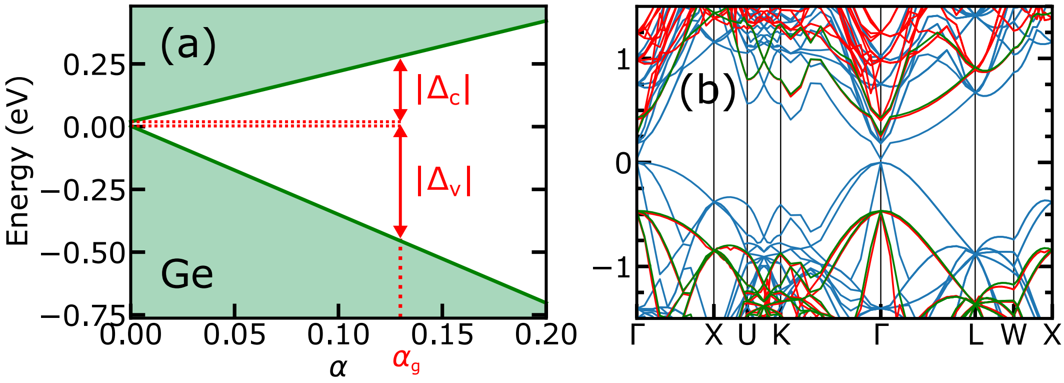

Figure A.1 – (a) Band edges of Ge as a function of the fraction α of Fock exchange in PBE0(α) calculations. The fraction α_g of Fock exchange is chosen to reproduce the experimental band gap. (b) Electronic bands of Ge as obtained with the semilocal functional PBE (in blue), with the hybrid functional PBE0(α_g) (in green), and with the functional PBE+$\mathcal{S}$ (in red).

Table A.1. This procedure is illustrated in Fig. A.1(a) in the case of Ge. This case study is particularly interesting since a regular semilocal density functional such as PBE would predict a vanishing band gap. At variance, in PBE0(α) calculations, the band gap can be opened to reproduce the experimental result.

Next, we determine the accuracy of the electronic and atomic structure for the various functionals considered in this work. In regards to the electronic structure, we calculate the electronic bands along a **k**-point path determined with SeeK-Path [279]. We find that the valence and conduction bands obtained with PBE+$\mathcal{S}$ are very similar to the PBE electronic bands but shifted by the amounts Δ_v and Δ_c, respectively, as illustrated in Fig. A.1(b) for Ge. To assess the accuracy of the atomic structure, we calculate the equibrium lattice parameter a_0 of the unit cell and the bulk modulus B_0. This is done by calculating the total energy versus supercell size and by using a Murnaghan fit [280]. We find that the PBE and

Table A.2 – Equilibrium lattice parameter a_0 of the unit cell and bulk modulus B_0 obtained with PBE, PBE+$\mathcal{S}$, and PBE0(α_g) functionals in comparison with the experimental values. The lattice parameters are in Å, the bulk moduli are in GPa. The mean percentage errors δ with respect to the experimental values are given.

	PBE		PBE/PBE+$\mathcal{S}$		PBE0(α_g)		Expt.	
System	a_0	B_0	a_0	B_0	a_0	B_0		
Ge	5.76	56.6	5.76	56.6	5.67	67.5	5.66[a]	74.9[b]
GaN	3.22	171.2	3.22	171.2	3.17	199.0	3.19[c]	207.0[d]
GaAs	5.74	59.2	5.74	59.2	5.64	73.6	5.65[e]	75.4[f]
δ	1.4%	21.1%	1.4%	21.1%	0.2%	5.4%	–	–

PBE+$\mathcal{S}$ results practically coincide and result in mean percentage errors of 1.4% and 21.1% with respect to experiment for a_0 and B_0, respectively. The hybrid functional PBE0(α_g) improves this result with mean percentage errors with respect to the experiment of 0.2% and 5.4% for a_0 and B_0, respectively. Overall, this confirms the validity of our PBE+$\mathcal{S}$ method in relation to the electronic and atomic structure.

A.4 Discussion

We introduced a method for opening the band gap based on adding a scissor operator to the semilocal Hamiltonian. The scissor operator is constructed as a sum of projectors, which are defined using the wave functions calculated in the self-consistent optimization of the Kohn-Sham equations. The resulting electronic and atomic properties of bulk systems are in good agreement with reference results obtained with hybrid functionals.

B Appendix: Code implementation in Quantum Espresso

We discuss the implementation of the γDFT scheme and of the self-consistent scissor operator in QUANTUM ESPRESSO. In γDFT, we enhance the data structure pertaining to electron densities by including the polaron distribution in real and reciprocal space. At each step of the self-consistency, the polaron density is calculated and mixed with results at previous steps using the same subroutines as for the total electron density. The semilocal potential in γDFT is then constructed and added to the total Hamiltonian. For the scissor operator, we construct the projectors using the self-consistent wave functions and then the scissor operator to the Hamiltonian. Relevant implementation details for achieving fast convergence are discussed.

B.1 Implementation of the γDFT scheme

We discuss the implementation details of the γDFT scheme in the code PW of QUANTUM ESPRESSO. The implementation follows the workflow illustrated in Fig. B.1. In particular, the polaron density is calculated and mixed analogously to the total electron density. Similarly, the γDFT potential is evaluated together with the exchange-correlation potential. In the following, we show that the implementation requires minimal changes to existing data structures and subroutines. We discuss in detail the files that are modified for including the γDFT scheme.

In order to perform a γDFT calculation, we introduce the following input variables in the `&SYSTEM` namecard of the PW input file:

```
&SYSTEM
...
   sic_gamma  = 1.40
   sic_energy = .true.
   pol_type   = 'h'
\
```

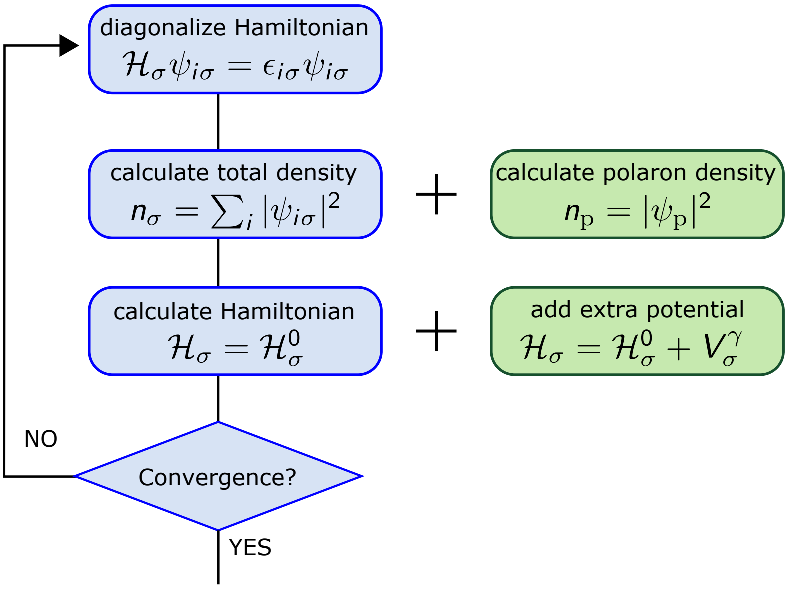
diagonalize Hamiltonian
$\mathcal{H}_\sigma \psi_{i\sigma} = \epsilon_{i\sigma}\psi_{i\sigma}$
calculate total density
$n_\sigma = \sum_i |\psi_{i\sigma}|^2$
+
calculate polaron density
$n_\mathrm{p} = |\psi_\mathrm{p}|^2$
calculate Hamiltonian
$\mathcal{H}_\sigma = \mathcal{H}^0_\sigma$
+
add extra potential
$\mathcal{H}_\sigma = \mathcal{H}^0_\sigma + V^\gamma_\sigma$
NO
Convergence?
YES

Figure B.1 – Implementation workflow of the γDFT scheme. In blue the existing subroutines, in green the subroutines related to the γDFT scheme.

where `sic_gamma` is a real number representing the strength γ of the localized potential, `sic_energy` a logical variable enabling the calculation of the energy ΔE^{γ}, and `pol_type` a string specifying the type of polaron (`'e'` for electron polarons, `'h'` for hole polarons). These input parameters are inlcuded through proper modification of the files `Modules/input_parameters.f90`, `Modules/control_flags.f90`, `Modules/read_namelists.f90`, and `PW/src/input.f90`.

As illustrated in Fig. B.1, one needs to construct the polaron density. The electron density is stored in the data structure `scf_type`, which is used to represent densities or potentials in a 3D grid in the real and in the reciprocal spaces, as defined in the file `PW/src/scf_mod.f90`. Here, we enhance the `scf_type` structure by introducing two equivalent features that represent the polaron density in real and reciprocal space, namely

```
TYPE scf_type
   REAL(DP), ALLOCATABLE :: of_r(:,:)
   COMPLEX(DP), ALLOCATABLE :: of_g(:,:)
   ...
   REAL(DP), ALLOCATABLE :: pol_r(:,:):
   COMPLEX(DP), ALLOCATABLE :: pol_g(:,:)
END TYPE scf_type
```

where `pol_r` and `pol_g` refer to the representation of the polaron density in real and reciprocal spaces, respectively. This is analogous to the features `of_r` and `of_g` used for the total density. Consequently, all subroutines involving the data structure `scf_type` in the file `scf_mod.f90` are modified accordingly, including all operations devoted to the mixing of the electron density. In this way, the mixing of the polaron density is achieved consistently with the mixing of the total electron density. The electron density is determined through subroutines in the file `sum_band.f90`, where the densities of all orbitals are summed up. Similarly, in `sum_band.f90` we construct the polaron density using the same subroutines but taking only the last occupied wave function in the spin up channel for electron polarons, or the first unoccupied wave function in the spin down channel for hole polarons.

For the calculation of the potential V_{σ}^{γ}, we introduce a new module named `sic_mod` in the file `PW/src/sic.90`, which makes use of existing exchange-correlation subroutines. In particular, the total electron density is stored in the variable `rho`. Then, following Eqs. (6.15) and (6.16), we construct an auxiliary density `rho_aux`, which is equal to `rho` minus (plus) the density of the electron (hole) polaron in the spin up (down) channel. Next, the potential V_σ^γ is constructed as follows

```
CALL v_xc(rho,      rho_core, rhog_core, etxc_aux, vtxc_aux, vxc)
CALL v_xc(rho_aux,  rho_core, rhog_core, etxc_aux, vtxc_aux, vxc_aux)
v%of_r(:,:) = v%of_r(:,:) + sic_gamma*(vxc(:,:) - vxc_aux(:,:))
```

where `v_xc` is the subroutine that calculates the exchange-correlation potential, `vxc` and `vxc_aux` are the exchange-correlation potentials pertaining to `rho` and `rho_aux`, and `v%of_r` is the Kohn-Sham potential in real space. In addition, the module `sic_mod` handles the allocation and deallocation of all quantities related with the γDFT calculation. The inclusion of the potential is incorporated in the calculation of the Kohn-Sham potential, as performed in the file `PW/src/v_of_rho.f90`. At the first step of the self-consistency, the potential V_σ^γ is initialized to zero, as given in the file `PW/src/potinit.f90`. The extrapolation of the polaron density in consecutive relaxation calculation is done in the file `PW/src/update_pot.f90`.

The calculation of the energy ΔE^γ, which is defined in the file `PW/src/pwcom.f90`, is enabled when setting the input variable `sic_energy = .true.`. Following Eq. (6.9), this requires carrying out two independent calculations at polaron charges $q = 0$ and $q = Q$ ($Q = -1$ for electron polarons, $Q = +1$ for hole polarons). The subroutines for performing these two consecutive calculations are inserted in the files `PW/src/sic.f90`, `PW/src/setup.f90`, and `PW/src/electrons.f90`. At the end of the calculation with $q = 0$, the total electron density is stored in the variable `rho_n` of the module `sic_mod`, and all buffers and other variables pertaining to the neutral calculations are initialized to zero in the files `PW/src/clean_pw.f90` and `PW/src/electrons.f90`. The charged calculation is then performed and the energy ΔE^γ is evaluated at each step of the self-consistency in the file `PW/src/sic.f90`.

In order to guarantee robust convergence in structural relaxations, molecular dynamics calculations, or nudged elastic band calculations, it might be convenient to initialize the density of the system from a superposition of atomic orbitals at each restart. This is achieved by including the input variable `pol_reset` in the `&SYSTEM` namecard. The presence of this input variable requires modification of the files `Modules/input_parameters.f90`, `Modules/control_flags.f90`, `Modules/read_namelists.f90`, and `PW/src/input.f90`. The reset of the wave functions is performed in the file `PW/src/electrons.f90`.

B.2 Implementation of the scissor operator

We now focus on the implementation of the self-consistent scissor operator in the code PW of QUANTUM ESPRESSO. In particular, we introduce two additional variables in the `&SYSTEM` namecard of the PW input file, namely

```
&SYSTEM
...
   sci_vb = -1.0
   sci_cb = +1.0
\
```

where `sci_vb` and `sci_cb` are real numbers corresponding to the shift of the valence and conduction bands, respectively. These input parameters are included through the modification of the files `Modules/input_parameters.f90`, `Modules/control_flags.f90`, `Modules/read_namelists.f90`, and `PW/src/input.f90`.

For the calculation of the scissor operator $\mathcal{S}_\sigma$, we introduce a new module named `sci_mod` in the file `PW/src/scissor.90`. In particular, $\mathcal{S}_\sigma$ is constructed with the wave functions $\phi_{i\sigma}$ in input to the diagonalization of the Hamiltonian $\mathcal{H}_\sigma$ at each step of the self-consistent cycle, as given in the file `PW/src/c_bands.f90`. The wave functions are selected from either valence or conduction manifolds. In polaron calculations, the manifold of valence electrons is identified as the set of occupied wave functions excluding the electron polaron state. Similarly, the manifold of conduction electrons is identified as the set of unoccupied wave functions excluding the hole polaron state. Then, for given wave functions $\psi_{i\sigma}$, we calculate directly the application of the scissor operator to the wave functions, namely

$$\mathcal{S}_\sigma \left|\psi_{i\sigma}\right\rangle = \Delta \sum_{i\in\mathcal{M}_\sigma} \left\langle\phi_{i\sigma}|\psi_{i\sigma}\right\rangle \left|\phi_{i\sigma}\right\rangle , \tag{B.1}$$

where $\phi_{i\sigma}$ are the wave functions used for constructing the scissor operator, and $\phi_{i\sigma}$ are the wave functions to which the scissor operator applies to. The evaluation of $\mathcal{S}_\sigma \left|\psi_{i\sigma}\right\rangle$ requires the evaluation of the overlaps $\left\langle\phi_{i\sigma}|\psi_{i\sigma}\right\rangle$ and is performed in the file

`PW/src/scissor.90`. This is then added to $\mathcal{H}_\sigma \left|\psi_{i\sigma}\right\rangle$ in the file `h_psi.f90`. The corresponding energy is then included through variables in the files `PW/src/pwcom.f90` and `PW/src/electrons.f90`. The scissor operators for the valence and conduction bands are decoupled and are activated through the keywords `sci_vb` and `sci_cb`, respectively.

Bibliography

(1) Dirac, P. A. M. *Proc. R. Soc. Lond.* **1929**, *123*, 714–733.

(2) Kohn, W. *Rev. Mod. Phys.* **1999**, *71*, 1253–1266.

(3) Thomas, L. H. **1927**, *23*, 542–548.

(4) Fermi, E **1927**, *6*, 602–607.

(5) Fermi, E; Amaldi, E **1934**, *6*, 119.

(6) Hartree, D. R. *Proc. Cambridge Philos. Soc.* **1928**, *24*, 89–110.

(7) Fock, V. *Z. Phys.* **1930**, *61*, 126–148.

(8) Hohenberg, P.; Kohn, W. *Phys. Rev.* **1964**, *136*, B864–B871.

(9) Kohn, W.; Sham, L. J. *Phys. Rev.* **1965**, *140*, A1133–A1138.

(10) Perdew, J. P.; Burke, K.; Ernzerhof, M. *Phys. Rev. Lett.* **1996**, *77*, 3865–3868.

(11) Perdew, J. P.; Parr, R. G.; Levy, M.; Balduz, J. L. *Phys. Rev. Lett.* **1982**, *49*, 1691–1694.

(12) Ruzsinszky, A.; Perdew, J. P.; Csonka, G. I.; Vydrov, O. A.; Scuseria, G. E. *J. Chem. Phys.* **2007**, *126*, 104102.

(13) Zhang, Y.; Yang, W. *J. Chem. Phys.* **1998**, *109*, 2604–2608.

(14) Yang, W.; Zhang, Y.; Ayers, P. W. *Phys. Rev. Lett.* **2000**, *84*, 5172–5175.

(15) Schmidt, T.; Kümmel, S. *Phys. Rev. B* **2016**, *93*, 165120.

(16) Mori-Sánchez, P.; Cohen, A. J.; Yang, W. *J. Chem. Phys.* **2006**, *125*, 201102.

(17) Lany, S.; Zunger, A. *Phys. Rev. B* **2009**, *80*, 085202.

(18) Ruzsinszky, A.; Perdew, J. P.; Csonka, G. I.; Vydrov, O. A.; Scuseria, G. E. *J. Chem. Phys.* **2006**, *125*, 194112.

(19) Kronik, L.; Kümmel, S. *Phys. Chem. Chem. Phys.* **2020**, *22*, 16467–16481.

(20) Atalla, V.; Zhang, I. Y.; Hofmann, O. T.; Ren, X.; Rinke, P.; Scheffler, M. *Phys. Rev. B* **2016**, *94*, 035140.

(21) Körzdörfer, T.; Kümmel, S.; Mundt, M. *J. Chem. Phys.* **2008**, *129*, 014110.

(22) Chevy, F. *Physics* **2016**, *9*, 86.

(23) Franchini, C.; Reticcioli, M.; Setvin, M.; Diebold, U. *Nat. Rev. Mater* **2021**, *6*, 560–586.

(24) Landau, L. D. *Phys. Z. Sowjetunion* **1933**, *3*, 664.

(25) Pekar, S. I. *Zh. Eksp. Teor. Fiz* **1946**, *16*, 341.

(26) Landau, L. D.; Pekar, S. I. *Zh. Eksp. Teor. Fiz* **1948**, *18*, 419–423.

(27) Fröhlich, H.; Pelzer, H.; Zienau, S. *Lond. Edinb. Dubl. Philos. Mag. J. Sci.* **1950**, *41*, 221–242.

(28) Holstein, T. *Ann. Phys.* **1959**, *8*, 325–342.

(29) Lee, T. D.; Low, F. E.; Pines, D. *Phys. Rev.* **1953**, *90*, 297–302.

(30) Fröhlich, H. *Adv. Phys.* **1954**, *3*, 325–361.

(31) Feynman, R. P. *Phys. Rev.* **1955**, *97*, 660–665.

(32) Gross, E. P. *Phys. Rev.* **1955**, *100*, 1571–1578.

(33) Marshall, J. T.; Mills, L. R. *Phys. Rev. B* **1970**, *2*, 3143–3146.

(34) Luttinger, J. M.; Lu, C.-Y. *Phys. Rev. B* **1980**, *21*, 4251–4263.

(35) Kholodenko, A. L.; Freed, K. F. *Phys. Rev. B* **1983**, *27*, 4586–4600.

(36) Prokof'ev, N. V.; Svistunov, B. V. *Phys. Rev. Lett.* **1998**, *81*, 2514–2517.

(37) Titantah, J. T.; Pierleoni, C.; Ciuchi, S. *Phys. Rev. Lett.* **2001**, *87*, 206406.

(38) Grusdt, F. *Phys. Rev. B* **2016**, *93*, 144302.

(39) Varley, J. B.; Janotti, A.; Franchini, C.; Van de Walle, C. G. *Phys. Rev. B* **2012**, *85*, 081109.

(40) Miceli, G.; Chen, W.; Reshetnyak, I.; Pasquarello, A. *Phys. Rev. B* **2018**, *97*, 121112.

(41) Wiktor, J.; Ambrosio, F.; Pasquarello, A. *ACS Energy Lett.* **2018**, *3*, 1693–1697.

(42) Wiktor, J.; Pasquarello, A. *ACS Appl. Mater. Interfaces* **2019**, *11*, 18423–18426.

(43) Österbacka, N.; Erhart, P.; Falletta, S.; Pasquarello, A.; Wiktor, J. *Chem. Mater.* **2020**, *32*, 8393–8400.

(44) Du, M.-H.; Zhang, S. B. *Phys. Rev. B* **2009**, *80*, 115217.

(45) Deák, P.; Aradi, B.; Frauenheim, T. *Phys. Rev. B* **2011**, *83*, 155207.

(46) Spreafico, C.; VandeVondele, J. *Phys. Chem. Chem. Phys.* **2014**, *16*, 26144–26152.

(47) Lany, S. *Phys. Status Solidi B* **2011**, *248*, 1052–1060.

(48) Kokott, S.; Levchenko, S. V.; Rinke, P.; Scheffler, M. *New J. Phys.* **2018**, *20*, 033023.

(49) Sio, W. H.; Verdi, C.; Poncé, S.; Giustino, F. *Phys. Rev. Lett.* **2019**, *122*, 246403.

(50) Sio, W. H.; Verdi, C.; Poncé, S.; Giustino, F. *Phys. Rev. B* **2019**, *99*, 235139.

(51) Lee, N.-E.; Chen, H.-Y.; Zhou, J.-J.; Bernardi, M. *Phys. Rev. Mater.* **2021**, *5*, 063805.

(52) Luo, Y.; Chang, B. K.; Bernardi, M. *Phys. Rev. B* **2022**, *105*, 155132.

(53) Perdew, J. P.; Ernzerhof, M.; Burke, K. *J. Chem. Phys.* **1996**, *105*, 9982–9985.

(54) Chen, W.; Pasquarello, A. *Phys. Rev. B* **2017**, *96*, 020101.

(55) Perdew, J. P.; Zunger, A. *Phys. Rev. B* **1981**, *23*, 5048–5079.

(56) Borghi, G.; Park, C.-H.; Nguyen, N. L.; Ferretti, A.; Marzari, N. *Phys. Rev. B* **2015**, *91*, 155112.

(57) d'Avezac, M.; Calandra, M.; Mauri, F. *Phys. Rev. B* **2005**, *71*, 205210.

(58) VandeVondele, J.; Sprik, M. *Phys. Chem. Chem. Phys.* **2005**, *7*, 1363–1367.

(59) Cohen, A. J.; Mori-Sánchez, P.; Yang, W. *Science* **2008**, *321*, 792–794.

(60) Deák, P.; Duy Ho, Q.; Seemann, F.; Aradi, B.; Lorke, M.; Frauenheim, T. *Phys. Rev. B* **2017**, *95*, 075208.

(61) Sadigh, B.; Erhart, P.; Åberg, D. *Phys. Rev. B* **2015**, *92*, 075202.

(62) Sai, N.; Barbara, P. F.; Leung, K. *Phys. Rev. Lett.* **2011**, *106*, 226403.

(63) Refaely-Abramson, S.; Sharifzadeh, S.; Jain, M.; Baer, R.; Neaton, J. B.; Kronik, L. *Phys. Rev. B* **2013**, *88*, 081204.

(64) Bischoff, T.; Wiktor, J.; Chen, W.; Pasquarello, A. *Phys. Rev. Mater.* **2019**, *3*, 123802.

(65) Bischoff, T.; Reshetnyak, I.; Pasquarello, A. *Phys. Rev. B* **2019**, *99*, 201114.

(66) Bischoff, T.; Reshetnyak, I.; Pasquarello, A. *Phys. Rev. Research* **2021**, *3*, 023182.

(67) Yang, J.; Falletta, S.; Pasquarello, A. *J. Phys. Chem. Lett.* **2022**, *13*, 3066–3071.

(68) Cococcioni, M.; de Gironcoli, S. *Phys. Rev. B* **2005**, *71*, 035105.

(69) Dabo, I.; Ferretti, A.; Poilvert, N.; Li, Y.; Marzari, N.; Cococcioni, M. *Phys. Rev. B* **2010**, *82*, 115121.

(70) Nguyen, N. L.; Colonna, N.; Ferretti, A.; Marzari, N. *Phys. Rev. X* **2018**, *8*, 021051.

(71) Borghi, G.; Ferretti, A.; Nguyen, N. L.; Dabo, I.; Marzari, N. *Phys. Rev. B* **2014**, *90*, 075135.

(72) Oliver, G. L.; Perdew, J. P. *Phys. Rev. A* **1979**, *20*, 397–403.

(73) Himmetoglu, B.; Floris, A.; de Gironcoli, S.; Cococcioni, M. *Int. J. Quantum Chem.* **2014**, *114*, 14–49.

(74) Pulay, P. *Mol. Phys.* **1969**, *17*, 197–204.

(75) Janak, J. F. *Phys. Rev. B* **1978**, *18*, 7165–7168.

(76) Freysoldt, C.; Grabowski, B.; Hickel, T.; Neugebauer, J.; Kresse, G.; Janotti, A.; Van de Walle, C. G. *Rev. Mod. Phys.* **2014**, *86*, 253–305.

(77) Freysoldt, C.; Neugebauer, J.; Van de Walle, C. G. *Phys. Rev. Lett.* **2009**, *102*, 016402.

(78) Komsa, H.-P.; Rantala, T. T.; Pasquarello, A. *Phys. Rev. B* **2012**, *86*, 045112.

(79) Castleton, C. W. M.; Höglund, A.; Mirbt, S. *Phys. Rev. B* **2006**, *73*, 035215.

(80) Hine, N. D. M.; Frensch, K.; Foulkes, W. M. C.; Finnis, M. W. *Phys. Rev. B* **2009**, *79*, 024112.

(81) Taylor, S. E.; Bruneval, F. *Phys. Rev. B* **2011**, *84*, 075155.

(82) Castleton, C. W. M.; Mirbt, S. *Phys. Rev. B* **2004**, *70*, 195202.

(83) Leslie, M; Gillan, N. J. *J. Phys. C* **1985**, *18*, 973–982.

(84) Makov, G.; Payne, M. C. *Phys. Rev. B* **1995**, *51*, 4014–4022.

(85) Lany, S.; Zunger, A. *Phys. Rev. B* **2008**, *78*, 235104.

(86) Freysoldt, C.; Neugebauer, J.; Van de Walle, C. G. *Phys. Status Solidi B* **2011**, *248*, 1067–1076.

(87) Umari, P.; Pasquarello, A. *Phys. Rev. Lett.* **2002**, *89*, 157602.

(88) Jónsson, H.; Mills, G.; Jacobsen, K. W. In *Classical and Quantum Dynamics in Condensed Phase Simulations*, pp 385–404.

(89) Henkelman, G.; Uberuaga, B. P.; Jónsson, H. *J. Chem. Phys.* **2000**, *113*, 9901–9904.

(90) Marcus, R. A. *Angew. Chem.* **1993**, *32*, 1111–1121.

(91) Marcus, R. A. *Ann. Rev. Phys. Chem.* **1964**, *15*, 155–196.

(92) Emin, D.; Holstein, T *Ann. Phys.* **1969**, *53*, 439–520.

(93) Holstein, T. *Ann. Phys.* **2000**, *281*, 725–773.

(94) Austin, I.; Mott, N. *Adv. Phys.* **1969**, *18*, 41–102.

(95) Böttger, H.; Bryksin, V. V. In *Hopping Conduction in Solids*; Akademie-Verlag, Berlin: 1985.

(96) Landau, L. *Phys. Z. Sowjetunion* **1932**, *2*, 118.

(97) Zener, C. *Proc. R. Soc. London, Ser. A* **1932**, *137*, 696–702.

(98) Blumberger, J. *Chem. Rev.* **2015**, *115*, PMID: 26485093, 11191–11238.

(99) Deskins, N. A.; Dupuis, M. *Phys. Rev. B* **2007**, *75*, 195212.

(100) Deskins, N. A.; Rousseau, R.; Dupuis, M. *J. Phys. Chem. C* **2009**, *113*, 14583–14586.

(101) Liao, P.; Toroker, M. C.; Carter, E. A. *Nano Lett.* **2011**, *11*, 1775–1781.

(102) Oberhofer, H.; Blumberger, J. *Phys. Chem. Chem. Phys.* **2012**, *14*, 13846–13852.

(103) Plata, J. J.; Márquez, A. M.; Sanz, J. F. *J. Phys. Chem. C* **2013**, *117*, 14502–14509.

(104) Adelstein, N.; Neaton, J. B.; Asta, M.; De Jonghe, L. C. *Phys. Rev. B* **2014**, *89*, 245115.

(105) Alidoust, N.; Carter, E. A. *Phys. Chem. Chem. Phys.* **2015**, *17*, 18098–18110.

(106) Smart, T. J.; Ping, Y. *J Phys. Condens. Matt.* **2017**, *29*, 394006.

(107) Oberhofer, H.; Reuter, K.; Blumberger, J. *Chem. Rev.* **2017**, *117*, 10319–10357.

(108) Wu, F.; Ping, Y. *J. Mater. Chem. A* **2018**, *6*, 20025–20036.

(109) Zhang, W.; Wu, F.; Li, J.; Yan, D.; Tao, J.; Ping, Y.; Liu, M. *ACS Energy Lett.* **2018**, *3*, 2232–2239.

(110) Liu, T.; Pasumarthi, V.; LaPorte, C.; Feng, Z.; Li, Q.; Yang, J.; Li, C.; Dupuis, M. *J. Mater. Chem. A* **2018**, *6*, 3714–3723.

(111) Carey, J. J.; Quirk, J. A.; McKenna, K. P. *J. Phys. Chem. C* **2021**, *125*, 12441–12450.

(112) Dey, M.; Singh, A.; Singh, A. K. *J. Phys. Chem. C* **2021**, *125*, 11548–11554.

(113) Tao, J.; Zhang, Q.; Liu, T. *Phys. Chem. Chem. Phys.* **2022**, *24*, 22918–22927.

(114) Alkauskas, A.; Lyons, J. L.; Steiauf, D.; Van de Walle, C. G. *Phys. Rev. Lett.* **2012**, *109*, 267401.

(115) Alkauskas, A.; Yan, Q.; Van de Walle, C. G. *Phys. Rev. B* **2014**, *90*, 075202.

(116) Wang, Z.; Bevan, K. H. *Phys. Rev. B* **2016**, *93*, 024303.

(117) Falletta, S.; Wiktor, J.; Pasquarello, A. *Phys. Rev. B* **2020**, *102*, 041115.

(118) Paudel, T. R.; Lambrecht, W. R. L. *Phys. Rev. B* **2008**, *77*, 205202.

(119) Kan, D.; Terashima, T.; Kanda, R.; Masuno, A.; Tanaka, K.; Chu, S.; Kan, H.; Ishizumi, A.; Kanemitsu, Y.; Shimakawa, Y., et al. *Nat. Mater.* **2005**, *4*, 816.

(120) Ambrosio, F.; Miceli, G.; Pasquarello, A. *J. Phys. Chem. Lett.* **2017**, *8*, 2055–2059.

(121) Haynes, W. M., *CRC Handbook of Chemistry and Physics*; CRC press: Boca Raton, 2014.

(122) Chen, W.; Pasquarello, A. *Phys. Rev. B* **2015**, *92*, 041115.

(123) Jain, M.; Chelikowsky, J. R.; Louie, S. G. *Phys. Rev. Lett.* **2011**, *107*, 216803.

(124) Smart, T. J.; Wu, F.; Govoni, M.; Ping, Y. *Phys. Rev. Mater.* **2018**, *2*, 124002.

(125) Chen, W.; Pasquarello, A. *Phys. Rev. B* **2013**, *88*, 115104.

(126) VandeVondele, J.; Krack, M.; Mohamed, F.; Parrinello, M.; Chassaing, T.; Hutter, J. *Comput. Phys. Commun.* **2005**, *167*, 103–128.

(127) Goedecker, S.; Teter, M.; Hutter, J. *Phys. Rev. B* **1996**, *54*, 1703–1710.

(128) Hartwigsen, C.; Goedecker, S.; Hutter, J. *Phys. Rev. B* **1998**, *58*, 3641–3662.

(129) VandeVondele, J.; Hutter, J. *J. Chem. Phys* **2007**, *127*, 114105.

(130) Guidon, M.; Hutter, J.; VandeVondele, J. *J. Chem. Theory Comput.* **2010**, *6*, 2348–2364.

(131) Van Vechten, J. A. *Phys. Rev.* **1969**, *182*, 891–905.

(132) Whited, R.; Flaten, C. J.; Walker, W. *Solid State Commun.* **1973**, *13*, 1903 –1905.

(133) Whited, R. C.; Walker, W. C. *Phys. Rev. Lett.* **1969**, *22*, 1428–1430.

(134) Thormälen, I.; Straub, J.; Grigull, U. *Phys. Chem. Ref. Data* **1985**, *14*, 933–945.

(135) Frenkel, D.; Smit, B., *Understanding Molecular Simulation: from Algorithms to Applications*; Elsevier: San Diego, 1996.

(136) Cheng, J.; Sulpizi, M.; Sprik, M. *J. Chem. Phys.* **2009**, *131*, 154504.

(137) Ambrosio, F.; Miceli, G.; Pasquarello, A. *J. Chem. Phys.* **2015**, *143*, 244508.

(138) Kirkwood, J. G. *J. Chem. Phys.* **1935**, *3*, 300–313.

(139) Rinke, P.; Schleife, A.; Kioupakis, E.; Janotti, A.; Rödl, C.; Bechstedt, F.; Scheffler, M.; Van de Walle, C. G. *Phys. Rev. Lett.* **2012**, *108*, 126404.

(140) Falletta, S.; Wiktor, J.; Pasquarello, A. https://github.com/falletta/finite-size-corrections-defect-levels, 2020.

(141) Falletta, S.; Pasquarello, A. *Phys. Rev. Lett.* **2022**, *129*, 126401.

(142) Falletta, S.; Pasquarello, A. *Phys. Rev. B* **2022**, *106*, 125119.

(143) Peng, H.; McKendry, I. G.; Ding, R.; Thenuwara, A. C.; Kang, Q.; Shumlas, S. L.; Strongin, D. R.; Zdilla, M. J.; Perdew, J. P. *Proc. Natl. Acad. Sci.* **2017**, *114*, 9523–9528.

(144) Ambrosio, F.; Wiktor, J.; De Angelis, F.; Pasquarello, A. *Energy Environ. Sci.* **2018**, *11*, 101–105.

(145) Elmaslmane, A. R.; Watkins, M. B.; McKenna, K. P. *J. Chem. Theory Comput.* **2018**, *14*, 3740–3751.

(146) Carey, J. J.; McKenna, K. P. *J. Phys. Chem. C* **2019**, *123*, 22358–22367.

(147) Quirk, J. A.; Lazarov, V. K.; McKenna, K. P. *J. Phys. Chem. C* **2020**, *124*, 23637–23647.

(148) Wing, D.; Ohad, G.; Haber, J. B.; Filip, M. R.; Gant, S. E.; Neaton, J. B.; Kronik, L. *Proc. Natl. Acad. Sci.* **2021**, *118*, e2104556118.

(149) Pacchioni, G.; Frigoli, F.; Ricci, D.; Weil, J. A. *Phys. Rev. B* **2000**, *63*, 054102.

(150) Lægsgaard, J.; Stokbro, K. *Phys. Rev. Lett.* **2001**, *86*, 2834–2837.

(151) Gerosa, M.; Di Valentin, C.; Bottani, C. E.; Onida, G.; Pacchioni, G. *J. Chem. Phys.* **2015**, *143*, 111103.

(152) Han, D.; West, D.; Li, X.-B.; Xie, S.-Y.; Sun, H.-B.; Zhang, S. B. *Phys. Rev. B* **2010**, *82*, 155132.

(153) Giannozzi, P. et al. *J. Phys.: Condens. Matter* **2009**, *21*, 395502.

(154) van Setten, M.; Giantomassi, M.; Bousquet, E.; Verstraete, M.; Hamann, D.; Gonze, X.; Rignanese, G.-M. *Comput. Phys. Commun.* **2018**, *226*, 39 –54.

(155) Wiktor, J.; Reshetnyak, I.; Ambrosio, F.; Pasquarello, A. *Phys. Rev. Mater.* **2017**, *1*, 022401.

(156) Wiktor, J.; Reshetnyak, I.; Strach, M.; Scarongella, M.; Buonsanti, R.; Pasquarello, A. *J. Phys. Chem. Lett.* **2018**, *9*, PMID: 30193068, 5698–5703.

(157) Capano, G.; Ambrosio, F.; Kampouri, S.; Stylianou, K. C.; Pasquarello, A.; Smit, B. *J. Phys. Chem. C* **2020**, *124*, 4065–4072.

(158) Wing, D.; Strand, J.; Durrant, T.; Shluger, A. L.; Kronik, L. *Phys. Rev. Mater.* **2020**, *4*, 083808.

(159) Sayama, K.; Nomura, A.; Arai, T.; Sugita, T.; Abe, R.; Yanagida, M.; Oi, T.; Iwasaki, Y.; Abe, Y.; Sugihara, H. *J. Phys. Chem. B* **2006**, *110*, 11352–11360.

(160) Luo, H.; Mueller, A. H.; McCleskey, T. M.; Burrell, A. K.; Bauer, E.; Jia, Q. X. *J. Phys. Chem. C* **2008**, *112*, 6099–6102.

(161) Kudo, A.; Omori, K.; Kato, H. *J. Am. Chem. Soc.* **1999**, *121*, 11459–11467.

(162) Nery, J. P.; Allen, P. B.; Antonius, G.; Reining, L.; Miglio, A.; Gonze, X. *Phys. Rev. B* **2018**, *97*, 115145.

(163) Onuma, T.; Kosaka, W.; Kudo, K.; Ota, Y.; Yamaguchi, T.; Kaneko, K.; Fujita, S.; Honda, T. *Appl. Phys. Lett.* **2021**, *119*, 132105.

(164) Kresse, G.; Marsman, M.; Hintzsche, L. E.; Flage-Larsen, E. *Phys. Rev. B* **2012**, *85*, 045205.

(165) Engel, M.; Miranda, H.; Chaput, L.; Togo, A.; Verdi, C.; Marsman, M.; Kresse, G., 2022.

(166) Philipp, H. *Solid State Commun.* **1966**, *4*, 73–75.

(167) Refaely-Abramson, S.; Jain, M.; Sharifzadeh, S.; Neaton, J. B.; Kronik, L. *Phys. Rev. B* **2015**, *92*, 081204.

(168) Yang, S.; Brant, A. T.; Halliburton, L. E. *Phys. Rev. B* **2010**, *82*, 035209.

(169) Alkauskas, A.; Broqvist, P.; Pasquarello, A. *Phys. Status Solidi B* **2011**, *248*, 775–789.

(170) Marques, M. A. L.; Vidal, J.; Oliveira, M. J. T.; Reining, L.; Botti, S. *Phys. Rev. B* **2011**, *83*, 035119.

(171) Skone, J. H.; Govoni, M.; Galli, G. *Phys. Rev. B* **2014**, *89*, 195112.

(172) Chen, W.; Miceli, G.; Rignanese, G.-M.; Pasquarello, A. *Phys. Rev. Mater.* **2018**, *2*, 073803.

(173) Bassani, F.; Parravicini, G. P., *Electronic states and optical transitions in solids*; Elsevier Science & Technology: 1975.

(174) Henderson, T. M.; Paier, J.; Scuseria, G. E. *Phys. Status Solidi (b)* **2011**, *248*, 767–774.

(175) Gavartin, J. L.; Sushko, P. V.; Shluger, A. L. *Phys. Rev. B* **2003**, *67*, 035108.

(176) Carvalho, A.; Alkauskas, A.; Pasquarello, A.; Tagantsev, A. K.; Setter, N. *Phys. Rev. B* **2009**, *80*, 195205.

(177) Kümmel, S.; Kronik, L. *Rev. Mod. Phys.* **2008**, *80*, 3–60.

(178) Klüpfel, S.; Klüpfel, P.; Jónsson, H. *J. Chem. Phys.* **2012**, *137*, 124102.

(179) Rachko, Z. A.; Valbis, J. A. *Phys. Status Solidi B* **1979**, *93*, 161–166.

(180) Dolgov, S.; Kärner, T; Lushchik, A; Maaroos, A; Nakonechnyi, S; Shablonin, E *Phys. Solid State* **2011**, *53*, 1244–1252.

(181) Shluger, A. L.; Heifets, E. N.; Gale, J. D.; Catlow, C. R. A. *J. Phys.: Condens. Matter* **1992**, *4*, 5711–5722.

(182) Ganduglia-Pirovano, M. V.; Da Silva, J. L. F.; Sauer, J. *Phys. Rev. Lett.* **2009**, *102*, 026101.

(183) Shluger, A. L.; McKenna, K. P.; Sushko, P. V.; Ramo, D. M.; Kimmel, A. V. *Model. Simul. Mater. Sci. Eng.* **2009**, *17*, 084004.

(184) Falletta, S.; Pasquarello, A. *npj Comput. Mater.* **2022**, *8*, 265.

(185) Anisimov, V. I.; Gunnarsson, O. *Phys. Rev. B* **1991**, *43*, 7570–7574.

(186) Anisimov, V. I.; Zaanen, J.; Andersen, O. K. *Phys. Rev. B* **1991**, *44*, 943–954.

(187) Anisimov, V. I.; Solovyev, I. V.; Korotin, M. A.; Czyżyk, M. T.; Sawatzky, G. A. *Phys. Rev. B* **1993**, *48*, 16929–16934.

(188) Solovyev, I. V.; Dederichs, P. H.; Anisimov, V. I. *Phys. Rev. B* **1994**, *50*, 16861–16871.

(189) Czyżyk, M. T.; Sawatzky, G. A. *Phys. Rev. B* **1994**, *49*, 14211–14228.

(190) Liechtenstein, A. I.; Anisimov, V. I.; Zaanen, J. *Phys. Rev. B* **1995**, *52*, R5467–R5470.

(191) Anisimov, V. I.; Aryasetiawan, F; Lichtenstein, A. I. *J. Phys. Condens. Matter* **1997**, *9*, 767–808.

(192) Dudarev, S. L.; Botton, G. A.; Savrasov, S. Y.; Humphreys, C. J.; Sutton, A. P. *Phys. Rev. B* **1998**, *57*, 1505–1509.

(193) Petukhov, A. G.; Mazin, I. I.; Chioncel, L.; Lichtenstein, A. I. *Phys. Rev. B* **2003**, *67*, 153106.

(194) Zhou, F.; Cococcioni, M.; Marianetti, C. A.; Morgan, D.; Ceder, G. *Phys. Rev. B* **2004**, *70*, 235121.

(195) Tao, K.; Zhou, J.; Sun, Q.; Wang, Q.; Stepanyuk, V. S.; Jena, P. *Phys. Rev. B* **2014**, *89*, 085103.

(196) Bjaalie, L.; Verma, A.; Himmetoglu, B.; Janotti, A.; Raghavan, S.; Protasenko, V.; Steenbergen, E. H.; Jena, D.; Stemmer, S.; Van de Walle, C. G. *Phys. Rev. B* **2015**, *92*, 085111.

(197) Mann, G. W.; Lee, K.; Cococcioni, M.; Smit, B.; Neaton, J. B. *J. Chem. Phys.* **2016**, *144*, 174104.

(198) Ricca, C.; Timrov, I.; Cococcioni, M.; Marzari, N.; Aschauer, U. *Phys. Rev. B* **2019**, *99*, 094102.

(199) Timrov, I.; Marzari, N.; Cococcioni, M. *Phys. Rev. B* **2018**, *98*, 085127.

(200) Floris, A.; Timrov, I.; Himmetoglu, B.; Marzari, N.; de Gironcoli, S.; Cococcioni, M. *Phys. Rev. B* **2020**, *101*, 064305.

(201) Timrov, I.; Marzari, N.; Cococcioni, M. *Phys. Rev. B* **2021**, *103*, 045141.

(202) Timrov, I.; Marzari, N.; Cococcioni, M. *Comput. Phys. Commun.* **2022**, *279*, 108455.

(203) Dudarev, S. L.; Liu, P.; Andersson, D. A.; Stanek, C. R.; Ozaki, T.; Franchini, C. *Phys. Rev. Materials* **2019**, *3*, 083802.

(204) Wang, L.; Maxisch, T.; Ceder, G. *Phys. Rev. B* **2006**, *73*, 195107.

(205) García-Mota, M.; Bajdich, M.; Viswanathan, V.; Vojvodic, A.; Bell, A. T.; Nørskov, J. K. *J. Phys. Chem. C* **2012**, *116*, 21077–21082.

(206) Jain, A.; Hautier, G.; Ong, S. P.; Moore, C. J.; Fischer, C. C.; Persson, K. A.; Ceder, G. *Phys. Rev. B* **2011**, *84*, 045115.

(207) Bajdich, M.; García-Mota, M.; Vojvodic, A.; Nørskov, J. K.; Bell, A. T. *J. Am. Chem. Soc.* **2013**, *135*, 13521–13530.

(208) Franchini, C.; Podloucky, R.; Paier, J.; Marsman, M.; Kresse, G. *Phys. Rev. B* **2007**, *75*, 195128.

(209) Aschauer, U.; Pfenninger, R.; Selbach, S. M.; Grande, T.; Spaldin, N. A. *Phys. Rev. B* **2013**, *88*, 054111.

(210) Hong, J.; Stroppa, A.; Íñiguez, J.; Picozzi, S.; Vanderbilt, D. *Phys. Rev. B* **2012**, *85*, 054417.

(211) Deskins, N. A.; Dupuis, M. *J. Phys. Chem. C* **2009**, *113*, 346–358.

(212) Patrick, C. E.; Giustino, F. *J. Phys.: Cond. Matter* **2012**, *24*, 202201.

(213) Erhart, P.; Klein, A.; Åberg, D.; Sadigh, B. *Phys. Rev. B* **2014**, *90*, 035204.

(214) Kulik, H. J.; Cococcioni, M.; Scherlis, D. A.; Marzari, N. *Phys. Rev. Lett.* **2006**, *97*, 103001.

(215) Mosey, N. J.; Carter, E. A. *Phys. Rev. B* **2007**, *76*, 155123.

(216) Mosey, N. J.; Liao, P.; Carter, E. A. *J. Chem. Phys.* **2008**, *129*, 014103.

(217) Aryasetiawan, F.; Karlsson, K.; Jepsen, O.; Schönberger, U. *Phys. Rev. B* **2006**, *74*, 125106.

(218) Miyake, T.; Aryasetiawan, F. *Phys. Rev. B* **2008**, *77*, 085122.

(219) Şaşıoğlu, E.; Friedrich, C.; Blügel, S. *Phys. Rev. B* **2011**, *83*, 121101.

(220) Setvin, M.; Franchini, C.; Hao, X.; Schmid, M.; Janotti, A.; Kaltak, M.; Van de Walle, C. G.; Kresse, G.; Diebold, U. *Phys. Rev. Lett.* **2014**, *113*, 086402.

(221) Tavadze, P.; Boucher, R.; Avendaño-Franco, G.; Kocan, K. X.; Singh, S.; Dovale-Farelo, V.; Ibarra-Hernández, W.; Johnson, M. B.; Mebane, D. S.; Romero, A. H. *npj Comput. Mater.* **2021**, *7*, 1–9.

(222) Yu, M.; Yang, S.; Wu, C.; Marom, N. *npj Comput. Mater.* **2020**, *6*, 1–6.

(223) Schirmer, O. *J. Phys. Chem. Solids* **1971**, *32*, 499–509.

(224) Shluger, A.; Kotomin, E.; Kantorovich, L. *J. Phys. C: Solid State Phys.* **1986**, *19*, 4183.

(225) Alkauskas, A.; Pasquarello, A. *Phys. Rev. B* **2011**, *84*, 125206.

(226) Laughlin, R. B.; Joannopoulos, J. D.; Chadi, D. J. *Phys. Rev. B* **1979**, *20*, 5228–5237.

(227) Imada, M.; Fujimori, A.; Tokura, Y. *Rev. Mod. Phys.* **1998**, *70*, 1039–1263.

(228) Falletta, S.; Pasquarello, A. in preparation, 2022.

(229) Zhang, S. X.; Kundaliya, D. C.; Yu, W.; Dhar, S.; Young, S. Y.; Salamanca-Riba, L. G.; Ogale, S. B.; Vispute, R. D.; Venkatesan, T. *J. Appl. Phys.* **2007**, *102*, 013701.

(230) Harwig, T.; Kellendonk, F. *J. Solid State Chem.* **1978**, *24*, 255 –263.

(231) Binet, L.; Gourier, D. *J. Phys. Chem. Solids* **1998**, *59*, 1241–1249.

(232) Higashiwaki, M.; Sasaki, K.; Murakami, H.; Kumagai, Y.; Koukitu, A.; Kuramata, A.; Masui, T.; Yamakoshi, S. *Semicond. Sci. Technol.* **2016**, *31*, 034001.

(233) Pearton, S. J.; Yang, J.; Cary, P. H.; Ren, F.; Kim, J.; Tadjer, M. J.; Mastro, M. A. *Appl. Phys. Rev.* **2018**, *5*, 011301.

(234) Guo, D.; Guo, Q.; Chen, Z.; Wu, Z.; Li, P.; Tang, W. *Mater. Today Phys.* **2019**, *11*, 100157.

(235) Tadjer, M. J.; Lyons, J. L.; Nepal, N.; Freitas, J. A.; Koehler, A. D.; Foster, G. M. *ECS J. Solid State Sci. Technol.* **2019**, *8*, Q3187–Q3194.

(236) Villora, E. G.; Yamaga, M.; Inoue, T.; Yabasi, S.; Masui, Y.; Sugawara, T.; Fukuda, T. *Jpn. J. Appl. Phys.* **2002**, *41*, L622.

(237) Yamaga, M.; Ishikawa, T.; Yoshida, M.; Hasegawa, T.; Villora, E. G.; Shimamura, K. *Phys. Status Solidi C* **2011**, *8*, 2621–2624.

(238) Armstrong, A. M.; Crawford, M. H.; Jayawardena, A.; Ahyi, A.; Dhar, S. *J. Appl. Phys.* **2016**, *119*, 103102.

(239) Yamaoka, S.; Nakayama, M. *Phys. Status Solidi C* **2016**, *13*, 93–96.

(240) Kananen, B. E.; Giles, N. C.; Halliburton, L. E.; Foundos, G. K.; Chang, K. B.; Stevens, K. T. *J. Appl. Phys* **2017**, *122*, 215703.

(241) Ho, Q. D.; Frauenheim, T.; Deák, P. *Phys. Rev. B* **2018**, *97*, 115163.

(242) Polyakov, A. Y.; Smirnov, N. B.; Shchemerov, I. V.; Pearton, S. J.; Ren, F.; Chernykh, A. V.; Lagov, P. B.; Kulevoy, T. V. *APL Materials* **2018**, *6*, 096102.

(243) Gake, T.; Kumagai, Y.; Oba, F. *Phys. Rev. Mater.* **2019**, *3*, 044603.

(244) Frodason, Y. K.; Johansen, K. M.; Vines, L.; Varley, J. B. *J. Appl. Phys.* **2020**, *127*, 075701.

(245) Marcinkevičius, S.; Speck, J. S. *Appl. Phys. Lett.* **2020**, *116*, 132101.

(246) Bouzid, A.; Pasquarello, A. *Phys. Status Solidi RRL* **2019**, *13*, 1800633.

(247) Song, Y. P.; Zhang, H. Z.; Lin, C.; Zhu, Y. W.; Li, G. H.; Yang, F. H.; Yu, D. P. *Phys. Rev. B* **2004**, *69*, 075304.

(248) Varley, J. B.; Weber, J. R.; Janotti, A.; Van de Walle, C. G. *Appl. Phys. Lett.* **2010**, *97*, 142106.

(249) Tang, C.; Sun, J.; Lin, N.; Jia, Z.; Mu, W.; Tao, X.; Zhao, X. *RSC Adv.* **2016**, *6*, 78322–78334.

(250) Kananen, B. E.; Halliburton, L. E.; Stevens, K. T.; Foundos, G. K.; Giles, N. C. *Appl. Phys. Lett.* **2017**, *110*, 202104.

(251) Pozina, G.; Forsberg, M.; Kaliteevski, M.; Hemmingsson, C. *Sci. Rep.* **2017**, *7*, 1–8.

(252) Banerjee, S.; Jiang, X.; Wang, L.-W. *Phys. Chem. Chem. Phys.* **2018**, *20*, 9471–9479.

(253) Ingebrigtsen, M. E.; Varley, J. B.; Kuznetsov, A. Y.; Svensson, B. G.; Alfieri, G.; Mihaila, A.; Badstübner, U.; Vines, L. *Appl. Phys. Lett.* **2018**, *112*, 042104.

(254) Peelaers, H.; Lyons, J. L.; Varley, J. B.; Van de Walle, C. G. *APL Mater.* **2019**, *7*, 022519.

(255) Von Bardeleben, H. J.; Zhou, S.; Gerstmann, U.; Skachkov, D.; Lambrecht, W. R. L.; Ho, Q. D.; Deák, P. *APL Mater.* **2019**, *7*, 022521.

(256) Peelaers, H.; Van de Walle, C. G. *Phys. Rev. B* **2019**, *100*, 081202.

(257) Skachkov, D.; Lambrecht, W. R. L.; von Bardeleben, H. J.; Gerstmann, U.; Ho, Q. D.; Deák, P. *J. Appl. Phys.* **2019**, *125*, 185701.

(258) McCluskey, M. D. *J. Appl. Phys.* **2020**, *127*, 101101.

(259) Passlack, M.; Schubert, E. F.; Hobson, W. S.; Hong, M.; Moriya, N.; Chu, S. N. G.; Konstadinidis, K.; Mannaerts, J. P.; Schnoes, M. L.; Zydzik, G. J. *J. Appl. Phys.* **1995**, *77*, 686–693.

(260) Tippins, H. H. *Phys. Rev.* **1965**, *140*, A316–A319.

(261) Bell, R. P.; Hinshelwood, C. N. *Proc. R. Soc. Long. A* **1936**, *154*, 414–429.

(262) Evans, M. G.; Polanyi, M. *Trans. Faraday Soc.* **1938**, *34*, 11–24.

(263) Chan, M. K. Y.; Ceder, G. *Phys. Rev. Lett.* **2010**, *105*, 196403.

(264) Hedin, L. *Phys. Rev.* **1965**, *139*, A796–A823.

(265) Chen, W.; Pasquarello, A. *Phys. Rev. B* **2014**, *90*, 165133.

(266) Levine, Z. H.; Allan, D. C. *Phys. Rev. Lett.* **1989**, *63*, 1719–1722.

(267) Baraff, G. A.; Schlüter, M. *Phys. Rev. B* **1984**, *30*, 1853–1866.

(268) Gonze, X.; Ghosez, P.; Godby, R. W. *Phys. Rev. Lett.* **1995**, *74*, 4035–4038.

(269) Deák, P.; Frauenheim, T.; Gali, A. *Phys. Rev. B* **2007**, *75*, 153204.

(270) Alkauskas, A.; Broqvist, P.; Pasquarello, A. *Phys. Rev. Lett.* **2008**, *101*, 046405.

(271) Deák, P.; Gali, A.; Aradi, B.; Frauenheim, T. *Phys. Status Solidi B* **2011**, *248*, 790–798.

(272) Carvalho, A.; Jones, R.; Janke, C.; Goss, J. P.; Briddon, P. R.; Coutinho, J.; Öberg, S. *Phys. Rev. Lett.* **2007**, *99*, 175502.

(273) Miceli, G.; Pasquarello, A. *Microelectr. Eng.* **2015**, *147*, 51–54.

(274) Holloway, H.; Hass, K. C.; Tamor, M. A.; Anthony, T. R.; Banholzer, W. F. *Phys. Rev. B* **1991**, *44*, 7123–7126.

(275) Reeber, R. R.; Wang, K. *J. Mater. Res.* **2000**, *15*, 40–44.

(276) Madelung, O., *Semiconductors: group IV elements and III-V compounds*; Springer Science & Business Media: 2012.

(277) Madelung, O., *Semiconductors—basic data*; Springer Science & Business Media: 2012.

(278) Vurgaftman, I.; Meyer, J. R.; Ram-Mohan, L. R. *J. Appl. Phys.* **2001**, *89*, 5815–5875.

(279) Hinuma, Y.; Pizzi, G.; Kumagai, Y.; Oba, F.; Tanaka, I. *Comput. Mater. Sci.* **2017**, *128*, 140–184.

(280) Tyuterev, V.; Vast, N. *Comput. Mater. Sci.* **2006**, *38*, 350–353.

(281) Menoni, C. S.; Hu, J. Z.; Spain, I. L. *Phys. Rev. B* **1986**, *34*, 362–368.

(282) Wright, A. F. *J. Appl. Phys.* **1997**, *82*, 2833–2839.

(283) McSkimin, H. J.; Jayaraman, A.; Andreatch, P. *J. Appl. Phys.* **1967**, *38*, 2362–2364.

Stefano Falletta

Curriculum Vitae

Personal Information

Birth 4th January 1995 in Siracusa, Italy

Nationality Italian

Education

2018 – 2023 **Ph.D. in Physics**, EPFL, Switzerland.

2016 – 2018 **M.Sc. in Physics of Complex Systems**, Politecnico di Torino, Italy, 110/110 with honor.

2017 – 2018 **M.Sc. in Physics of Complex Systems**, Université Paris Sud, France, with honor.

2016 – 2018 **M.Sc. in Mathematical Engineering**, Politecnico di Milano, Italy, 110/110 with honor.

2016 – 2018 **Diploma in Business Management and Entrepreneurship**, Alta Scuola Politecnica, Italy.

2013 – 2016 **B.Sc. in Physics Engineering**, Politecnico di Torino, Italy, 110/110 with honor.

Research Experiences

2018 – 2023 **Graduate Student**, EPFL, Switzerland, group of Prof. Alfredo Pasquarello.

2022 **Visitor**, Max Planck Institute for Eisenforschung, Germany, group of Dr. Christoph Freysoldt.

2019 **Visitor**, University of Zurich, Switzerland, group of Prof. Juerg Hutter.

2018 **Intern**, Fermi National Accelerator Laboratory, USA, group of Prof. Emanuela Barzi.

2018 **Intern**, École Polytechnique, France, group of Prof. Silke Bierman.

2017 – 2018 **Intern**, IBM & Politecnico di Milano, Italy.

2017 **Intern**, Fermi National Accelerator Laboratory, USA, group of Prof. Emanuela Barzi.

Publications

2023 **Polaron hopping through piecewise-linear functionals**, Falletta, S., Pasquarello, A., in preparation.

2023 **Range-separated hybrid functionals for accurate band gap prediction**, Yang, J., Falletta, S., Pasquarello, A., in review in *npj Computational Materials*.

2022 **Hubbard *U* through polaronic defect states**, Falletta, S., Pasquarello, A., *npj Computational Materials* 8(1), 263.

2022 **Many-body self-interaction and polarons**, Falletta, S., Pasquarello, A., *Physical Review Letters*, 129, 126401.

2022 **Polarons free from many-body self-interaction in density functional theory**, Falletta, S., Pasquarello, A., *Physical Review B*, 106, 125119.

2022 **One-shot approach for enforcing piecewise linearity on hybrid functionals: application to band gap predictions**, Yang, J., Falletta, S., Pasquarello, A., *The Journal of Physical Chemistry Letters*, 13(13), 3066-3071.

2020 **Finite-size corrections of defect energy levels involving ionic polarization**, Falletta, S., Wiktor, J., and Pasquarello, A., *Physical Review B*, 102(4), 041115.

2020 **Unraveling the synergy between metal-organic frameworks and co-catalysts in photocatalytic water splitting**, Falletta, S., Gono, P., Guo, Z., Kampouri, S., Stylianou, K., and Pasquarello, A., *Journal of Materials Chemistry A*, 8 (39), 20493-20502.

2020 **Small electron polarons in CsPbBr$_3$: competition between electron localization and delocalization**, Österbacka, N., Erhart, P., Falletta, S., Pasquarello, A., and Wiktor, J., *Chemistry of Materials*, 32 (19), 8393-8400.

2019 **An innovative Nb$_3$Sn film approach and its potential for SRF applications**, Barzi, E., Ciaccia, C., Falletta, S., Turrioni, D., Kikuchi, A., Hayano, H., Saeki, T., Ito, H., Eremeev, G., Geng, R., and Rimmer, R., *29th Linear Accelerator Conference*, Beijing, China, JACOW Publishing, Geneva, Switzerland.

2018 **Conversational support for education**, Akcora, D. E., Belli, A., Berardi, M., Casola, S., Di Blas, N., Falletta, S., Faraotti, A., Lodi, L., Diaz, D. N., Paolini, P., Renzi, F., and Vannella, F., *International Conference on Artificial Intelligence in Education*, Springer, Cham.

2018 **Nb$_3$Sn thin films for the production of higher gradient SRF cavities at reduced cost**, Kahn, S., Barzi, E., Cummings, M. A., Falletta, S., Kikuchi, A., and Turrioni, D., *9th International Particle Accelerator Conference*, Vancouver, BC, Canada, JACOW Publishing, Geneva, Switzerland.